Stabilization of foams by in-situ hydrophobized nanoparticles

vorgelegt von
Frank Adrian Carl
aus Berlin

von der Fakultät II - Mathematik und Naturwissenschaften
an der Technischen Universität Berlin
zur
Erlangung des akademischen Grades

Doktor der Naturwissenschaften
(Dr. rer. nat.)

genehmigte Dissertation

Promotionsausschuss:

Vorsitzender:	Prof. Dr. Reinhard Schomäcker
1. Gutachter:	Prof. Dr. Regine von Klitzing
2. Gutachter:	Dr. habil. Wiebke Drenckhan-Andreatta

Tag der wissenschaftlichen Aussprache: 18.07.2016

Berlin 2016

Acknowledgment

I would like to thank my advisor Prof. Dr. Regine von Klitzing for giving me the opportunity to work in her research group. Without her encouragement, guidance and helpful suggestions, I would not have been able to complete my dissertation. I appreciate her input and funding throughout my dissertation.

The order of mentions does not reflect any rating whatsoever.

Dr. Antonio Stocco earns my gratitude for introducing me to Diffusing Wave Spectroscopy and thereby planting the seed for a fruitful part of this thesis.

I would like to thank all my colleagues from the TU Berlin who shared their time and energy.

I am grateful for my student assistants Anne Bannuscher and Judith Witte who were always motivated and eager to learn. They conducted all experiments with great care and therefore made a great impact to this work.

I would like to thank Dr. Stefan Wellert and Dr. Kornelia Gawlitza for their friendship, advice, ideas and great discussions on and off campus.

My office colleagues Samantha Micciulla, Bhuvnesh Bharti, Mojdeh Heidari, Jens Meißner and Heiko Fauser for their kindness and good-heartedness that made the days of data crunching enjoyable.

I would like to thank Dr. Marieke Üzüm and Martin Uhlig for pushing it in the gym and being awesome the rest of the time.

Special thanks to my family for their love, support and patience.

Finally, Verena, I am deeply grateful to have you as my companion. You believe in me when I don't. The list of things that I thank you for would be a thesis itsself.

God made the bulk; surfaces were invented by the devil.

- Wolfgang Pauli

Contents

1. Introduction **7**

2. Scientific background **11**

2.1. Particles versus surfactants 11
2.2. Surface forces 12
2.2.1. Surface tension 12
2.2.2. Surface pressure 13
2.2.3. Surface elasticity 14
2.3. Foam ageing 14
2.3.1. Drainage 14
2.3.2. Coarsening 15
2.3.3. Coalescence 16
2.4. Particle aggregation 16
2.5. Probing of foam structure and dynamics 17

3. Methods and Apparatus **19**

3.1. Density measurements 19
3.2. Zeta Potential / Electrophoretic Mobility 20
3.3. X-Ray Reflectivity 21
3.4. Axisymmetric Drop Shape Analysis (ADSA) 22
3.5. Photon Correlation Techniques 23
3.5.1. Dynamic Light Scattering (DLS) 25
3.5.2. Diffusing Wave Spectroscopy (DWS) 26

4. Experimental section **29**

4.1. Materials and preparation 29
4.1.1. Materials 29
4.1.2. Preparation of suspensions 29
4.2. Experiments and apparatus 30
4.2.1. Zeta potential / Electrophoretic mobility 30
4.2.2. Pyrene Fluorescence 30
4.2.3. X-ray Reflectivity (XRR) 31
4.2.4. Interfacial Tension (IFT) 31
4.2.5. Surface Pressure Isotherms 31
4.2.6. Dynamic Light Scattering (DLS) 32
4.2.7. Diffusing Wave Spectroscopy (DWS) 32
4.2.8. Particle Extraction and Foam Volume 33
4.2.9. Macroscopic Foamability 34

5. Particle Adsorption and Contact Angle **35**
5.1. Introduction . . . 35
5.2. Results . . . 37
5.2.1. Interfacial Tension (IFT) . . . 37
5.2.2. X-ray Reflectivity . . . 37
5.2.3. Theoretical Calculations . . . 46
5.3. Discussion . . . 48
5.4. Conclusion . . . 51

6. Bulk Behavior and Interfacial Structure **53**
6.1. Introduction . . . 53
6.2. Results . . . 55
6.2.1. Bulk Behavior . . . 55
6.2.2. Interfacial Behavior . . . 57
6.2.3. Foaming Behavior . . . 62
6.3. Discussion . . . 66
6.4. Conclusion . . . 70

7. Particle Structure and Dynamics of the Foam **71**
7.1. Introduction . . . 71
7.2. Results . . . 73
7.3. Discussion . . . 80
7.4. Conclusion . . . 84

8. Summary and Outlook **89**

List of Figures **101**

A. Listings **105**
A.1. XRR fitting . . . 105
A.2. Surface Fraction Calculations . . . 108

Abstract

All foams are composed of a liquid, a surface active compound and a gas. The gas is dispersed in the liquid phase creating a highly complex and hierarchical structure. The surface active compound prevents the immediate collapse of the foam. For classical foams, low molecular weight surfactants are used to stabilize the gas/liquid interface. Alternatively, solid particles can stabilize the interface. The present study deals with the stabilization of foams by solid particles.

The in-situ adsorption of short chain amines onto hydrophilic silica nanoparticles is chosen in the present thesis to render the particle hydrophobic. Foams are prepared from the particle suspensions with varying amounts of alkyl amines to change the particle hydrophobicity. Additionally, the dependence of the amine chain length is studied from a carbon chain length of C_5 to C_8. The system is studied at different length and time scales. A comprehensive understanding of the stabilizing mechanisms of the particle stabilized foams is obtained.

In the bulk suspension, amine adsorption onto the particles is proven by ζ-potential measurements. A change in the potential from $\approx$ -35 mV towards charge neutralitiy is found with increasing amine concentration. A critical amine concentration (CAC) is found for each chain length above which particle flocculation occurs. This effect can be explained by the formation of hydrophobic patches on the particle surface. These hydrophobic domains are shown by a fluorescent probe experiment. Further characterization of the bulk liquid is performed by dynamic liqht scattering. Here, an increase in particle size is found above the CAC, indicating the existance of particle flocculates.

For interfacially adsorbed particles, a contact angle of 30 to 45° is found. It increases with increasing amine concentration as well as increasing amine chain length. The contact angle is determined by x-ray reflectivity measurements and suitable data analysis, as described in the thesis. Lateral interaction of the particles at the interface is shown by surface pressure isotherms. The mechanical response of the interface allows to deduct structural features of the interface. A fractal model is suggested for the particle arrangement, which fits well to theoretical literature models.

The life time of the macroscopic foam increases dramatically above the CAC as seen by image analysis. Diffusing wave spectroscopy is employed as a tool to resolve this effect microscopically. In combination with particle depletion measurements, it is shown that particles form aggregates within the foam structure above the CAC. This leads to a decelleration of the foam ageing processes. On the other hand, it is shown that the particle dimensions in the foam can be determined in good agreement with measurements in the bulk suspension.

Zusammenfassung

Schäume sind komplexe, hierarchische Strukturen, zusammengesetzt aus einer flüssigen Phase, einer Gasphase und einer stabilisierenden Komponente. Die stabilisierende Komponente verhindert dabei, dass die Struktur unmittelbar nach ihrer Entstehung wieder kollabiert. Gewöhnlich werden Schäume durch niedermolekulare Tenside stabilisiert. Es ist jedoch auch möglich, Partikel zur Stabilisierung der Grenzflächen zu nutzen. Die vorliegende Arbeit befasst sich mit dieser Stabilisierung von Schäumen durch Nanopartikel.

Um die Partikel zu hydrophobisieren werden kurzkettige Alkylamine genutzt, die auf die Partikeloberfläche adsorbieren. Die Aminkonzentration und -kettenlänge wird variiert, um die Partikelhydrophobizität einzustellen. Die Alkylkettenlänge variiert dabei von C_5 bis C_8. Das System und die präparierten Schäume werden auf verschiedenen Längen und Zeitskalen charaktierisiert. Ein umfassendes Verständnis der zugrundeliegenden Mechanismen der Schaumstabilisierung durch die teilhydrophobisierten Partikel wird durch die vorliegende Arbeit erlangt.

Die Adsorption der Amine auf die Partikeloberflächen wird durch Messungen des ζ-Potentials nachgewiesen. Das Potential der Partikeloberfläche ohne Aminadsorption von ca. -35 mV wird mit zunehmender Aminkonzentration in Richtung 0 mV verschoben. Für jede Kettenlänge existiert eine charakteristische Aminkonzentration (CAC), oberhalb derer Flokkulation stattfindet. In einem Fluoreszenzexperiment wird gezeigt, dass diese Flokkulation mit der Bildung von hydrophoben Domänen auf der Partikeloberfläche zusammenhängt. Die Flokkulation und die CAC wird zusätzlich durch dynamische Lichtstreumessungen belegt.

Für die an der Grenzfläche adsorbierten Partikel werden Konktaktwinkel von ca. 30 bis 45° gefunden. Der Kontaktwinkel steigt mit zunehmender Konzentration und Kettenlänge der Amine. Röntgenreflektometrie in Verbindung mit einer geeigneten Datenanalyse erlaubt eine zuverlässige Messung des Kontaktwinkels, wie in der vorliegenden Arbeit gezeigt wird. Die laterale Wechselwirkung der adsorbierten Partikel wird durch Oberflächendruckisothermen untersucht. Die mechanische Antwort der Grenzfläche erlaubt Rückschlüsse auf die Struktur der Partikel. Im vorliegenden Fall wird ein durch die Literatur gestütztes Fraktalmodell genutzt.

Oberhalb der CAC nimmt die Stabilität der Schäume deutlich zu, wie durch Bildanalyse gezeigt wird. Mittels Diffusing Wave Spektroskopie kann dieser Effekt auf mikroskopischem Level aufgeklärt werden. Aggregation der Partikel in der Flüssigphase bremst die Alterungsprozesse des Schaums und erhöht dessen Stabilität. Die Verarmung an Partikeln in der Volumenphase stützt diese Beobachtung. Zusätzlich wird gezeigt, dass die Partikelgröße im Schaum mit zufriedenstellender Genauigkeit bestimmt werden kann.

Chapter 1.

Introduction

Dispersing different materials in one another is a common method to create materials with new and interesting properties. With at least one component being a fluid, usually soft matter is created. The definition of soft matter is not a strict one but dispersions of one fluid in another one definitely falls into the category of soft matter. In the case of a foam, one fluid is a gas and the other one is a liquid. The liquid phase can be water, oil or even another complex fluid itself. Undoubtedly, foams are the aesthetically most pleasing form of simple dispersions. Since foams are mostly composed of gas, their structure is very delicate. The lifespan of a foam is usually transient. Interestingly, by combining gas and liquid, a structure is obtained which also obeys the properties of a solid.

Below their yield stress, foams respond solid-like to external deformation, showing elastic properties. Above the yield stress, foams behave as non-Newtonian liquids and can be poured or pumped. When the ambient pressure is increased, a foam will respond like a gas and follow the ideal gas equation to a first approximation.

In disregard of their interesting properties, foams are the least investigated amongst the dispersions when compared to emulsions or suspensions. In the recent years, the interest in foams has increased. This comes as no surprise since the application of foams has a lot of potential in a vast range of industries. From a scientific point of view, surfactant foams are well understood. Still, some fundamental questions remain or have only been answered recently. Especially the field of particle stabilized and responsive foams opened up a new field of research presenting new challenges.

The fact that solid particles can stabilize dispersions has been known for over a century. Ramsden and Pickering discovered the phenomenon for emulsions. Dispersions of a gas in a liquid can be stabilized in the same manner. Given proper wetting properties, particles can attach to a liquid/gas interface. This has been exploited for decades in the multi-billion dollar process of flotation. In other applications, the formation of a foam (or stable bubbles) from a particle dispersion may be highly undesirable. Unwanted bubbles may be formed during coating processes or foam can be produced in motor oils due to the high shear involved. In general, one has to understand the detailed mechanisms of foam stabilization in order to achieve the desired system properties, may it be high or low foam stability.

A foam can be interpreted as a highly hierarchical structure. In the present study, the smallest structural element are the surfactants and the nanoparticles. These can inter-

act with each other and change their interfacial behavior. The role of the surfactant is adopted by the alkyl amines and additionally by the in-situ hydrophobized nanoparticles. Increasing the length scale, the next level of hierachy is the gas/liquid interface. Due to the large amount of air incorporated into the foam, the properties of the interface strongly influence the properties of the foam. Here, the structure of the adsorption layer composed of amines and particles is of interest. Two foam bubbles are seperated by a lamella, the thickness of which is an order of magnitude larger than the particle size, initially. It should be kept in mind that, as the foam ages, the lamellae decrease in thickness due to drainage of the liquid phase. Another feature on the same length scale as the bubbles is the network structure made up of Plateau borders and vertices. The size of these structural elements is large compared to size of the amines and particles. Therefore, it can be treated as the bulk phase. In the end, the assembly of bubbles and the liquid network structure make up the macroscopic foam. From the previous explanation, it is clear that the macroscopic behavior is strongly linked to the interactions on the molecular level.

In this thesis, the different time and length scales of a particle stabilized foam are investigated. Relationships between microscopic and macroscopic behavior are established. A detailed understanding is gained about the mechanisms of foam stabilization by in-situ hydrophobized solid nanoparticles.

Chapter 5 deals with the interfacial adsorption properties of the used alkyl amines and the particles at the interface. Interfacial tension isotherms and x-ray reflecitvity studies are combined with theoretical considerations of the interfacial particle adsorption. A good understanding of the thermodynamics is obtained. A model is developed to enables reliable measurements of the particle contact angle.

In Chapter 6, the interaction of the amines and the particles is studied in the bulk phase by means of fluorescence spectroscopy. An interesting adsorption behavior of the amines onto the particles leading to hydrophobic attraction is shown. Additionally, the interfacial structure of the adsorbed particles is probed by micromechanical measurements. It can be deduced that there is a network structure at the interface for short adsorption times. Concerning the macroscopic foam behavior, it is found that increasing foam stability is mainly linked to increased particle-particle interaction in the bulk phase. The foamability is mainly linked to the particle network formation at the interface. The foam stability depends on the state of aggregation of the particles in the foam channels.

Dynamics of the foam structure and the particles in the foam are addressed in Chapter 7. Diffusing Wave Spectroscopy is applied to probe these dynamics. The amount of particles in the foam is determined by density measurements. It is shown that the evolution of the

foam structure is arrested above a certain amine concentration. This arrest is caused by gelation of the bulk phase. Below that concentration, the particles are dispersed in the foam liquid volume as single particles.

Chapter 2.

Scientific background

In this chapter, the fundamental scientific background is briefly summarized to create a basis for the understanding of the present thesis. More detailed explanations are given in the corresponding chapters.

The structural elements of the system are reviewed in Figure 2.1.

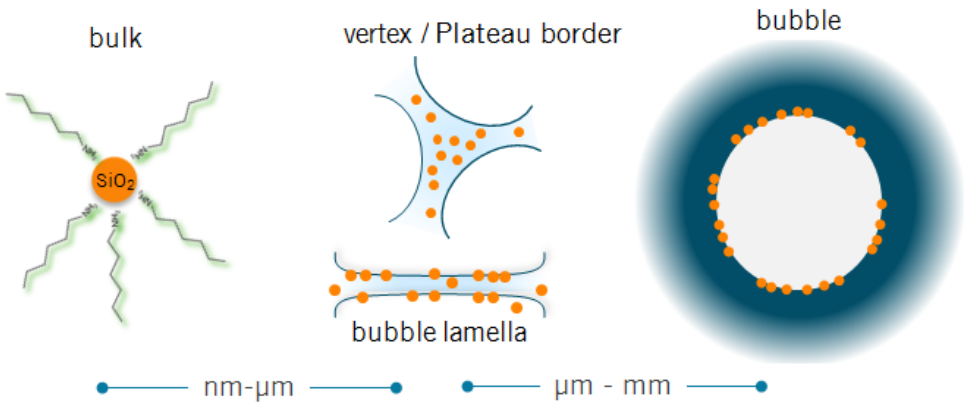

Figure 2.1.: The bulk liquid phase of the foam is a dispersion of silica particles onto which amines are adsorbed. Structural elements of the foam are the Plateau borders, four of which connect to form a vertex. Additionally, the lamellae separate two bubbles. The foam is composed of a collection of bubbles. Amines and particles may be adsorbed at all gas/liquid interfaces. An estimate of the size ranges of the structures is shown.

2.1. Particles versus surfactants

Particles and surfactants share the ability to stabilize interfaces, given suitable properties[1]. Surfactants are surface active by definition. Their actual surface activity depends on the kind of interface they should adsorb to. The surface activity of these molecules stems from the fact that two (or more) moieties of different hydrophobicity are present in the same molecule. In contrast, particles can be surface active although they might have a homogeneous surface[2,3]. In an aqueous phase, particles need a certain degree of hydrophobicity to render them surface active.

For surfactants, the adsorption energy is on the order of the thermal energy kT. That is, a dynamic adsorption equilibrium is established and there is a vigorous exchange of surfactant molecules between the bulk and the interface. The situation is different for hydrophobic particles. Their attachment energies can be orders of magnitude larger than

the thermal energy kT[4]. Thus, once a particle adsorbs at the interface, it will stay attached and no exchange with the bulk phase occurs. More elaborate discussion of particle hydrophobicity and adsorption energy can be found in Chapter 5.

In bulk, surfactants aggregate above the critical micelle concentration. In case of aliphatic surfactants, the structure of the micelles is globular to a first approximation. Particles do not form well defined structures upon aggregation. Usually, they form clusters or networks of particles which might be described by a fractal dimension rather than a simple geometric shape[5,6]. Figure 2.2 exemplarily shows two different possible structures of particles adsorbed at an interface. The concept of fractals is used in Chapter 6 in order to describe two-dimensional particle aggregates.

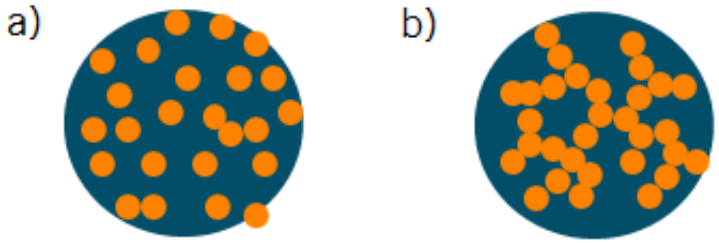

Figure 2.2.: Possible structures of interfacially adsorbed particles. a) Isolated particles b) Aggregated particles forming a (fractal) network

2.2. Surface forces

2.2.1. Surface tension

One of the most important properties that determines the fate of a foam is the surface tension. The surface tension of a pure liquid will be discussed first. Additional surface active components impose an additional force which will be discussed in the following section.

There is a common misconception about surface tension. In educational textbooks, it is often described as a force which arises due to an imbalance of forces normal to the interface. If that was the case, the system would not be in equlibrium. Actually, the surface tension acts tangential to the interface which is well described by Marchand et al.[7]

The stress tensor of the system is anisotropic at the interface within a few molecular diameters. If the system is conceptually divided into two subsystems, it is seen that this pressure difference is attractive. This attractive force is the surface tension.

From a thermodynamic point of view, the Gibbs free surface energy of a system is obtained by integrating the surface tension over the system's surface area. This energy is always positive. Hence, a thermodynamic driving force acts on the system to minimize its interfacial area.

Any foam is thermodynamically instable but the kinetic pathways for its destruction might be blocked, as will be discussed in the section about foam ageing below.

2.2.2. Surface pressure

As discussed above, surface tension is an attractive force parallel to the interface. Introducing surface active components will change the interfacial layer. The surface tension decreases as the amount of surface active material in increased. Since the surface tension γ is a negative pressure, a reduction of the original surface tension γ_0 has to be linked to the occurrence of a positive surface pressure Π. This is expressed by equation (2.1)

$$\Pi = \gamma_0 - \gamma \tag{2.1}$$

Most dilute particle and surfactant layers behave like a two-dimensional analogue of the ideal gas which obey the 2D-ideal gas equation:

$$\Pi A_m = RT \tag{2.2}$$

with the area per molecule A_m. Refined models can be found in the literature, these might include molecular or particle interaction, excluded volume, particle shape and other effects[8,9].

Surfactants usually show a surface pressure which is independent of the surface area. Consequently, the surface tension does not change as the system is compressed or extended as long as the rate of the area change is on the same order of magnitude as the rate of molecular exchange between interface and bulk. This is not the case for irreversibly adsorbed particles. As a particle layer is compressed, the particle density increases as they cannot escape into the bulk phase[10–12]. A higher particle density leads to a higher surface pressure or lower surface tension respectively.

The exact structure of the surface adsobed species determines the scaling of the surface pressure with the surface area change, as will be shown in Chapter 6.

2.2.3. Surface elasticity

The surface elasticity E determines how the surface tension changes with a relative change in interfacial area. It has been shown that surface elasticity is related to surfactant foam stability[13].

$$E = \frac{d\gamma}{dA/A} = \frac{d\gamma}{dlnA} \tag{2.3}$$

The surface elasticity is frequency dependent. For the slow evolution of a foam, only slow deformations are important.

In the case of particle stabilized foams, it has been shown that if the elasticity is large enough to fulfil the Gibbs stability criterion, the stability of a foam can increase drastically[14,15].

2.3. Foam ageing

Ageing of foams is a complex process. The three main mechanisms of foam destruction are drainage, coarsening and coalescence, conceptually shown in Fig.2.3. These processes are intertwined which complicates studies on exclusively a single mechanism[16].

2.3.1. Drainage

Drainage is the removal of the aqueous phase through the whole foam network by the action of gravity. It can only be fully suppressed in an environment like the international space station (ISS). The process of liquid removal from the foam leads to a thinning of the lamellae and the Plateau borders. The process alone does not destroy the foam. Theoretically there is no limit for the volume a foam occupies. Nonetheless, it has been shown that the amount of liquid held in the foam has a limiting value for low liquid fractions.

Drainage eventually leads to the formation of a foam which is wet at the bottom and dry at the top. The terms wet and dry refer to the amount of liquid held at a certain height. There is no official limit between a wet and a dry foam. Wet foams are characterized

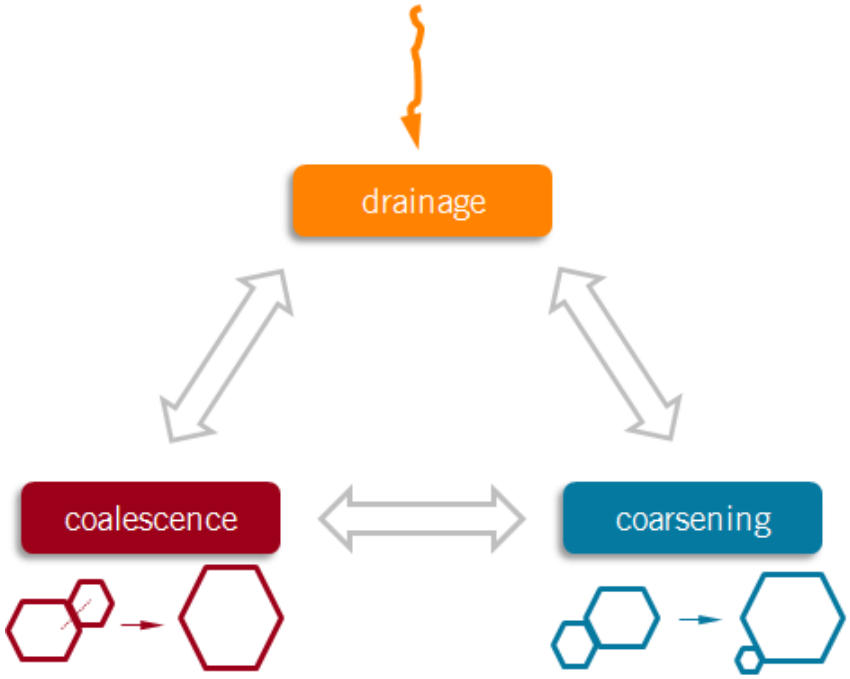

Figure 2.3.: Coupled mechanisms of foam ageing as explained in the text.

by smaller contact areas between the bubbles than in a corresponding dry foam. Dry foams are composed of highly polyhedral bubbles. In Chapter 7, moderately wet foams are investigated and the mean liquid fraction is determined by weighting of the foam.

Removal of liquid leads to thinner lamellae which are more likely to rupture. Furthermore, gas exchange accelerates with decreasing lamella thickness which in turn leads to faster coarsening.

The main amount if liquid drains through the Plateau borders. High liquid viscosity slows down this process. In particle stabilized foams, blocking of the Plateau borders can halt the drainage process[17]. It was shown that interfaces with high surface elasticity slow down drainage as they impose another flow profile (parabolic flow) than mobile interfaces (plug flow)[18].

2.3.2. Coarsening

Corsening is the increase in mean bubble size as the foam ages. The driving force of coarsening are differences of the gas pressures in the bubbles[19].

It was shown that coarsening can be stopped in particle stabilized foams with high surface elasticities[14,15]. When the Gibbs stability criterion is fulfilled, the pressure difference

between bubbles vanishes. Hence, there is no driving force to form larger bubbles at the expense of small bubbles.

Since coarsening requires gas exchange through the liquid phase, gases with low solubility slow down coarsening. This effect is charmingly demonstrated by the foam head on a Guinness beer. Guinness is tapped with higher amounts of nitrogen compared to regular beers for which carbon dioxide is used. Nitrogen has low solubility in water, hence the foam head becomes less prone to coarsening. A beer foam evolution study can be found in the literature[20].

The rate of gas exchange also depends on the effective area between bubbles. Therefore, dry foams coarsen faster than wet foams. The rate of gas solubilization also depends on the elasticity of the interfacial layer of surfactant as was shown for emulsion ripening[21]. Adsorbed particles restrict gas exchange by reducing the area available for gas exchange. As coarsening leads to larger bubbles, it leads to larger foam films between them, promoting bubble rupture.

2.3.3. Coalescence

It has been found that the rupture probability of foam films increases with their size. The exact mechanisms of foam film ruptures are not well understood[16,22]. Large film thicknesses are obviously more stable. Thin films are more prone to rupture by surface waves which locally pierce the film to create nucleation sites for film rupture[23,24]. High liquid viscosity or surface elasticity can dampen these oscillations to stabilize a lamella.

There is an internal film pressure, that prevents the lamella thickness to go to zero and eventually film rupture. This pressure is called the disjoining pressure. For surfactant stabilized films, its magnitude can mainly be described by the DLVO theory. Other effects like oscillatory forces are found when particles or micelles are introduced in the system[25–27].

2.4. Particle aggregation

According to Lifshitz theory, two identical materials that interact through a medium always attract each other[28]. This is the case for all dispersions, e.g. particles in aqueous environment or gas bubbles in a liquid. In the absence of repulsive forces, particles aggregate and gas bubbles coalesce. Aggregation can be prevented by steric or electroosmotic

stabilization. The DLVO theory is probably the most popular theory to explain these stabilization mechanisms.

All stabilization mechanisms rely on the introduction of a kinetic barrier that prevents contact of the interfaces. Detailed explanations can be found elsewhere in the literature[29].

Bare silica particles possess free SiOH groups on the particle surface. In alkaline aqueous media, these acidic groups dissociate to leave negative charges behind. The surface charge density increases with increasing pH[30]. Positively charged molecules like amines adsorb to these negative charges[31]. It is known that surfactant adsorption proceeds in different stages like shown in Fig. 2.4. For long chain surfactants, it is known that surfactant adsorption can be cooperative due to lateral interaction[32,33]. It is shown in Chapter 6 that amine-mediated hydrophobic interaction leads to particle aggregation in the present study with severe effect on the foam ageing.

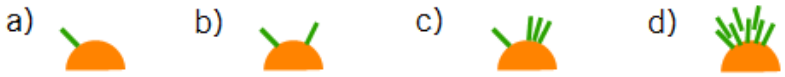

Figure 2.4.: a) Beginning of surfactant adsorption, b) Isolated Langmuir type adsorption, c) cooperative adsorption due to lateral interaction, d) double layer above CMC.

2.5. Probing of foam structure and dynamics

The internal structure of a foam is not readily accessible by optical means. Due to the opaque nature of a foam, often only its surface can be viewed. The vertical profile may be viewed through a transparent container. The structure can be examined nondestructively by x-ray radiography[20,34] or nuclear magnetic resonance[35]. Both techniques require that the foam structure is sufficiently stable on the time scale of the experiment. Changes of the foam structure during the measurement complicate the image reconstruction or even render it impossible. Due to these limitations, only very stable foams have been investigated with these techniques.

To investigate foam dynamics, one has to overcome the same obstacles as in the study of the foam structure. Even though the structural changes at the wall surface can be viewed, they may suffer from wall effects. Hence, they might not reflect the processes inside of the foam[36,37].

The commonly used reference foam is Gillette regular shaving foam. This might seem amusing but its worldwide availability and reproducibility is excellent, making it a suitable reference. It has been used for many fundamental studies of foam ageing. We can distinguish between continuous changes like coarsening and abrupt changes like bubble rearrangements or coalescence events as described earlier. Both proceed on different time scales and can be studied by Diffusing Wave Spectroscopy. This technique is a great tool to nondestructively study foams as will be demonstrated in Chapter 7.

Chapter 3.

Methods and Apparatus

3.1. Density measurements

When the particles in a dispersion have a different density than the dispersing medium, it is possible to determine their fraction in the dispersion. Measurements with high precision were necessary because small changes in the particle concentration were supposed to be quantified. Therefore, an oscillating U-shaped tube was used to measure the dispersion bulk density.

A U-shaped tube is excited to oscillate at its eigenfrequency. The oscillating volume is precisely defined and only depends on the geometry of the tube. When the tube is filled with a liquid, the tube's eigenfrequency changes, as the mass of the oscillating volume changes. The shift in eigenfrequency is measured electronically. With proper calibration, it is straightforward to convert the oscillation frequency to the density of the liquid.

A calibration curve with dispersions of known particle concentration is shown in Fig. 3.1. The dependence of the bulk density on the particle concentration is perfectly linear. Hence, the particle concentration can be measured precisely.

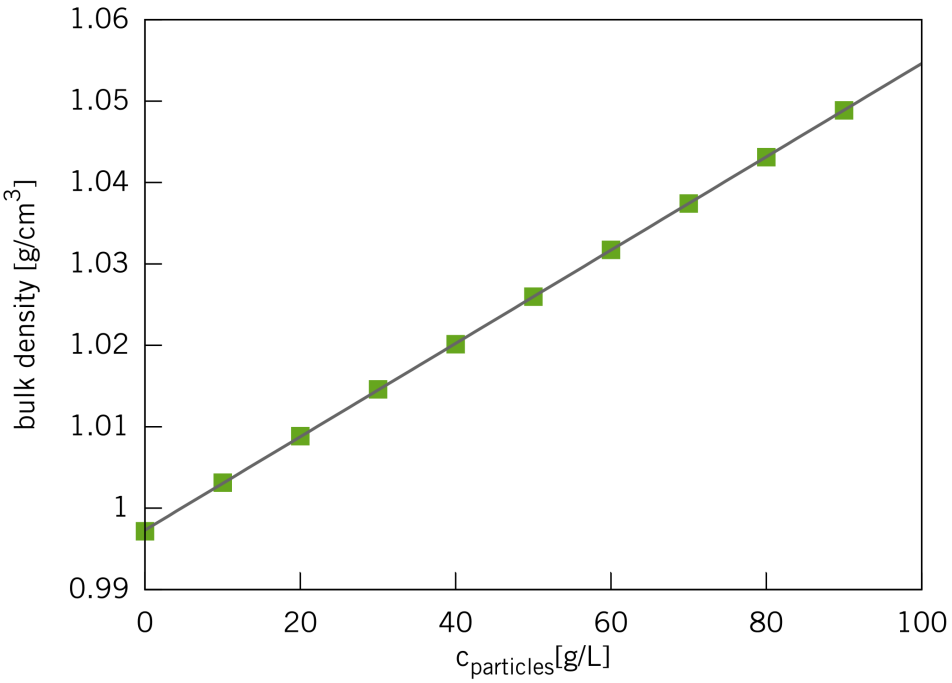

Figure 3.1.: Linear dependence of the bulk density of the particle suspensions on the mass concentration.

3.2. Zeta Potential / Electrophoretic Mobility

When a charged surface is submerged in a liquid containing ions or charged surfactants, these charged species can adsorb to the surface. There will be an electric potential gradient from the surface of e.g. a particle into the surrounding medium. When the particle moves in the liquid a shear plane above the surface forms. Ions closer to the particle than the shear plane will be dragged with the particle as if they belonged to the particle. The ζ-Potential is the electric potential at exactly this shear plane. It cannot be measured directly and depends on the applied theoretical framework.

The electrophoretic mobility can be measured directly. When an electric field is applied to a dispersion of charged particles, the particles start to move towards an electrode. The direction depends on the sign of the charge on each particle. This movement is measured by Laser Doppler Velocimetry and Phase Analysis Light Scattering.

When a particle is not subjected to an external electric field, the light scattered off the particle has almost exactly the same frequency as the incident light wavelength. Doppler effects are negligible. When the particle is in motion, the situation changes. The scattered light has a different frequency than the incident light. When the scattered light is recombined with unscattered light, interference will lead to a beating with frequency $\nu_{beat} = |\nu_{scat} - \nu_{inc}|$. The relation between the beat frequency ν_{beat} and the particle velocity v_p is:

$$\nu_{beat} = \frac{2v_p}{\lambda} \sin\left(\frac{\theta}{2}\right) \tag{3.1}$$

with the scattering angle θ and the laser wavelength λ. In addition, the used instrument (Malvern Zetasizer ZS) uses a patented technique that analyzes the phase of the beating with respect to an internally produced reference frequency. The electrophoretic mobility u_e is calculated by $u_e = v_e/U$ with the applied voltage U. From the electrophoretic mobility, the ζ-potential can be calculated:

$$\zeta = \frac{3u_e\eta}{2\epsilon f(\kappa r)} \tag{3.2}$$

with the solvent's dynamic viscosity η, the solvent's dielectric constant ϵ and the Henry function $f(kr)$. For the system studied in the present work, the Henry function takes the value of 1.5 (Smulochowski approximation).

3.3. X-Ray Reflectivity

X-ray Reflectivity (XRR) probes an interface for changes in the electron density normal to the interface. A typical setup is shown in Fig. 3.2. An x-ray source produces a divergent beam, which is collimated by special x-ray optics. The collimated beam then impinges on the sample, which can be a solid or a liquid interface. The intensity of the reflected beam is recorded by means of a suitable detector.

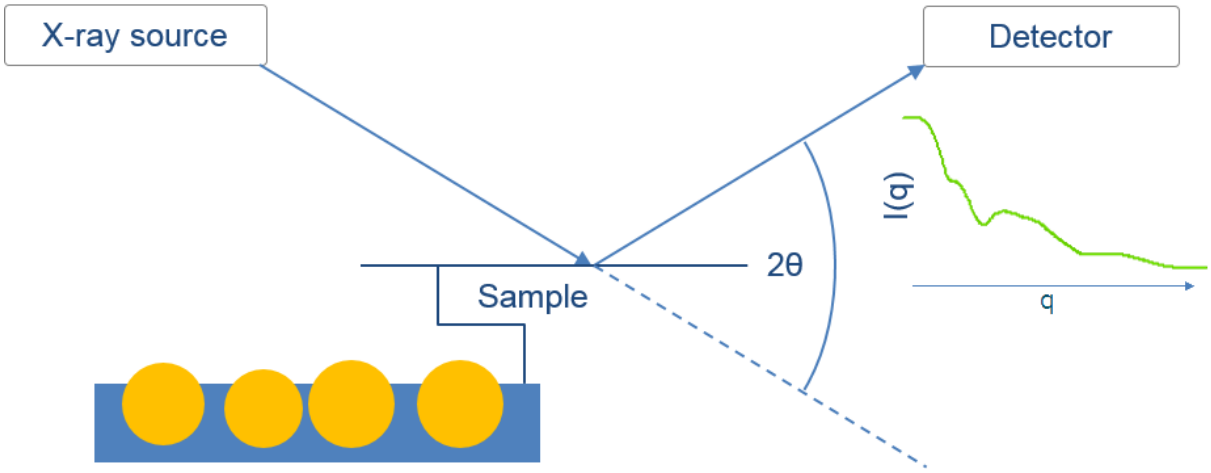

Figure 3.2.: Setup of a x-ray reflectivity experiment. Monochromation optics are used in front of the sample but are omitted in the sketch.

Below the critical (incidence) angle, the x-rays do not penetrate the sample surface and the beam is totally reflected off the interface. Above the critical angle, the beam starts to penetrate the sample. The high energy of the x-ray beam is able to excite all electrons present in the atoms. The total x-ray scattering cross section of an atom is therefore proportional to its atomic number Z. The excited electrons start to radiate themselves at the excitation frequency (elastic scattering). This elastic scattering process is the most relevant process in this study. X-rays may also be absorbed or inelastically scattered which will not be discussed here in detail.

Almost all experiments in this study were conducted in the 2θ scan mode in specular condition. The angle 2θ is scanned through a proper range while recording the reflected intensity.

For a sample composed of a homogeneous, infinitely thick layer of a certain material, the reflectance R(q) of the beam is expressed by:

$$R(q) \approx \frac{16\pi^2\rho_l^2}{q^4} \tag{3.3}$$

Here, ρ_l is the electron density difference of the continous phases and q is the scattering vector. A Gaussian surface roughness will lead to an additional exponential decay factor $\exp(-\sigma^2 q^2)$ with the Gaussian roughness of σ.

For samples with a structured interface, the reflected intensity cannot be described by an analytical function of 2θ. Still, the reflected intensity can be calculated by matrix methods. To do so, the sample is described as a stack of layers with defined electron density. The transmittance and reflectance properties of each layer are known. Therefore, the reflectance properties of the sample can be calculated. In order to obtain information from the measured reflectance curve, the theoretical model is systematically varied and the theoretical reflectance of the sample is calculated. This procedure is continued until an acceptable agreement between experimental data and model values is obtained.

Tools for the modeling of the sample reflectance are Parratt or Motofit, of which Motofit was used because it is more flexible for programming fitting models. The program code that was used to analyze the data of this study can be found in Appendix A.1.

3.4. Axisymmetric Drop Shape Analysis (ADSA)

Axisymmetric Drop Shape Analysis is used to determine the interfacial tension γ between two fluids. In this study, only liquid/gas interfaces were studied. The setup is shown schematically in Fig.3.3. A droplet of liquid is suspended from an orifice, e.g. a dosing

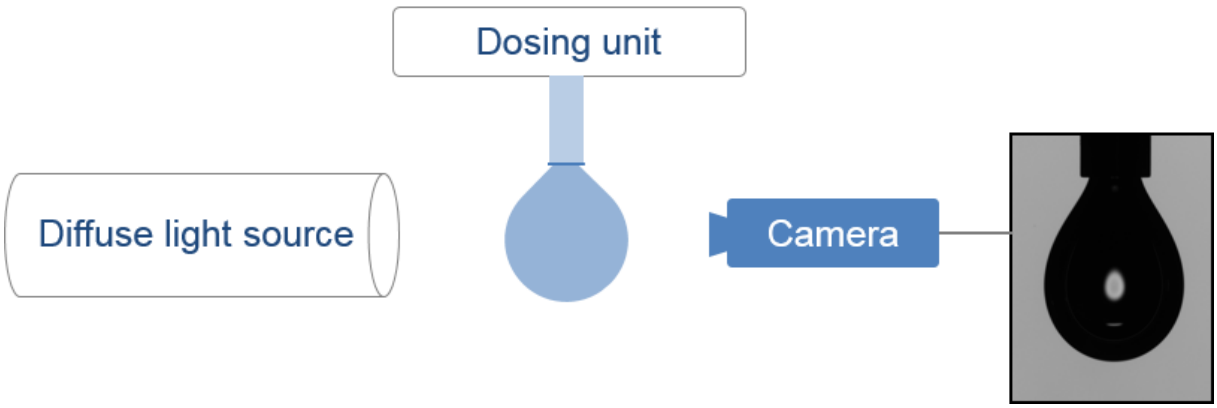

Figure 3.3.: Typical setup of an ADSA experiment.

needle. Alternatively, a bubble of air is created from a bent dosing needle. There are two main forces acting on the liquid. The surface tension acts on the droplet to minimize the surface/volume ratio. Gravity acts on the liquid to elongate the droplet, thereby increasing the surface/volume ratio. The capillary length λ_c is a measure for the dimension, at which

surface tension and gravitational forces are comparable. For a reliable measurement, the diameter of the droplet should be in the range of the capillary length.

$$\lambda_c = \sqrt{\frac{\gamma}{\rho g}} \tag{3.4}$$

with the density of the liquid ρ and the gravitational acceleration g. For the dispersions used in the study, the capillary length is in the range of ≈ 2 mm. The shape of the droplet can be calculated by means of the Young-Laplace-equation:

$$\Delta p = -\gamma \nabla \cdot \hat{n} \tag{3.5}$$

with the pressure difference across the interface Δp and the unit normal $\hat{n}$ pointing out of the surface. The pressure within the droplet varies in the vertical z-direction due to the presence of the gravitational field. This pressure is balanced by the curvature pressure on the right hand side of eq.(3.5). In turn, this means that the curvature of the droplet depends on the z-position within the droplet.

$$\Delta p(z) = -\gamma \left(\frac{1}{R_1(z)} + \frac{1}{R_2(z)} \right) \tag{3.6}$$

where R_1 and R_2 are the two principal curvatures of the interface. The droplet shape is recorded with a video camera and the image is processed to yield the outline of the droplet shape. Equation (3.6) is used in the supplied software to numerically fit the shape of the droplet to the measured outline which gives the surface tension γ.

3.5. Photon Correlation Techniques

Dynamic Light Scattering (DLS) and Diffusing Wave Spectroscopy (DWS) are photon correlation techniques. Both techniques allow to measure the dynamics of scatterers in a matrix. The techniques are nondestructive and can be applied to a large variety of samples. DLS is suitable for weakly scattering, nearly transparent samples, where single scattering events can be presumed. In contrast, in DWS the samples are required to be strongly scattering with multiple scattering events. Both techniques require the analysis of the fluctuation in the scattered light intensity. Dynamics within the sample produce transient deviations in the scattered light intensity $I(t)$ from the mean scattered intensity $\langle I(t) \rangle$. The brackets indicate the time average of the data.

A very common way to analyze the scattered intensity time series is to calculate the

normalized intensity autocorrelation function $g_2(\tau)$.

$$g_2(\tau) = \frac{\langle I(0)I(\tau)\rangle}{\langle I\rangle^2} \tag{3.7}$$

with the lag-time τ that denotes the time shift of the original signal used in the autocorrelation.

There are software and hardware implementations to measure $g_2(\tau)$. For most applications dealing with the fast dynamics of nanoparticles, specialized hardware correlators are used.

The variable which is directly connected to the motion of the scatterers is the normalized electric field autocorrelation function $g_1(\tau)$.

$$g_1(\tau) = \frac{\langle E(0)E(\tau)\rangle}{\langle E\rangle^2} \tag{3.8}$$

with the electric field strength $E(t)$. Currently, it is not possible to measure $g_1(\tau)$ directly due to loss in phase information. Fortunately, it is possible to calculate g_1 from g_2 in many cases. When the signal arriving at the detector obeys Gaussian statistics, it is possible to apply the Siegert relation:

$$g_2(\tau) = 1 + \beta|g_1(\tau)|^2 \tag{3.9}$$

Here, β is an instrument specific factor, dependent on the number of coherence areas covered by the detector. In case of a large number of scatterers in the probed volume element, the signal arriving at the detector is the sum of many scattering signals. Each scattered wave itself is a random variable. The central limit theorem states that the sum of a large number of arbitrarily distributed random variables obeys Gaussian statistics. In all experiments, the number of scatterers and/or the probed volume was large enough to apply the Siegert relation.

Dynamic Light Scattering is an ideal technique to investigate diluted bulk dispersions. Diffusing Wave Spectroscopy allows to investigate foams because they are strongly scattering. The discussion in this work is limited to scattering of colloidal dispersions and foams. To check which method is suitable for a system, the fraction of unscattered transmitted light T can be estimated using the Lambert-Beer-law:

$$T = \frac{I_t}{I_0} = \exp(-\frac{d}{l_{scat}}) \tag{3.10}$$

with the unscattered transmitted intensity I_t, the incident intensity I_0, the sample thickness d and the mean free path length l_{scat} between two scattering events. For $T > 0.95$, DLS is applicable. Turbid samples with $T < 0.05$ are probed by DWS. Possible stategies to adjust a sample into one of the two regimes are dilution and/or increasing the sample thickness.

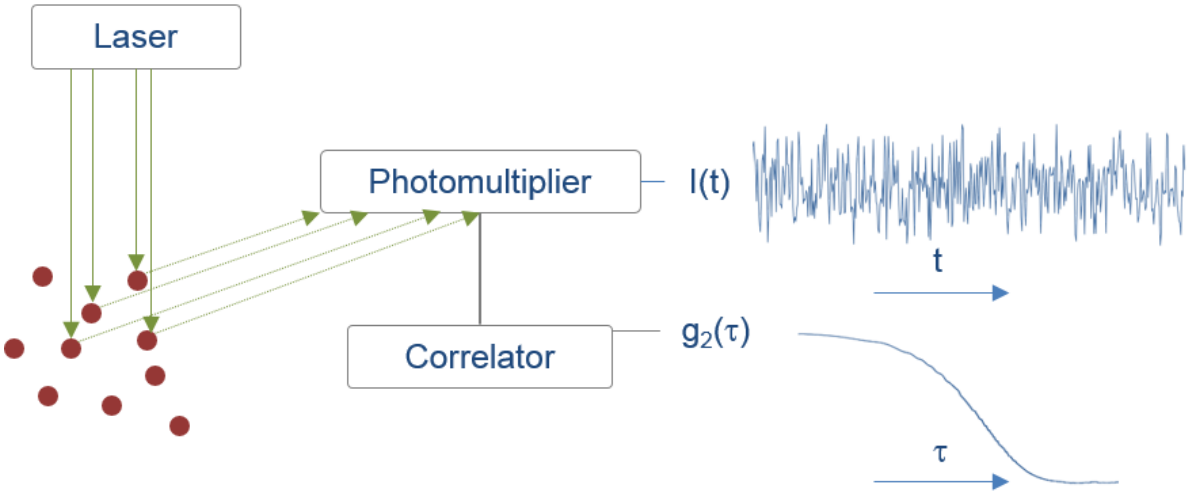

Figure 3.4.: Schematic setup of a DLS or DWS experiment. The correlation procedure of the data is identical in both cases. In DWS, the sample is probed in transmission (not shown).

3.5.1. Dynamic Light Scattering (DLS)

DLS is routinely used to characterize homogeneous particle dispersions. A typical setup is shown in Fig.3.4. A laser operating in constant wave mode is focussed into the sample. The detector is placed at an angle θ with respect to the transmitted beam. The scattered light is detected by a photomultiplier and the amplified signal is processed by an autocorrelator to yield $g_2(\tau)$. As described above, $g_1(\tau)$ is calculated by Eq.(3.9).

Monodisperse particles subjected to Brownian diffusion produce an electric field autocorrelation function with a simple exponential decay:

$$g_1(\tau) = \exp(-\Gamma\tau) \tag{3.11}$$

with the decay rate Γ. For a polydisperse particle dispersion, equation (3.11) is substituted by

$$g_1(\tau) = \int_0^\infty G(\Gamma)\exp(-\Gamma\tau)d\Gamma \tag{3.12}$$

with the normalized decay rate distribution function $G(\Gamma)$. In the case of Brownian diffusion of the scatterers, a simple relation between the decay rate Γ and the diffusion coefficient D exists:

$$\Gamma = Dq^2 \tag{3.13}$$

with the magnitude of the scattering vector q, calculated by

$$q = \frac{4\pi n}{\lambda} \sin\theta \tag{3.14}$$

Here, n denotes the refractive index of the dispersing medium, λ the probing laser vacuum wavelength and θ the scattering angle.

The hydrodynamic particle radius R_H can be calculated from the diffusion coefficient D via the Stokes-Einstein equation:

$$R_H = \frac{k_B T}{6\pi\eta D} \tag{3.15}$$

Hence, the particle radius can be determined from a measurement of g_1 for weekly scattering dispersions.

3.5.2. Diffusing Wave Spectroscopy (DWS)

The setup of DLS and DWS are quite similar. The main difference is the detection (or scattering) angle. In most cases, DWS is performed in 0° transmission or >150° backscattering geometry. The following discussion will be limited to measurements performed in the transmission geometry. In the ideal case, every photon travelling through the sample has been scattered multiple times before arriving at the detector. In such a case, any photon performs random walk while passing the sample. The random walk can be described by a diffusion equation, hence the name "diffusing wave".

For a colloidal dispersion, the mean free path length l_c between two scattering events can be calculated from the scattering cross-section of the scatterers σ_{scat} and their number concentration n:

$$l_c = \frac{1}{n\sigma_{scat}} \tag{3.16}$$

A random walk step length l_c^* is defined as the length, after which the direction of the incoming and outgoing photon are uncorrelated. In other words, it is impossible to predict the direction of a photon after it travelled the distance l_c^* even if the initial direction was known. For a Rayleigh scatterer, the direction is randomized after a single scattering

event. It should be noted that this is generally not the case for strong scatterers. Mie theory permits to describe the angle dependent scattering properties of spherical particles of arbitrary size and refractive index. For simplicity, the weak scatterers will be referred to as "small particles". It is assumed that in any case, a significant refractive index difference between particle and surrounding medium exists. In analogy, strong scatterers will be referred to as "large particles".

The angle dependence of the angular scattering power distribution for a weak and strong scatterer is shown in Fig. 3.5. The scattering of large particles is strongly directed into certain angles. For a Rayleigh scatterer, the scattered intensity is equal for all scattering angles (for VV geometry). The figure also shows that the larger particle scatters stronger than the smaller one. Further details of the DWS formalism and theory will be discussed in the corresponding Chapter 7.

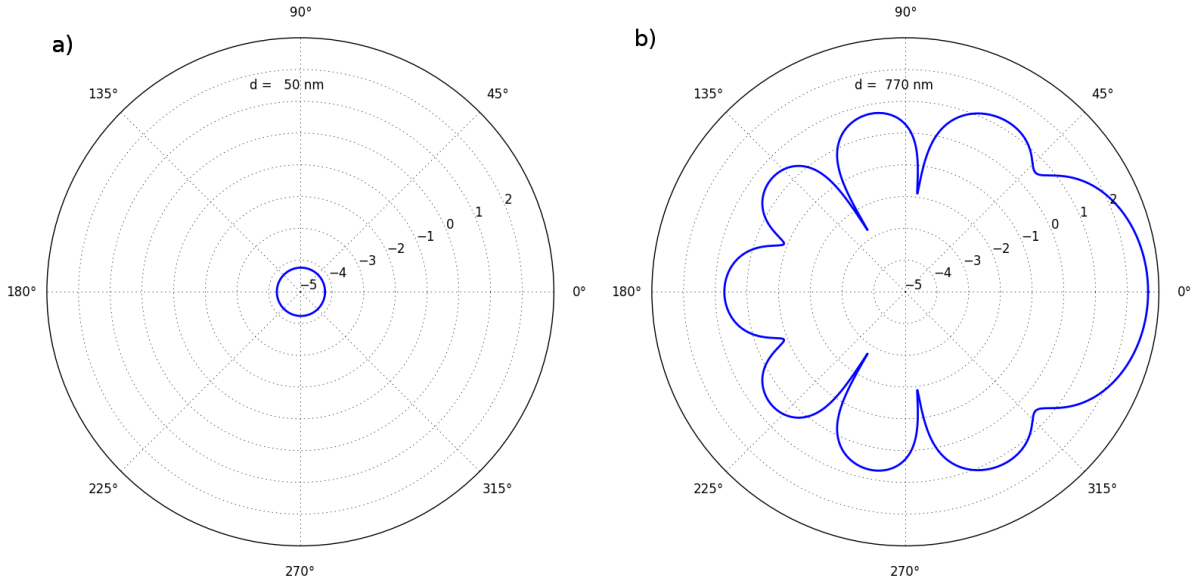

Figure 3.5.: Angular distribution of scattered light for a) a Rayleigh scatterer of diameter 70 nm. b) a Mie scatterer of diameter 770 nm. The intensity is in arbitrary units and scaled logarithmically.

Chapter 4.

Experimental section

4.1. Materials and preparation

4.1.1. Materials

The materials used in this study are listed in the table 4.1. High purity HCl and NaOH standard solutions were used for pH adjustments. All chemicals were used without further purification.

4.1.2. Preparation of suspensions

Unbranched alkyl amines of chain lengths C_5 to C_8 interact with silica nanoparticles of 28 nm in diameter.

It was shown that short chain surfactants bearing protonizable functionalities perform most efficiently, in terms of foaming particulate dispersions, when the pH is close to their pK_A value. The pK_A of the alkyl amines, irrespective of chain length, is 10.63. Consequently, the pH was adjusted at a value of 10.4. At this pH value, about 80 % of the amino functions are protonated, i.e. positively charged. In order to assure constant pH and approximately constant ionic strength, methylamine was used as a buffer. Combinations of silica particles and methyl amine alone did not show any foamability, as the methylamine is not surface active but mainly acts as a monovalent salt ion at the investigated pH value.

Stock solutions of the amines were prepared and adjusted to pH 10.4 via the addition of 1M HCl. The stock concentrations were 0.5 M for pentyl amine and hexyl amine, 0.05 M for heptyl amine and 0.02 M for octyl amine. For the longer chain amines (C_6 to C_8), a clear

Table 4.1.: List of used chemicals with their respective supplier and purity

Chemical	Purity	Supplier
Methylamine 40 % in H_2O	$\geq$ 97 %	BASF (free of charge)
Pentylamine	99 %	Sigma Aldrich
Hexylamine	99 %	Sigma Aldrich
Heptylamine	99 %	Sigma Aldrich
Octylamine	99 %	Sigma Aldrich
Ludox TMA 34 % in H_2O	$\geq$ 98 %	Sigma Aldrich

solution was only obtained when adjusting to the final pH. A silica stock solution of 50 g/L Ludox TMA containing 0.1 mol/L methylamine was prepared. A 1M methylamine solution was added dropwise to a silica dispersion which was previously diluted with ultrapure water. During the preparation, the pH was monitored. Small amounts of 1M HCl were added dropwise, when needed, to ensure the pH was not increased above 10.5. The final volume was adjusted in a volumetric flask. The final adjustment of the volume did not affect the pH.

To prepare the samples, the amine stock solutions were diluted to twice the desired final sample concentration and then mixed 1:1 with the silica dispersion to achieve the desired amine concentration and a silica concentration of 25 g/L. Mixing was done on a vortex mixer which avoided excessive foam production during the sample preparation.

4.2. Experiments and apparatus

4.2.1. Zeta potential / Electrophoretic mobility

The electrophoretic mobility was measured with a Malvern Zetasizer ZS. Zeta potential values were calculated from the particle mobilities by applying

$$\zeta = \frac{u\eta}{\epsilon_0 \epsilon_r f(\kappa r)} \tag{4.1}$$

Here, u is the electrophoretic mobility, η the dynamic viscosity, $\epsilon_0\epsilon_r$ the dielectric constant of the medium and $f(\kappa r)$ is the Henry function. Due to the fixed buffer concentration of 0.05 mol/L and considering the protonated fraction of 0.8, the maximum Debye screening length in the system $1/\kappa$ can not exceed 1.5 nm. Given a particle radius of 14 nm for the particles used in this study, $\kappa r >> 1$ and the function $f(\kappa r)$ can be approximated as 3/2 (Smoluchowski approximation). It should be noted that the Debye length is comparable to the length of the alkyl amine molecules. This implies that zeta potential changes can be used as a measure of a change in the surface charge of the silica.

4.2.2. Pyrene Fluorescence

A stock solution of $3.7 \cdot 10^{-5}$ M pyrene in ethanol was prepared. 20 μL of the pyrene stock solution were added to 2 mL of the sample dispersions. The resulting dilution of the sample dispersions was neglected. The fluorescence spectra were measured with a

Hitachi F-4500 spectrometer at an exitation wavelength of 334 nm. A Quartz cell of 10x10 mm was used and the fluorescence signal was detected at 90° from the incident exitation beam.

4.2.3. X-ray Reflectivity (XRR)

Samples for the X-ray Reflectivity measurements were produced by mixing silica stock solutions of 50 g/L with alkyl amine solutions of twice the final desired sample concentration. Mixing was performed on a vortex mixer with 1500 rpm to avoid excessive foam formation. The XRR measurements were performed on a Bruker D8 reflectometer.

A closed measurement cell was used for the experiments. The sample was gently filled into a circular trough machined from PTFE with a diameter of 60 mm. The interface was leveled by gravity. Present oscillation were damped with an active damping device sitting below the sample cell. The sample surface was accessible by X-ray transparent windows made of Kapton foil. Slits of 0.1 mm were used in front of and behind the sample.

A footprint correction was performed on the experimental data before the fitting procedure. The beam profile was measured to be Gaussian.

4.2.4. Interfacial Tension (IFT)

Droplet respectively bubble formation was done as described for the surface pressure isotherms.

The interfacial tension was calculated by axisymmetric drop shape analysis. For the interfacial tension measurements, at least 4 droplets were produced and each droplet was measured 10 times. The time dependent measurements were performed in similar manner. Slightly smaller droplets were chosen, so the decay in IFT did not lead to detachment of the droplet. During the time span of 30 min, the interfacial tension was determined each second by ADSA. Static interfacial tension measurements were done as soon as the droplets were formed.

4.2.5. Surface Pressure Isotherms

Surface pressure isotherms were recorded with a Dataphysics OCA 15 instrument. Pendant droplets of the sample dispersions were dosed via a stepper motor controlled syringe

pump. The droplet size was chosen at approximately 80 ± 5% of the maximum droplet size before the drop detached from the syringe. The maximum droplet size was determined before the actual measurements. A dosing needle of outer diameter 1.35 mm was used. The densities of the dispersions were measured with an Anton Paar DMA 4100 densiometer.

The droplets were formed quickly within a time span of 3-5 s and after 90 s the liquid was retracted at a speed of 0.06 mL/s. The interfacial tension was extracted by image analysis and fitting of a Laplacian droplet profile.

4.2.6. Dynamic Light Scattering (DLS)

Samples of a silica concentration of 5 g/L were used to study the concentration dependent aggregation behavior. The samples were prepared and left to age undisturbed for three days. Dynamic light scattering data were recorded using an ALV/CGS-3 compact goniometer system equipped with an ALV-7004/USB correlator. Temperature control was provided by a Huber Compatible Control thermostat. The laser wavelength was 632.8 nm, and the laser light was polarized perpendicularly to the scattering plane. Intensity autocorrelation functions $g_2(\tau)$ were recorded at a scattering angle of 90°. The Siegert relation was used to calculate the field autocorrelation function $g_1(\tau)$. Second order cumulant analysis was used to extract the relaxation rates Γ of the autocorrelation functions. With known Γ and scattering vector q, the particle diffusion coefficient D was calculated by $D = \Gamma/q^2$. Applying the Stokes-Einstein equation yielded the apparent hydrodynamic particle radius R_h

$$R_h = \frac{k_B T}{6\pi\eta D} \tag{4.2}$$

with the thermal energy kT and the dynamic dispersion viscosity η.

4.2.7. Diffusing Wave Spectroscopy (DWS)

For the experiments, 4 mL of sample dispersion with a silica mass concentration of 50 g/L were whipped for 60 s with a hand-held milk frothing device. Afterwards, the sample was quickly transferred to the sample cell. A flat glass cell of 5 mm thickness was used. The cell was 50 mm in diameter in order to ensure no light escapes through the sides. Only samples with sufficient foam life-times and proper handling properties (stiffness) could be assessed. The sample cell was weighted after the sample was inserted, which allowed to

calculate the mean liquid fraction Φ_l of the foam. Diffusing wave spectroscopy measurements were performed using an ALV goniometer system equipped with an ALV/LSE-5004 correlator. Temperature control was provided by a Huber Compatible Control thermostat. The incident laser beam (Nd-YAG, 532nm) was expanded to illuminate an area of approximately 4 cm^2. All measurements were performed in transmission geometry. Apertures were used to collect scattered light from an area roughly corresponding to a speckle. A photomultiplier tube connected to the autocorrelator yielded the normalized intensity autocorrelation function $g_2(\tau)$. Consecutive measurements of 120 s were performed until either the foam collapsed or a maximum time of 30 min was reached. Data analysis is heavily based on the model presented by Crassous and Saint-Jalmes. All samples were freshly prepared and measured three times. The samples were measured within the first 10 minutes after preparation. As the transmission increased more than 30 % from the starting value, the data were not used for further analysis.

4.2.8. Particle Extraction and Foam Volume

In order to quantify the amount of particles in the bulk dispersion, density measurements were performed with an Anton Paar DMA 4100 density meter. Bulk density measurements of silica dispersion samples with known mass concentration β revealed a perfectly linear dependence of bulk density on the mass concentration of particles. Sample volumes of 6 mL were used for the extraction experiments. The silica mass concentration was 25 g/L for all experiments. Gentle vortex mixing was crucial to avoid foam formation during the mixing process. Subsequently, 3 mL of the prepared sample dispersion were separated and the dispersion bulk density was measured. The remaining 3 mL of the sample in the test vial were vigorously shaken by hand for 30 s. Immediately after foaming, the produced foam volume was measured with the help of the graduation on the vial. As the foam drained, 1.5 mL of the dispersion were sampled from the bottom of the vial with a syringe and needle. Again, the bulk density was measured. The reference measurements with known mass concentrations were used to determine the silica mass concentration β of the unfoamed and foamed dispersion. The extracted fraction α of particles was calculated with the following equation.

$$\alpha = \frac{\beta_{unfoamed} - \beta_{foamed}}{\beta_{unfoamed}} \tag{4.3}$$

4.2.9. Macroscopic Foamability

To monitor the foam stability, 2 mL of the sample dispersions were transfered to 12 mL vials and vigourously shaken by hand for 30 s. All samples were shaken by the same person. The reproducibility of the shaking procedures was confirmed with three identical samples that were foamed one after the other. Immediately after the foaming procedure, the samples were monitored with a Canon EOS 5D Mark II. Pictures were taken every 120 s for up to 24 h. The foam half life was defined as the time it took for the foam to collapse to half its initial height. The half life was determined by visual inspection of the series of images taken at regular intervals.

Chapter 5.

Particle Adsorption and Contact Angle

Abstract

This chapter deals with the adsorption behavior of the surface active compounds used in this study. Here, the most important surface active species are the silica nanoparticles, which are hydrophobized by adsorbed short-chain amines. The short chain amines without nanoparticles are surface active themselves but do not show any substantial foamability or foam stability. In this chapter, the state of adsorption, especially the contact angle and the amount of adsorbed particles will be discussed. The here presented foam lamellae show only weak stability against rupture. Hence, the investigated system was simplified to a single air/suspension interface. From the performed static interfacial tension (IFT) measurements, the presence of particles at the interface cannot be concluded since they do not affect the interfacial tension at the studied timescale. Nonetheless, x-ray reflectivity (XRR) experiments clearly prove the adsorption of the nanoparticles to the air/suspension interface. For the studied system, the interface becomes almost fully packed. It was possible to measure the particle contact angle by means of XRR. The contact angles were found to be in the range of 30 to 50°, so the largest part of a particle stays immersed in the aqueous medium. Additional theoretical calculations of the amount of adsorbed particles revealed that a thermodynamic treatment of the adsorption equilibrium is highly dependent on the surface charge density. During the process of foam formation, a massive amount of air/suspension interface is formed within a short period of time. This fast formation is supposed to produce an interfaces far from the adsorption equilibrium, so kinetic adsorption effects may have to be considered in the actual foam.

Design of experiments, measurements, data analysis and interpretation were done by the author.

5.1. Introduction

The adsorption of surfactant modified particles at a fluid interface is of large interest in the fabrication of well defined particle monolayers. With respect to the stabilization of emulsions, the oil/water interface is investigated frequently[1,11,38–42]. Considering foams, the air/water interface is of great interest. Most studies focus on the interaction of classical long-chain surfactants (alkyl chain length ≥10 carbon atoms) with nanoparticles[10,12,43–45]. It has been recognized that colloidal particles share some properties with surfactants[1].

The most striking similarity is their surface activity, given proper hydrophobicity. A dynamic equilibrium establishes when the adsorption rate of the surfactant equals the desorption rate. Hence, there is a steady exchange of molecules at the interface. In the case of adsorbed particles, the adsorption can be irreversible. This is usually the case when the particle dimensions exceed 10 nm and the particles are moderately hydrophobic.

The hydrophobicity of a sherical colloidal particle can be expressed by the contact angle. Contact angles are usually measured through the water phase. An angle of 0° means the particle is fully wetted by the water phase, 180° means full wettability by the organic or gas phase. At 90° the particle is sitting in between the phases, protruding into both fluids with the same interfacial area.

Some particles are hydrophobic due to the material they are composed of. For example, polymeric polystyrene particles are hydrophobic[46–49]. Inorganic oxides like silica can be rendered hydrophobic by reacting organosilanes onto their surfaces[50,51]. As stated above, a very common method to hydrophobize particles is by adsorption of surfactant molecules. In the present study, short chain surfactants were used. Fewer studies of this type of surfactant-particle complexes are published[52] in comparison to classical surfactants. Nonetheless, short chain alkyl amines are capable of hydrophobic interaction or at least hydrophobization of nanoparticles[53–56]

Various theoretical models for particle adsorptions at a fluid interface were proposed in the literature[8,57–60]. Particles at an interface interact through a variety of forces. Electrostatic forces can act through both phases of the interface. Depending on the dielectric properties, dipole-dipole interaction might be induced, which is of importance for micrometer-sized particles. Van der Waals forces are present, regardless of colloid size. Additional interactions like capillary interaction can be neglected for nanoparticles like the ones used in this study. These effects are mediated by the deformation of the interface which can be neglected for nanoparticles.

The situation becomes more complicated when the particles do not have homogeneous wetting properties. In such a case, more parameters than the contact angle are nescessary to describe the particle wetting[61,62].

However, the particle contact angle is of great importance to understand the particle behavior. The nanoscopic size of the used nanoparticles prohibits the use of microscopic techniques to investigate the interface. Some attempts have been made to measure the contact angle by means of ellipsometry[63–66]. The results highly depend on the calculation method of the effective refractive index of the layers. Hence, this method can only give

an estimate of the particle contact angle. Direct methods have been developed, which use gelation of freezing of the dispersing phases. The phases are then separated manually and probed by means of i.e. electron microscopy[67–69] or atomic force microscopy[70]. Recently, x-ray reflectivity has been applied to measure the particle contact angle at the oil/water interface[71]. These measurements were performed at a high performance x-ray beamline.

In the present study, the interface was investigated by interfacial tension measurements. The amines and the amine-particle complexes were investigated. An x-ray reflectivity model was set up to extract the particle contact angle from the XRR curves.

The results from the XRR measurements are discussed together with theoretical calculations to give insight into the adsorption themodynamics of the particles. Good estimates of the amount of adsorbed particles are obtained by comparison of theory and experiment. Furthermore, the transfer of the result towards foams is discussed.

5.2. Results

5.2.1. Interfacial Tension (IFT)

Interfacial tension was measured on the alkyl amine solutions without nanoparticles and the suspensions of in-situ hydrophobized particles. Axisymmetric Drop Shape Analysis (ADSA) was used to obtain the interfacial tensions. The adsorption isotherms of the samples are shown in Figure 5.1. The interfacial tension decreases with increasing amine concentration for all amine chain lengths. The decay of the interfacial tensions starts at lower concentrations for longer alkyl chain lengths. No plateau was found in the studied concentration range as it is known for classical surfactant systems. While the C_5 amine was completely miscible with water at pH 10.4, the longer chain amines phase-separated at higher concentrations than the presented ones. Figure 5.1 also shows that the presence of nanoparticles at a concentration of 50 g/L does not alter the interfacial tension. Nonetheless, the foaming properties of these suspensions already strongly differ from the behavior of the pure amine solutions with the same alkyl amine concentration. Surprisingly, the presence of nanoparticle did not have any effect on the interfacial tension.

5.2.2. X-ray Reflectivity

X-ray reflectivity (XRR) was employed to analyze the interfacial composition and morphology. XRR probes the electron density profile along the surface normal (z-direction).

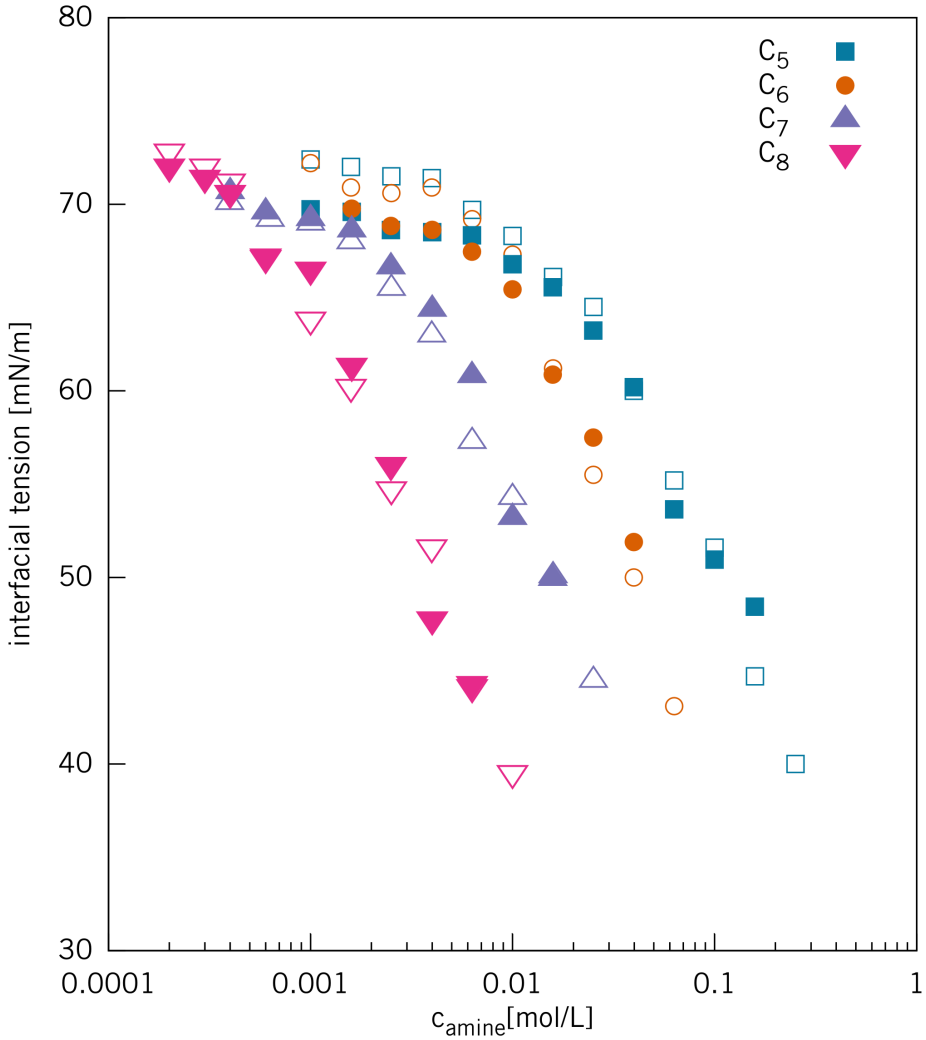

Figure 5.1.: Interfacial tension isotherms of alkyl amine solutions without particles (open symbols) and with a particle concentration of 50 g/L (closed symbols). Adsorption time is about 10 seconds. Error bars are smaller than the sysmbols.

To a first approximation, the reflected intensity $R(q)$ can be calculated from the Fourier transformation of the electron density gradient $d\rho_e/dz$, as described by eq.(5.1).

$$R(q) = R_F(q) \left| \frac{1}{\rho_\infty} \int_{-\infty}^{\infty} \left(\frac{d\rho_e}{dz} \right) e^{iqz} dz \right|^2 \tag{5.1}$$

$R_F(q)$ is the Fresnel reflectivity of the interface between the two continuous phases air and liquid, q is the wave vector and ρ_e is the electron density of the subphase (liquid). It is not possible to invert eq.(5.1) directly since the phase information is lost by the squaring operation. Additionally, the approximation is not accurate in the low q-regime. It cannot describe effects like the total reflection of the x-ray beam below the critical angle q_{crit}. The detailed theory of XRR will not be further elaborated at this point and continuative introductions can be found in literature.

The reflectivity of a certain interface electron density profile can be calculated by matrix methods. Among others, Parratt and Motofit are software packages to perform the calculations. In order to do so, the interfacial electron density profile has to be divided into discrete layers. In the present study, 200 layers were used. Each layer is defined by its electron density and thickness. The electron densities of the components used here are well known or can be calculated straightforwardly. A sketch of an interfacially adsorbed nanoparticle is shown in Fig. 5.2.

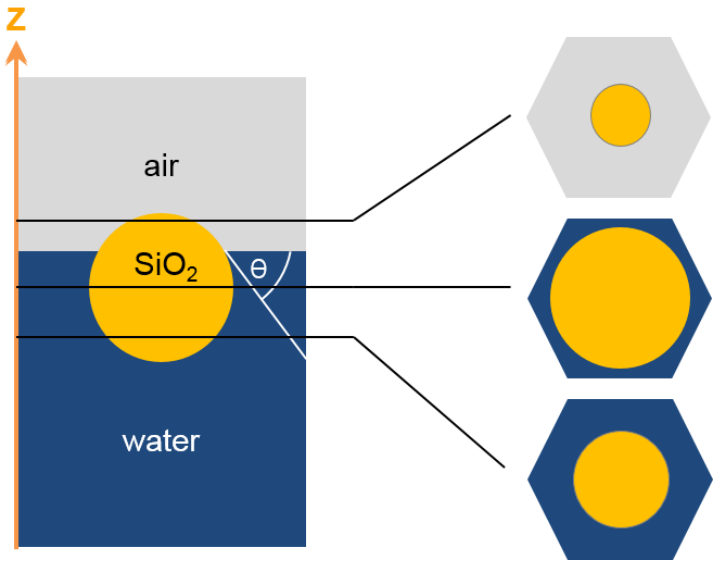

Figure 5.2.: Left: side view of an interfacially adsorbed nanoparticle with contact angle θ. Right: top view of virtual slices through the system in a plane parallel to the interface.

For the calculations, the lateral structure of the adsorbed particles is not important. The interface can be simplified as hexagonal tiles like the one depicted in Fig. 5.2. This

permits to calculate the fraction of particles and surrounding medium at each height z normal to the interface. The system is parametrized by the particle radius, the particle contact angle and the surface coverage of particles.

Another interesting aspect is the slightly polydisperse particle size distribution. A distribution of contact angles is taken into account, as is was also found in other nanoparticulate systems. Both distributions are incorporated as Gaussian. The particle size distribution of the used nanoparticles was measured by SAXS and the particle radius was fixed at r=14 ± 1.7 nm in the model. Figure (5.3) shows an example calculation of the electron density profile.

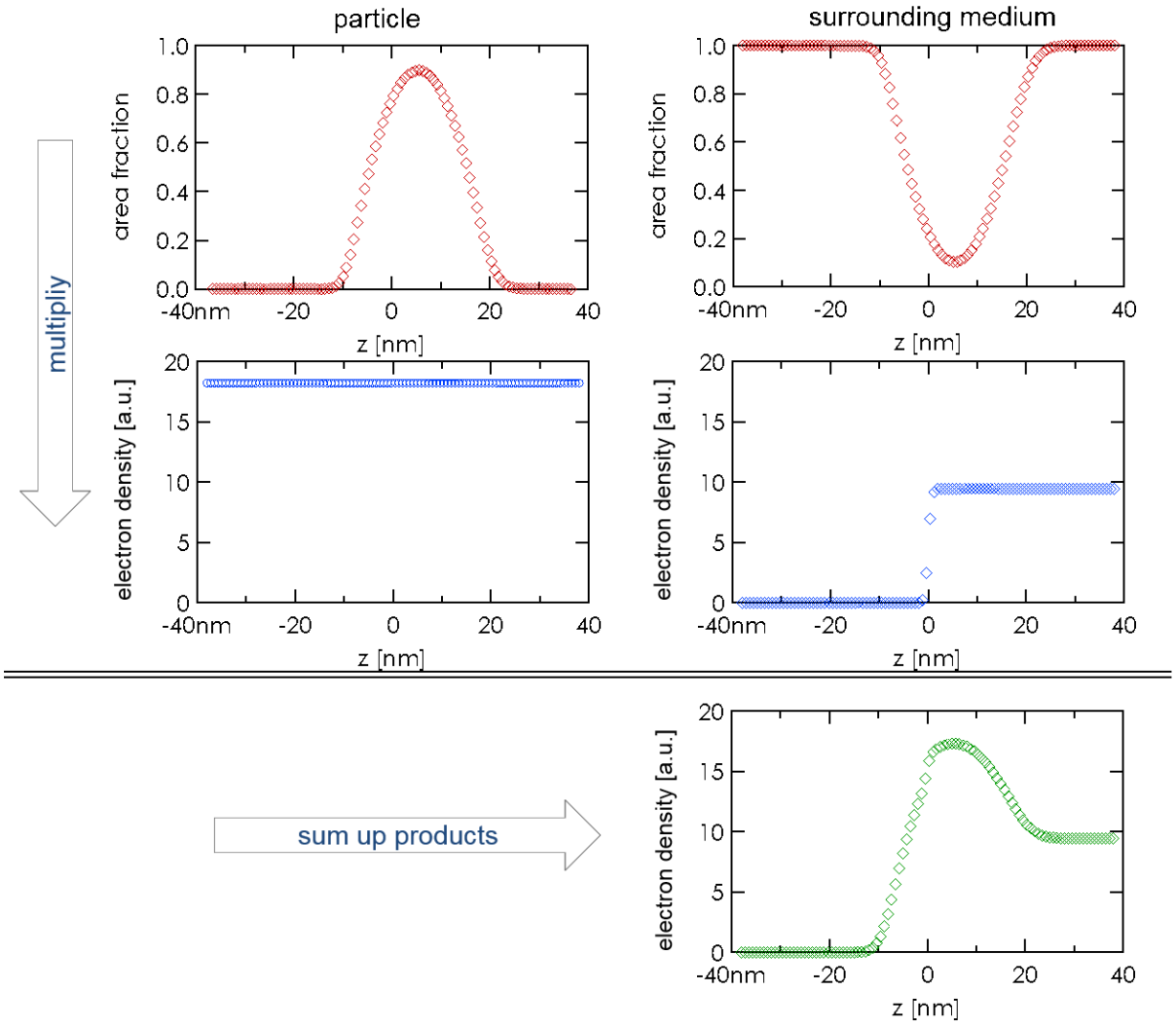

Figure 5.3.: Calculation of the electron density profile. Each data point represents one of the 200 layers. Particle diameter 28±3 nm, contact angle 60±5°

.

The analytical electron density profile has to be discretized into several layers. When a smooth profile is modeled, it is crucial to use a large number of layers. Discretization

artefacts can be avoided by using a layer thickness $t < 0.1 * 2\pi q_{qmax}$. Here, q_{qmax} is the maximum scattering vector in the data that shall be fitted. Too wide layers will produce artefacts in the form of fringes in the calculated reflected intensity curves.

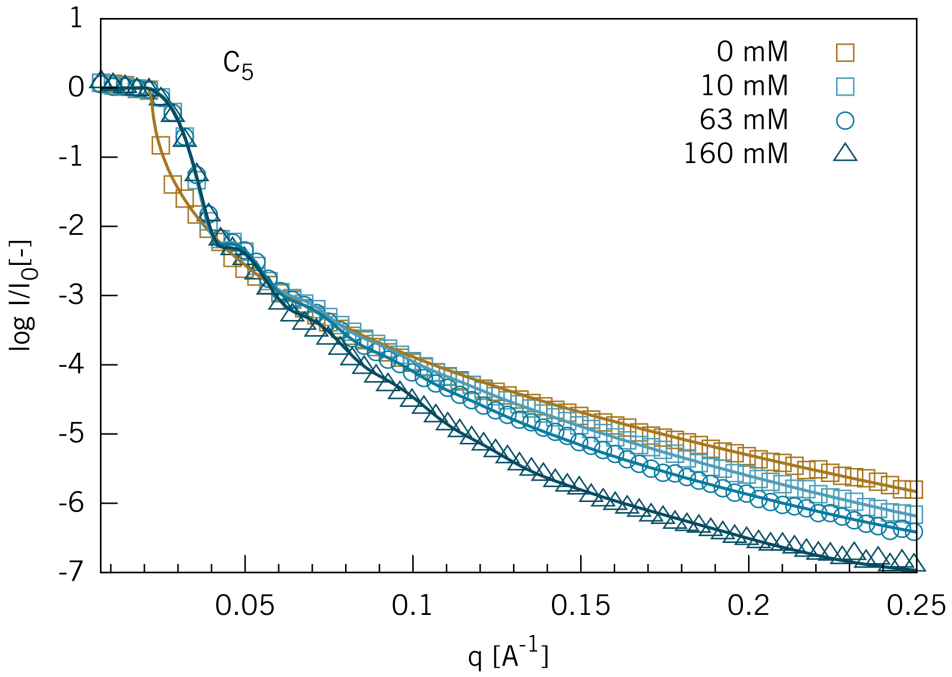

Figure 5.4.: XRR curves of pentyl amine (C_5) modified silica nanoparticles with increasing alkyl amine concentration. Silica concentration 25 g/L.

Figures 5.4 to 5.7 display respresentative XRR curves and corresponding fits for the samples used in this study. Figure 5.4 additionally shows the XRR curve of the bare air/suspension interface without alkyl amines. Evidently, the shapes of the curves are quite similar and do not feature a lot of details. Nonetheless, it should be noted that the total reflection edge is rounded for the amine modified particle suspensions. This is a unique feature and a clear sign of interfacial particle adsorption. For the system without amine modification, the total reflection edge is very well defined, followed by a sharp decay of the reflected intensity.

In the mid-q region between 0.03 and 0.12 A^{-1}, subtle oscillations are observed which are reminiscent of Kiessig fringes. The Δq between two oscillation minima is ≈ 0.02 A^{-1}. According to that, the layer thickness can be estimated from $d = 2\pi/\Delta q$ to be ≈ 30 nm. This thickness is very similar to the diameter of 28 nm of the used particles.

In the high-q region above 0.12 A^{-1}, the decay in reflected intensity is steeper with increasing amine concentration, irrespective of the amine chain length. In addition, the

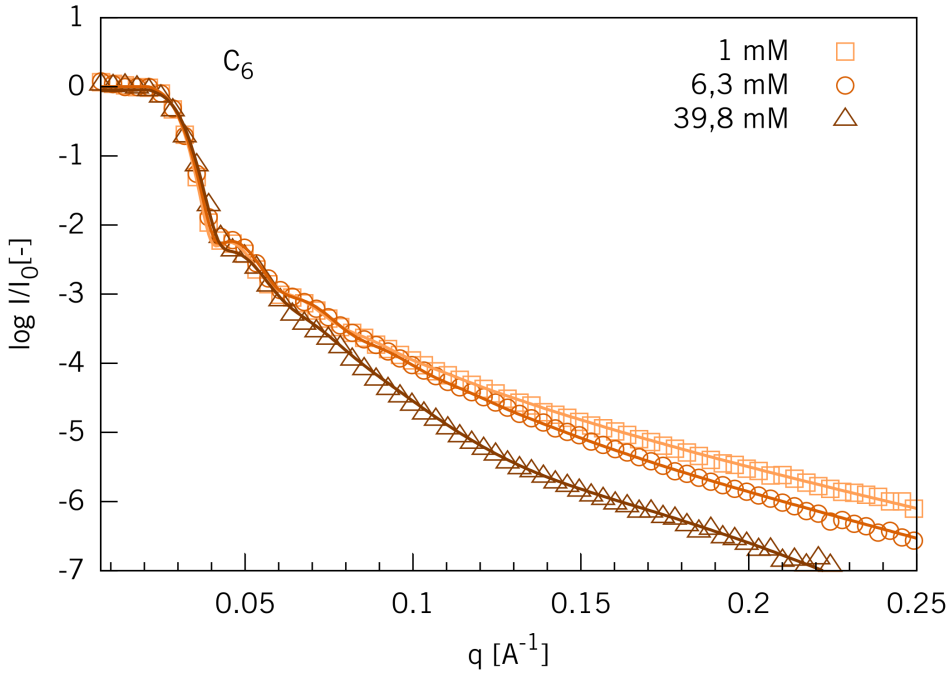

Figure 5.5.: XRR curves of hexyl amine (C_6) modified silica nanoparticles with increasing alkyl amine concentration. Silica concentration 25 g/L.

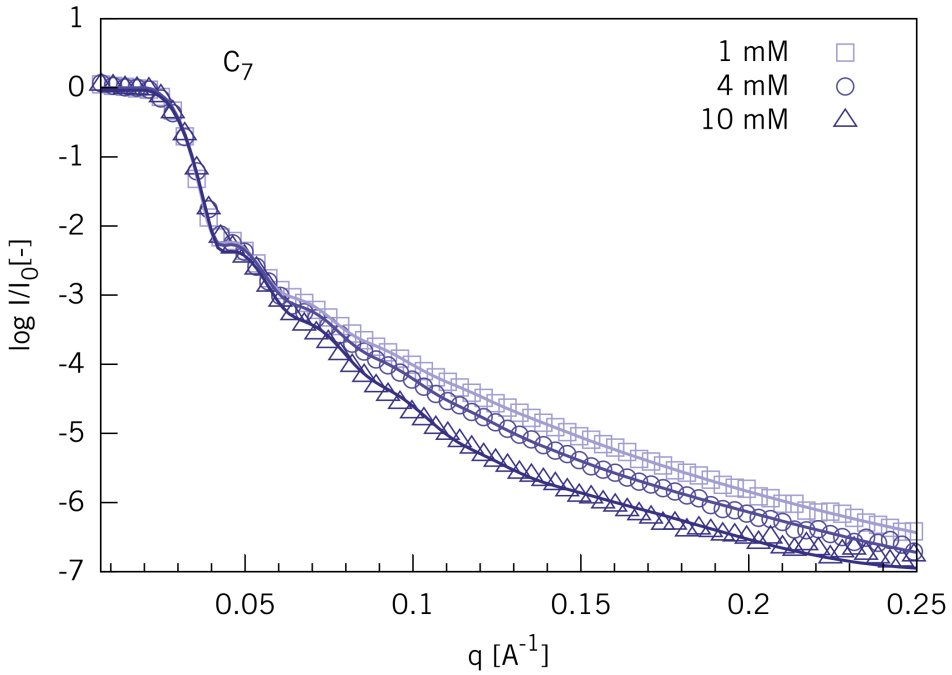

Figure 5.6.: XRR curves of heptyl amine (C_7) modified silica nanoparticles with increasing alkyl amine concentration. Silica concentration 25 g/L.

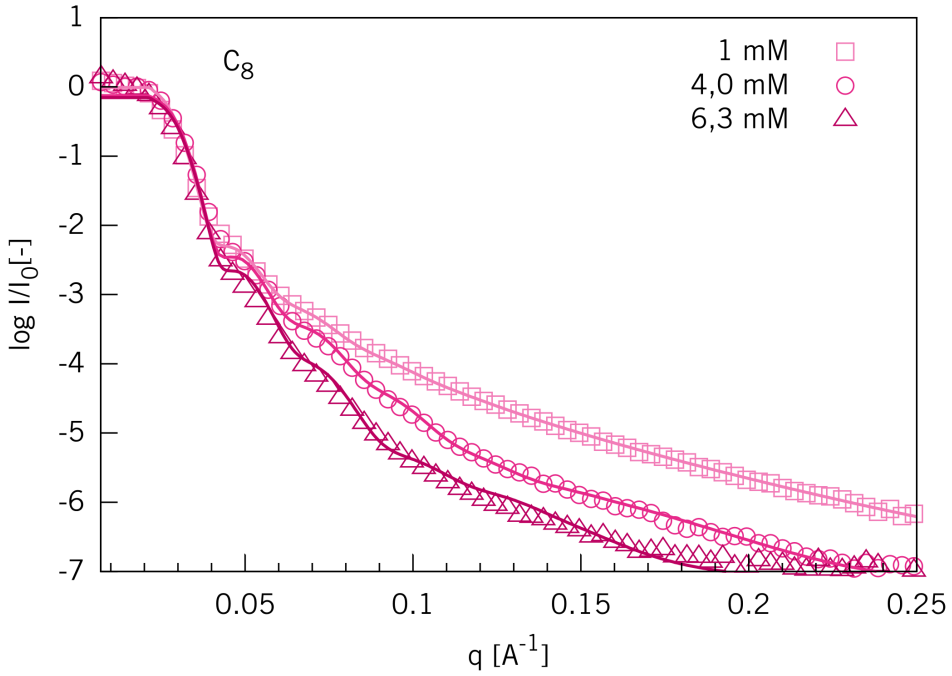

Figure 5.7.: XRR curves of octyl amine (C_8) modified silica nanoparticles with increasing alkyl amine concentration. Silica concentration 25 g/L.

region between 0.08 and 0.22 A^{-1} shows a stronger decay with increasing alkyl amine concentration. The fitting procedure with the model yields the particle contact angle CA, the Gaussian contact angle distribution width σ_{CA} and the mean spacing between the particles s. The resulting particle spacing was ≤ 5 nm for all samples. Variations of the particle spacing from 0 to 5 nm did not lead to noticable changes in the calculated XRR curves. Consequently, the particle fraction at the interface can be assumed to be above 0.80, which is close to a packed layer with a maximum fraction of 0.91.

The contact angle as a function of the amine concentration is shown in Figure 5.8. The corresponding CA distribution widths are listed in Table 5.1. A general trend is observed. The contact angle increases with increasing amine concentration for a fixed alkyl chain length. At comparable amine concentrations, the contact angle increases with amine chain length. Most of the contact angle distribution widths are in the range between 4 and 7°. This is equivalent to a distribution of 10-15 % which corresponds well to other values found in the literature[67,68].

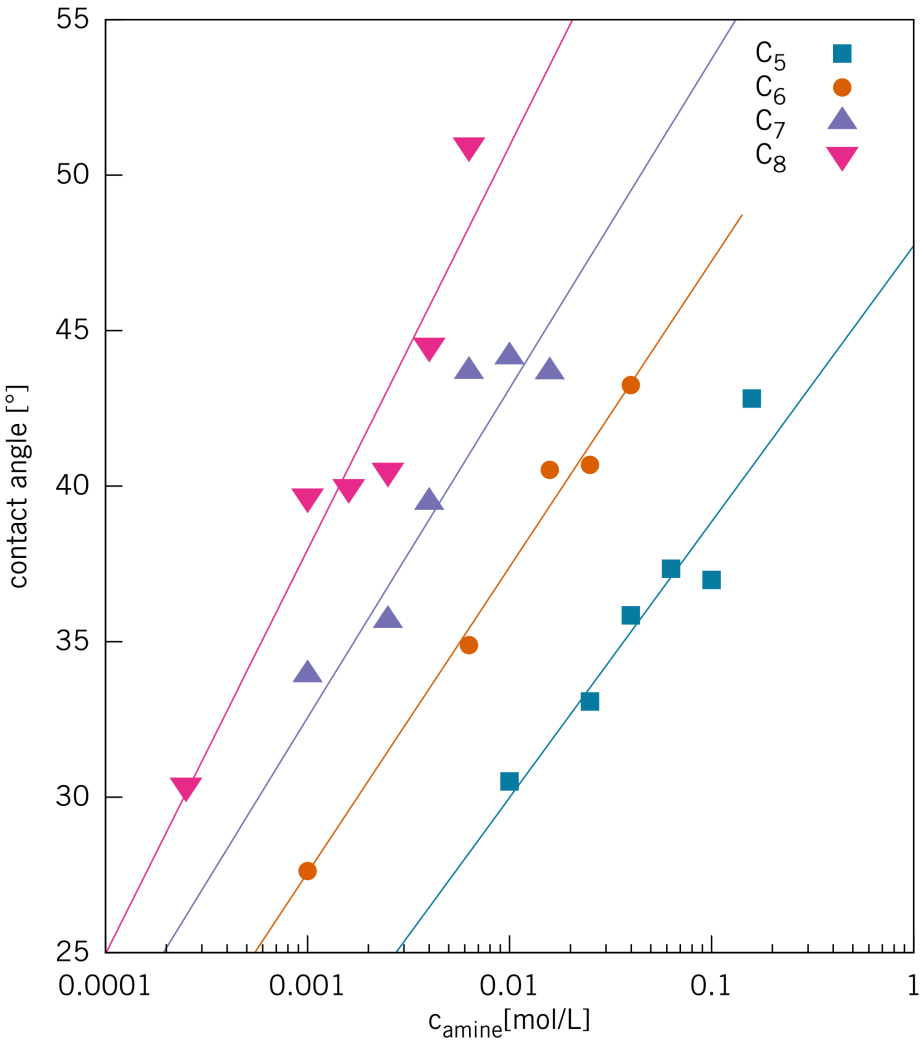

Figure 5.8.: Contact angles as a function of amine concentration determined by XRR according to the model in this chapter. Particle diameter 28 nm, particle concentration 25 g/L. The distribution width is omitted for clarity, it can be found in Table 5.1. Lines are guides to the eye.

Table 5.1.: Contact angles (CA) determined by XRR

$\mathbf{C}_n$	$\mathbf{c}_{amine}$ **[mM]**	**CA [°]**	σ_{CA} [°]
C_5	10,0	31	8
	25,0	33	7
	39,8	36	7
	63,0	37	6
	100,0	37	7
	158,0	43	4
C_6	1,0	28	12
	6,3	35	6
	15,8	41	6
	25,0	41	6
	39,8	43	5
C_7	1,0	34	6
	2,5	36	4
	4,0	39	5
	6,3	44	5
	10,0	44	5
	15,8	44	4
C_8	0,25	30	10
	1,0	40	10
	1,6	40	5
	2,5	40	8
	4,0	45	4
	6,3	51	6

5.2.3. Theoretical Calculations

In order to approach the problem of particle adsorption from a theoretical point of view, the model proposed by Reincke et al. was applied[57]. The model considers different interaction potentials of particles fixed at the interface. The exact formulas for the calculations become rather elaborated and are not shown here in details. For detailed information, the reader is referred to the supporting information of the original publication by Reincke et al[57]. The model was translated into an octave script, which can be found in Appendix A.2. A brief summary of the calculations is given in the following text.

A particle pinned at the interface with a certain contact angle is surrounded by two different media. In the case of the present study, the two media are air and an aqueous suspension. Figure 5.2 illustrates that the top of the particle is located in the gas phase while the bottom part is immersed in the aqueous phase.

In thermodynamic equilibrium, the chemical potentials of a particle at the interface μ_{int} and a particle in the liquid μ_{bulk} are identical, expressed by:

$$\mu_{int} = \mu_{bulk} \tag{5.2}$$

The term μ_{int} is composed of

- $\mu_{unscreened}$, the unscreened Coulomb interaction through the gas phase in case of free charges left on the top part of the nanoparticle.
- $\mu_{screened}$, a Coulomb interaction acting through the water phase.
- μ_{dipole}, a dipolar interaction resulting from the unequal amounts of free charges on the particle top and bottom.
- μ_{vdW}, the van der Waals term assuming 6 neighbor particles.

In order to solve the above equation for the equilibrium surface fraction y, some assumptions on the parameters had to be made. These were as follows. The particle radius is 14 nm, the contact angle is 40° which is a good estimate considering the results from the XRR experiments. The volume fraction of particles is taken as 0.0125 which corresponds to the value used in the XRR measurements. The relative dielectric constant of the gas and water phase are 1 and 78, respectively. The interfacial tension is 50 mN/m which is a mean value taken from the interfacial tension measurements. The ionic strength is 50 mM, mainly from methyl ammonium and chloride ions. The Hamaker constant is

$1 \cdot 10^{-20} J$. For theoretical considerations, a residual surface charge density is allowed to stay on the top of the particle, in the gas phase. This residual surface charge density is taken as a fraction of the charge density of the particle surface in the aqueous phase.

In the calculations, Eq.(5.2) is numerically solved for the adsorbed particle fraction y. The fraction is calculated for different surface charge densities. Additionally, the residual charge in the gas phase is varied. Figure 5.9 shows the calculated equilibrium surface fraction as a function of the surface charge density of the particles.

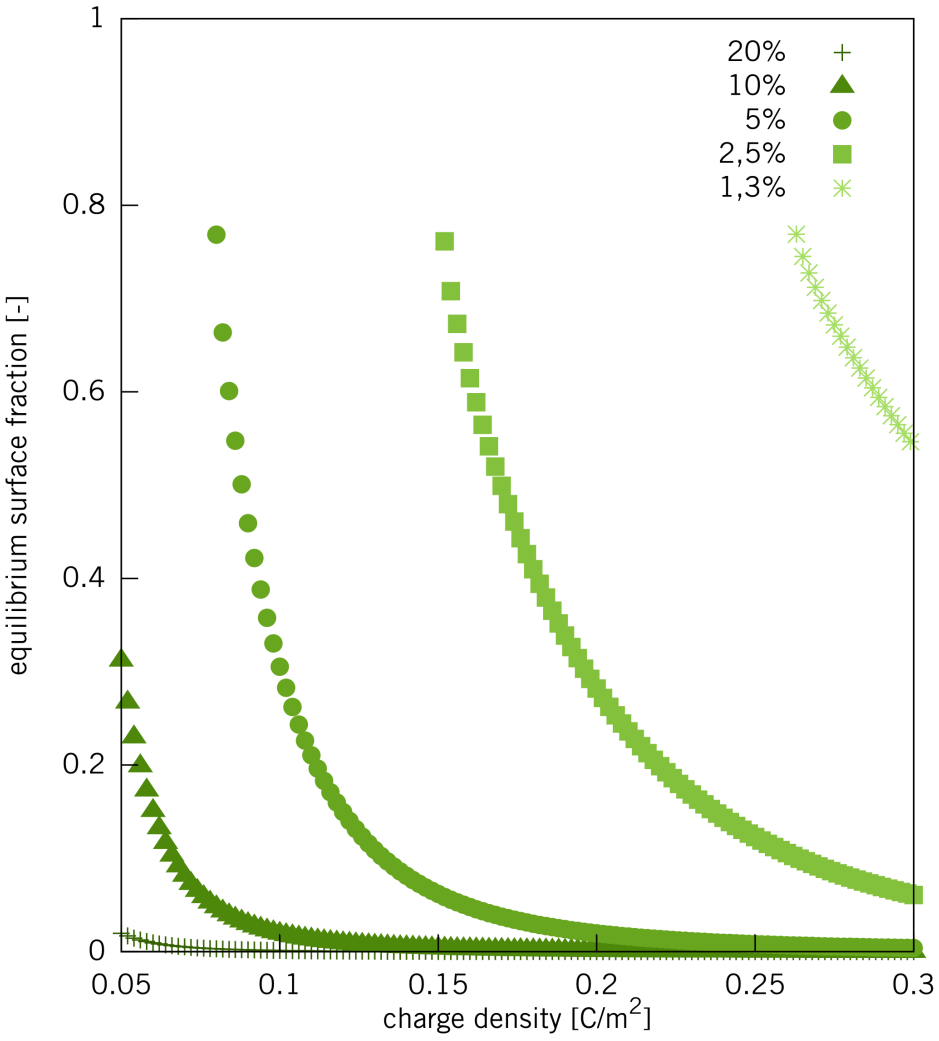

Figure 5.9.: Calculated equilibrium surface fraction of the particle layer as a function of the surface charge density and the residual surface charge fraction in the low-ϵ_r phase (in percent). The volume fraction of the particles in the bulk phase is 0.0125.

The equlibrium fraction increases as the surface charge decreases. At low surface charges, the calculation becomes numerically unstable and no equilibrium can be found. This is the case when it is energetically more favorable for the particle to adsorb at the interface

than being immersed in the solvent. From the point of thermodynamics, the interface becomes fully packed with particles for surface charges at the left end of each curve.

Another observation is that increasing residual surface charges in the gas phase lead to lower equilibrium fractions. This can be accounted to the strong unscreened Coulomb interaction through the gas phase. Nevertheless, this kind of interaction is highly speculative.

5.3. Discussion

The interfacial tension isotherms for the pure amine solutions and the particle suspensions were nearly identical. From these measurements, particle presence at the interface cannot be concluded.

Direct evidence of particles at the interface was found by using XRR. Here, an acceptable fit result could be obtained for all reflectivity curves shown above. These measurements permitted to obtain values of the particle contact angles. It can be concluded that the in-situ adsorption of alkyl amines onto the silica nanoparticles induces a slight hydrophobicity. The particles are rendered surface active and adsorb to the air/suspension interface. From the reflectivity experiment in specular condition, solely information along the direction normal to the interface is obtained. However, it is possible to gain information about the amount of particles at the interface, while it is not possible to deduce information about the lateral structure of the particle layer.

The rounded total reflection edge in the reflectivity curves can be found when the electron density along the z-direction is not step-like. In the case of adsorbed spherical particles, there is a smooth gradient in electron density as displayed in Figure 5.3. The position of the total reflection edge depends on the electron density contrast between the different layers. The rounding might be interpreted as an overlay of many sharp reflection edges slightly shifted to each other. Simulations with the fitting model have shown that the decay or curvature in the mid-q region becomes more pronounced with contact angles increasing from 0 to 90°. This predicted behavior is found for increased amine concentrations. Increasing the contact angle further from 90 to 180° will lead to the formation of a sharp total reflection edge, which was not found here.

Knowledge of the particle contact angle permits to calculate the detachment energies E_{det}, which is nescessary to remove a particle from the interface. For a homogeneous, spherical

particle, the detachment energy can be calculated according to Pieranksi and Binks:

$$E_{det} = \pi R^2 \gamma \left(1 - cos(\theta)\right)^2 \tag{5.3}$$

with the particle radius R, the interfacial tension γ and the contact angle θ. In this form, the equation describes the removal of the particle into the water phase, which is the only relevant direction for a gas/liquid interface. It is convenient to express the detachment energy in units of the thermal energy kT for a temperature of T = 300 K. For an interfacial tension of 50 mN/m, a particle radius of 14 nm and a contact angle of 40°, the energy E_{det} is 410 kT. Decreasing the contact angle to 30° still yields 134 kT. It should be kept in mind that the simple geometrical model does not include any lateral particle-particle interaction.

Additionally, it is assumed that the alkyl amines distribute homogeneously on the particle surface. Figure 5.10 presents a sketch to illustrate the model.

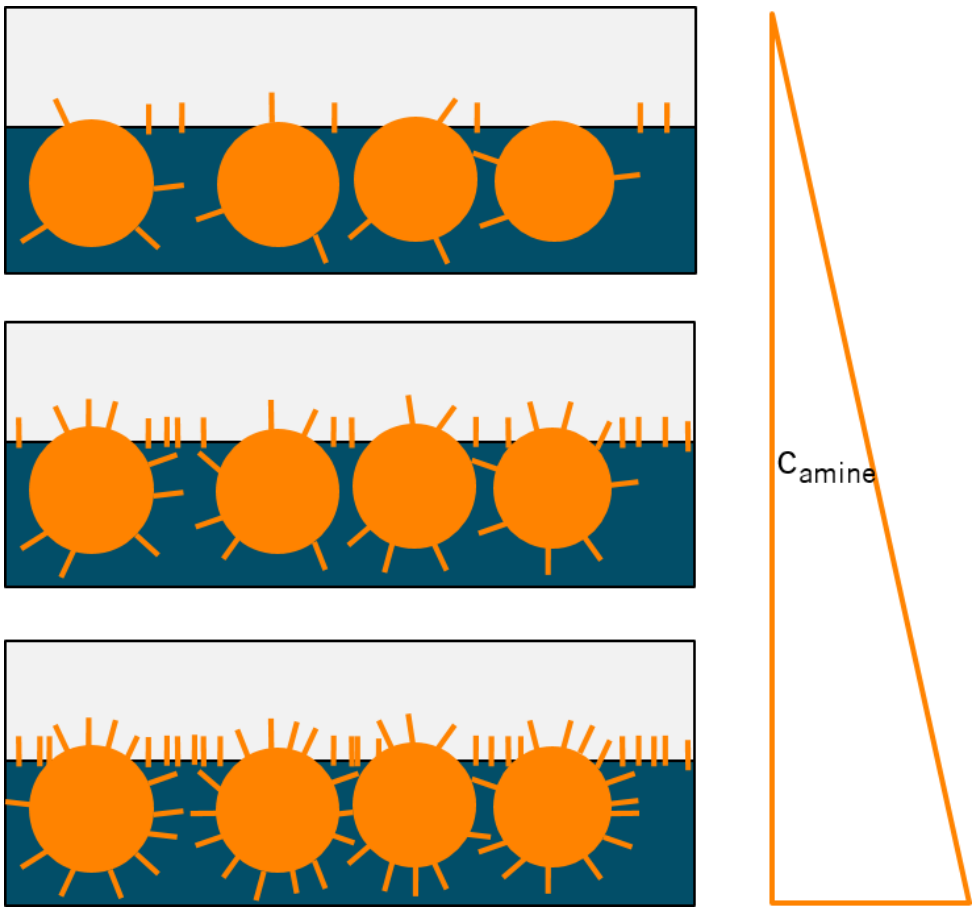

Figure 5.10.: Side-view of the assumed distribution of amine on the particle surface and the air/water interface as the amine concentration is increased.

Following these assumptions, the particles are irreversibly attached to the interface. The energy required to remove them is two orders of magnitude higher than the thermal energy. There are few studies on contact angle distributions of sub-micron particles. Gaussian distributions of contact angles have been found for latex particles of different sizes. Though the particles are pinned at the interface, they can still slightly change their position in z. Hence, the distribution of the contact angle would be due to particle dynamics.

The samples were studied after an equilibration time of 1 h in order to prevent changes in the system during the measurement. It is fair to assume that this time is sufficient for a quasi-equilibrium adsorption state of the particles. To apply the Reincke model, the surface charge density of the particles has to be known. The charge density of silica varies with the pH and varies in the literature. Some rough estimations on the lower and upper values of the surface charge can be made. A low charge density of $1e^-/5nm^2$, corresponds to 0.03 C/m^2, this can be taken as the lower limit. Assuming the surface is charged to the point where the mean distance between two charges is equal to the Bjerrum length, the charge density would be ≈ 0.3 C/m^2. From the ζ-potential, a rough estimation applying the Grahame equation yields a surface charge density on the order of ≈ 0.05 C/m^2. Figure 5.9 shows a considerable amount of surface charge on the particle top (in air) is needed to prevent a maximum surface coverage. It is highly unlikely that free charges exist on the particle in the gaseous phase. There is no screening of the electrostatic interaction in the gas phase to keep counterions seperated. Consequently, a high packing density should be achieved even for high surface charge densities > 0.25 C/m^2.

With respect to the behavior of the particles in a foam lamella, the contact angle is not supposed to depend on the equilibration time. In a foam, the liquid reservoir is very small compared to the gas/liquid interfacial area. Thus, it might be thermodynamically favorable to form a packed particle layer, but the ageing of the foam is too fast to establish an equilibrium adsorption state. In Figure 5.11, two possible adsorption schemes in a foam lamella are shown. Either the particles for a layer on each interface or the particles can bridge between the interfaces. Bridging is only possible for particles with contact angles below 90°. Particles with contact angles larger than 90° are supposed to act as defoamers because they pinch off the lamella.

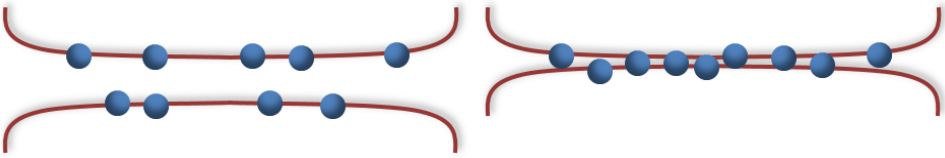

Figure 5.11.: Different possible states of a foam lamella. Left: Particle layer on both gas/liquid interfaces. Right: Bridging particles

5.4. Conclusion

The adsorption behavior of the alkyl amines and the amine-modified silica nanparticles onto the gas/liquid interface was investigated.

It is shown that the amines behave like short chain surfactants. The presence of particles adsorbed at the interface could not be clearly deduced from interfacial tension measurements. X-ray reflectivity clearly proves the existence of an interfacially adsorbed particle layer. However, the lateral structure could not be resolved by this method. Combined theoretical calculations and experimental results lead to the conclusion that the equilibrium particle fraction for long waiting times is close to that of a packed layer at the interface.

A model was developed to determine the particle contact angle via XRR. Excellent fitting results could be obtained from the experimental data. The contact angle of $\leq 50°$ indicates a moderate hydrophobicity of the nanoparticles. Slight distribution of the contact angles of around 10% is found. This low hydrophobicty is sufficient to make the interfacial attachment of the particles irreversible.

The experimental results show that the interfacial structure on a foam bubble likely differs from the equilibrium structure. This is compatible with the results in Chapter 6 from which an interfacial network was concluded for low adsorption times.

The possibility to measure the particle contact angle is important for studies of particle adsorption in general, since it allows to understand the themodynamics of the system. Further studies to investigate the bubble interface in a macroscopic foam are of interest.

Chapter 6.

Bulk Behavior and Interfacial Structure*

Abstract

In this chapter, a multi scale approach is used to reveal how the microscopic properties of the nanoparticle dispersion are translated into their foaming behavior at the macroscopic scale. Fluorescence spectroscopy and electrophoretic mobility measurements are used to characterize the bulk behavior of the nanoparticles with adsorbed amines. The interfacial behavior is probed by compressing particle monolayers while monitoring the surface tension. The macroscopic foamability and foam stability are evaluated. There are strong correlations between the system properties at all length scales. The most prominent effects are observed at a critical bulk concentration of amines at which the nanoparticles start to aggregate due to hydrophobic interactions. The study shows how the foam properties are related to the features of the bulk dispersions and to the ordering of particles at the air/water interface.

Design of experiments, data analysis and evaluation were done by the author. Measurements of the electrophoretic mobility, 50 % of the fluorescence experiments and 60 % of the droplet compression experiments were performed by Anne Bannuscher.

6.1. Introduction

Aqueous particle stabilized foams are applied in a variety of industrial processes. In the food industry, protein aggregates are used to stabilize foams and emulsions. Waste water is cleared by removing hydrophobic contaminations that attach to air bubbles. Valuable ores are selectively extracted from less valuable material in the process of froth flotation[56,72,73]. It was shown that particle rich foams can be precursors to the fabrication of porous ceramics and porous metals[55,74]. These processes have in common that particles are mimicking the role of surfactants by stabilizing fluid/fluid interfaces and the particles have to be sufficiently hydrophobic. The size of the particles of interest is usually in the order of nanometers to microns.

Some particles, e.g. milk proteins, possess inherent hydrophobicity and readily attach to the air/water interface without the need of modifying the proteins. Other particles,

*Similar content was presented in A. Carl, A. Bannuscher, and R. von Klitzing, *Langmuir*, **2015**, *31*, 1615-1622.

like silica, are very hydrophilic and therefore do not attach to the interface in their natural form. In order to render silica particles hydrophobic, they can be reacted with hydrophobic silanes that attach covalently to the hydroxyl groups present at the particle surface[2,75]. It has been shown that fumed silica particles with an appropriate degree of covalent hydrophobization act as highly efficient foam stabilizers[14,34,76,77]. Without any additional surfactants, foams with life-times of weeks or longer have been achieved by this route. These life-times greatly surpass those of regular surfactant foams. Another way to hydrophobize the particles is to physically adsorb hydrophobic molecules to the particle surface. As with particle-only systems, improved foam stability was found at appropriate surfactant concentrations. In general, when particles and suitable surfactants are combined, synergistic effects can be found in terms of foamability and/or foam stability of the corresponding dispersions[43,74,78]. Hunter and Horozov reviewed the different concepts of foam stabilization with emphasis on foam stabilization mechanisms involving (nano)particles[79,80].

It has been found that particle layers can stabilize a fluid/fluid interface by forming a protective layer around the dispersed phase. These layers can decellerate or even halt Ostwald ripening and coalescence processes[77,81–85]. For the case of foams, particles at the interface and within the foam lamella keep the bubbles separated, providing additional steric stabilization. Drainage is decelerated when the bubble surfaces become stiffer[17,18]. Gas exchange between bubbles will favor the formation of large bubbles at the expense of smaller ones, a process reminiscent of Ostwald ripening. The thicker the lamellae between to foam bubbles, the slower the gas exchange. Besides, a thicker foam lamella is less likely to rupture and to coalesce two adjacent bubbles.

Hydrophobic nanoparticles can have very high interfacial adsorption energies. For sufficiently large and hydrophobic nanoparticles (e.g. $R > 10$ nm, contact angle $> 45°$), the adsorption energy can become orders of magnitude larger than the thermal energy. This means the particle adsorption is essentially irreversible[4] in those cases. Regarding the lateral interaction of the particles, once they are at the interface, several approaches were used to clarify the lateral structure of the adsorbed layer[8,57]. Oettel et al. discussed the interfacial behavior of micron sized particles[86]. For nanoparticles, predictions remain challenging. Groot et al. simulated the adsorption of hydrophobic particles to the air/water interface and postulated the formation of a 2D fractal network of particles at the interface[87].

The structure of the adsorbed nanoparticle layers is not fully understood. Stocco found in an x-ray tomography study that it is not necessary to have a fully particle covered bubble interface in order to achieve high foam stability. In general, it was found that the

formation of bulk aggregates strongly enhances the foam stability due to bulk gelation. In combination with a high particle fraction, even drainage can be suppressed[88]. Despite the similarities found for different systems composed of particles and surfactants, it remains challenging to predict properties like foamability or foam stability.

In the present study, mixtures of commercial silica particles (Ludox TMA) and alkyl amines of different chain lengths (C_5 to C_8) are investigated. Pure aqueous solutions of short chain alkyl amines do not form stable foams. Similarly, the nanoparticle dispersions show essentially no foamability since the silica particles are very hydrophilic and therefore not surface active. Combined dispersions of silica and alkyl amines show a broad spectrum of foaming behavior and strong evidence for synergistic effects.

The bulk properties of the particle-amine systems are characterized by measurements of the elecrophoretic mobility and fluorescence spectroscopy to examine the adsorption behavior of the amines onto the silica nanoparticles. Surface pressure isotherms are recorded to obtain information on the interfacial structure of the particle layers. The macroscopic foaming behavior is investigated by image analysis.

Usually, it is very hard to predict the foamability or foam stability even for pure surfactant systems. It is shown that there is a strong correlation between characteristic properties ranging across all investigated length scales that permit to predict foamability and foam stability of the dispersions.

6.2. Results

6.2.1. Bulk Behavior

Different length scales, from the nanometer scale to the centimeter scale, were assessed in this study. To follow the adsorption of the alkyl amines onto the silica particles' surface in the bulk, the electrophoretic mobility of the dispersions was measured at different amine concentrations. Figure 6.1 shows the electrophoretic mobilities and corresponding zeta-potentials of the silica particles as a function of the alkyl amine concentration for different carbon chain lengths. Bare particles in methyl amine buffer have a zeta potential of around -35 mV. The particle surface charge is partially neutralized as the amine concentration is increased. For every additional CH_2-group added to the carbon chain, this neutralization starts at lower alkyl amine concentrations. Hexylamine (C_6) shows a charge reversal of the particles in the concentration range studied. The particles start to flocculate in

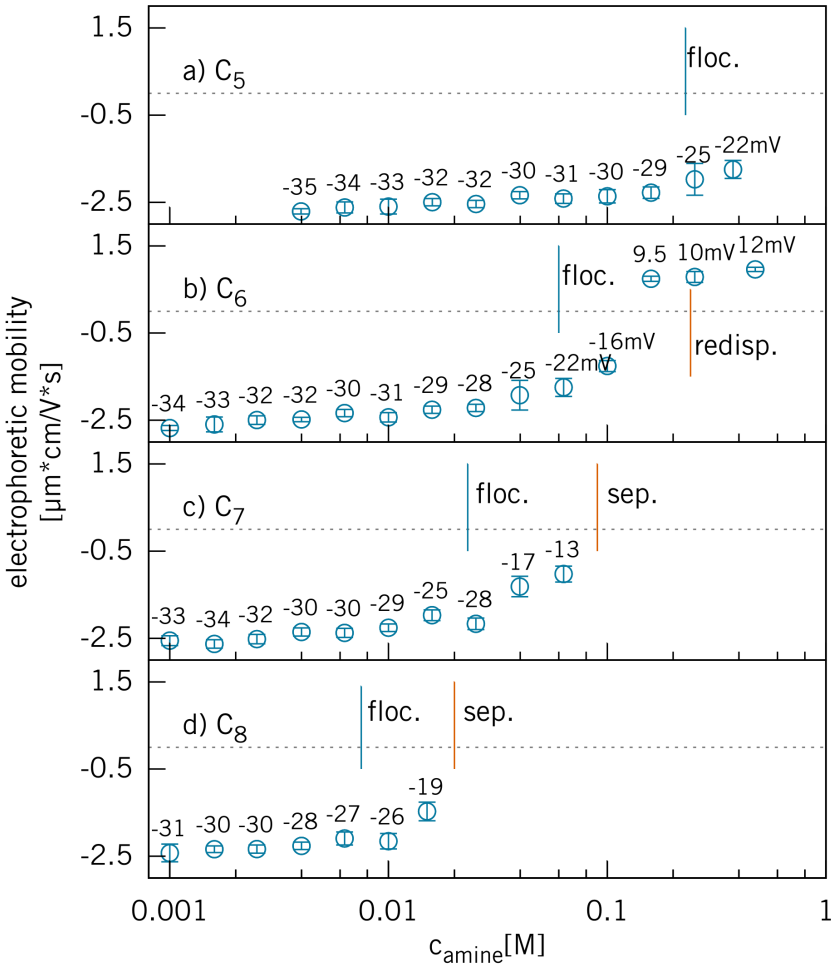

Figure 6.1.: Electrophoretic mobilitiy and ζ-potential (in mV) dependence on alkyl amine chain length and concentration for a dispersion of 2.5wt-% silica particles. Adsorption of the amines to the particles leads to charge neutralisation at the particle/water interface. Bulk flocculation at a certain amine concentration is indicated by "floc". Redispersion of the particles is marked by "redisp". Separation into a water-rich and amine-rich phase is indicated by "sep".

bulk around a zeta-potential of -25 mV. Heptylamine (C_7) and octylamine (C_8) phase seperate into a water and amine phase above a concentration of 0.09 mol/L and 0.02 mol/L, respectively.

The question arises, what drives the flocculation process. For classical long-chain surfactants the effect of surface charge reduction and charge reversal due to surfactant adsorption is well known. It can be explained by surface micellization and the consecutive formation of a surfactant double layer at increased surfactant concentrations[89,90].

In order to investigate whether cooperative phenomena can be found for the short-chain systems, pyrene was used as a fluorescent probe. The ratio of the intensity of the first (I_1) and third (I_3) prominent band in the fluorescence spectrum changes, depending on the hydrophilicity of the surrounding medium. Residing in a hydrophilic environment, the ratio I_1/I_3 is in the range of 1.8, while for a hydrophobic environment the ratio reduces to 1.1-1.2. The fluorescence spectra for pyrene in water and pyrene in a cetyltrimethylammonium bromide (C_{16}TAB) solution above the CMC of C_{16}TAB are depicted in the inset of Figure 6.2. Because of its high partitioning coefficient $pK_{ow} = 5.2$, pyrene readily partitions into any available hydrophobic domain of appropriate size to accomodate the molecule. Figure 6.2 shows, for the pure pentylamine (C_5) solution, no hydrophobic domains can be found since the ratio I_1/I_3 is ≈ 1.8 for the full concentration range studied. For the mixed system of pentylamine and particles, at a pentylamine concentration of 0.23 mol/L, the intensity ratio decays to 1.2, indicating the presence of hydrophobic moieties. In the case of a pure hexylamine (C_6) solution, a change of I_1/I_3 from 1.8 to 1.1 is found at a concentration of 0.24 mol/L. When silica particles are present, this change in the pyrene fluorescence behavior is observed at a lower concentration of 0.06 mol/L. Increasing the chain length further to heptylamine (C_7) and octylamine (C_8), no hydrophobic domains can be detected for the pure amine solutions until they phase seperate into a water and amine phase. In the presence of particles, a reduction in the I_1/I_3 intensity ratio can be seen at an amine concentration of 0.02 mol/L for heptylamine and at 0.008 mol/L for octylamine.

6.2.2. Interfacial Behavior

In order to gain insight into the interfacial properties of the silica/alkyl amine dispersions, surface pressure isotherms were recorded. Silica particles spontaneously adsorb to the air/water interface if sufficiently hydrophobized by the alkyl amines. The prepared Gibbs monolayers of total interfacial area A_0 were compressed under controlled conditions.

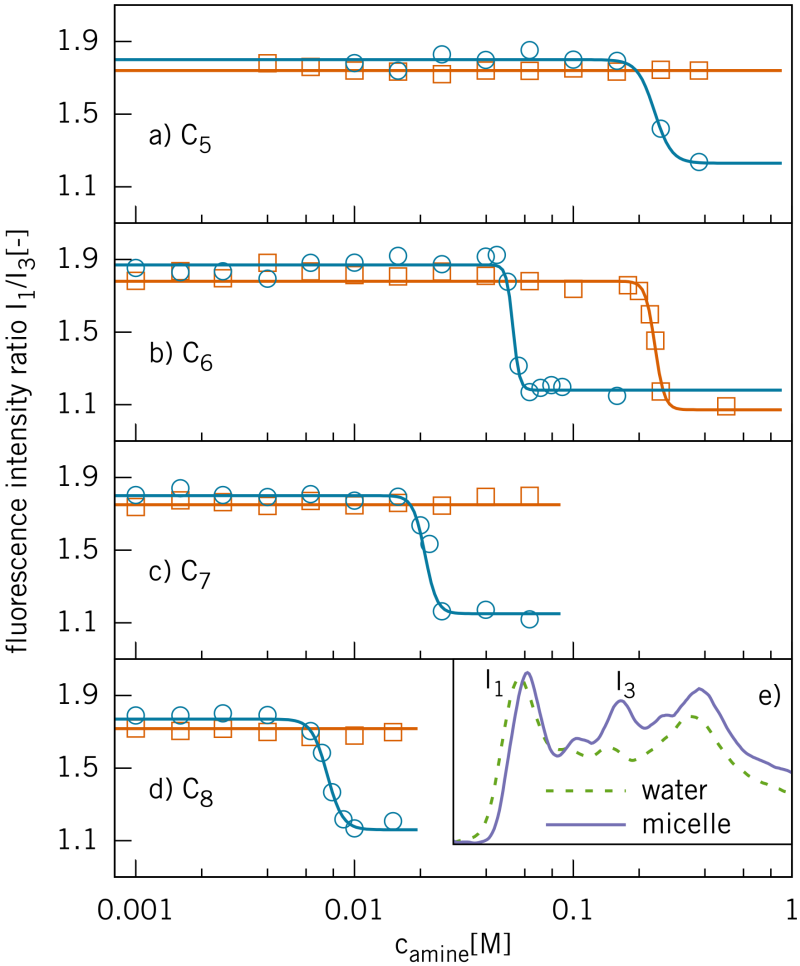

Figure 6.2.: Probing of hydrophobic domains by fluorescence spectroscopy. Ratio of the fluorescence intensities I_1 and I_3 of the pyrene molecule as marked in the inset in the lower right. Ratio for the pure amine solutions at increasing concentrations (squares) and the mixed dispersions with an amount of 2.5wt-% silica particles (circles) for the studied chain lengths. A change of the ratio I_1/I_3 from 1.8 to 1.2 indicates the formation of hydrophobic domains. For heptylamine c) and octylamine d), phase separation occurs above the concentrations shown. Solid lines are guides to the eye.

Surface pressure isotherms permit to probe the two-dimensional particle-particle interaction at the air/suspension interface. When a hydrophobic nanoparticle attaches to an interface, from interfacial tension balance arguments it can be followed that the attachment energy E for a homogeneously coated nanoparticle is[75]

$$E = \pi r^2 \gamma_0 \left(1 - cos\theta\right)^2 \tag{6.1}$$

with the particle radius r, the contact angle θ and the air/dispersion interfacial tension γ_0. For the particles used in this study and even low contact angles of $\theta > 30°$ the adsorption energy of the particle exceeds the thermal energy kT by orders of magnitude, $E >> 100kT$. That is, the particles attach irreversibly to the interface. The interface is not necessarily fully covered with particles but may show a fluid-like behavior. When such an insoluble particle layer is compressed, a surface pressure builds up due to the particle-particle interaction. The surface pressure Π can be monitored during the compression by monitoring the surface tension and is calculated by $\Pi = \gamma_0 - \gamma$ with γ_0 as the corresponding alkyl amine solution surface tension without particles[8].

The pendant drop technique was used to follow the change in surface tension during compression. In comparison with the classical experiment in a Langmuir trough, this technique has been shown to be less susceptible to surface impurities and has high reproducibility[91]. The droplet surfaces are compressed isotropically. Especially for particle layers, it has been found that anisotropic compression may induce unwanted structuring at the interface. In this study, the ratio $R_{drop}/R_{particle} > 10^5$, so the interface appears flat to a single particle. Figure 6.3 demonstrates the good reproducibility of the experiment. It should be noted that the data are scaled logarithmically. In a control experiment, neither the pure alkyl amine solutions nor the particle dispersion show any significant surface pressure up to a compression of $A/A_0 \approx 0.15$. Further compression leads to artefacts in the analysis since the droplets becomes too spherical for the reliable application of the fitting algorithm.

An insoluble particle layer can not be compressed indefinitely since at some point, the particles form a packed layer at the droplet interface, the corresponding area is called the collapse area. In Figure 6.3, the collapse can be identified as a kink in the surface pressure curves for the higher amine concentration towards low values of A/A_0. Further forced compression of the droplet can result in surface crumpling and a non-Laplacian shape of the droplet[10,12].

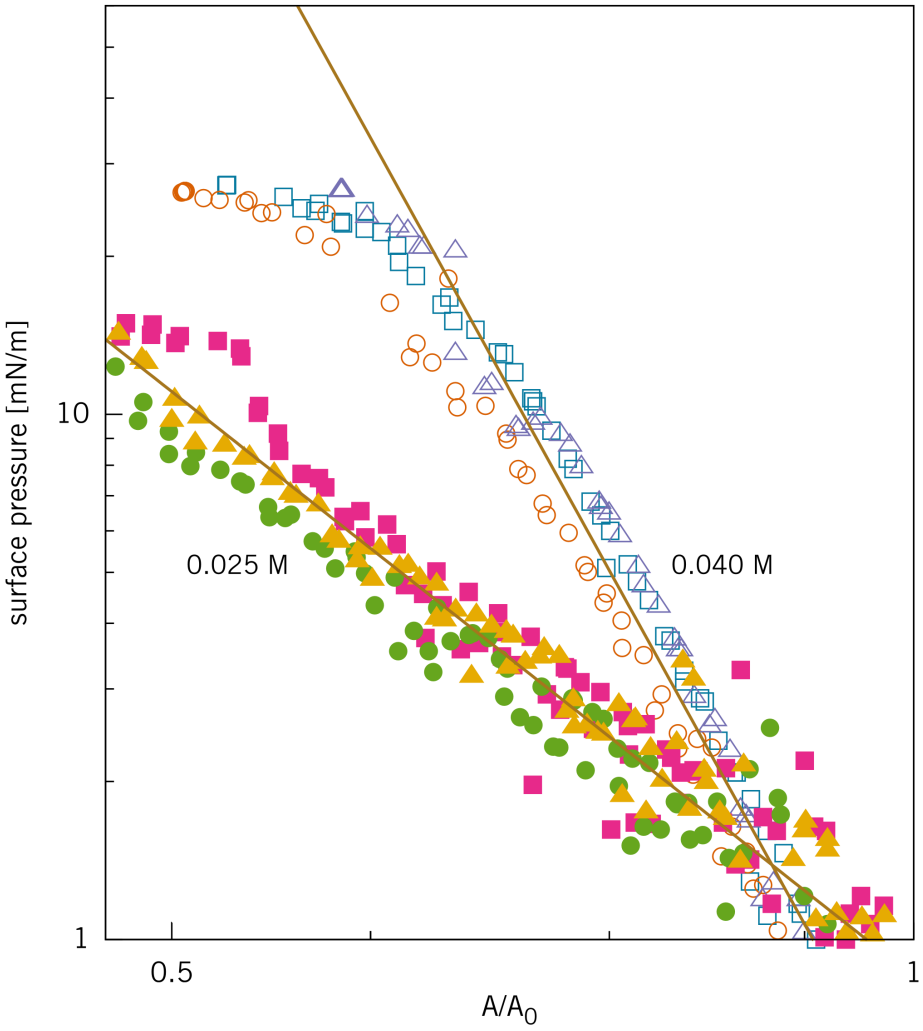

Figure 6.3.: Surface pressure isotherm analysis from pendant drop measurements. Hexylamine modified silica particles were compressed at the amine concentration stated at the corresponding plots. Closed and open symbols correspond to repeated measurements of the surface pressure isotherm at the same hexylamine concentration. Power laws were fit to the data.

Additional to the collapse point, Figure 6.3 shows, that the surface pressure scales differently for different amine concentrations at the same carbon chain length. In the log-log presentation, it can easily be seen that the surface pressure Π scales as power law of the form $(A/A_0)^E$. Figure 6.4 shows that with increasing alkyl amine concentration, the col-

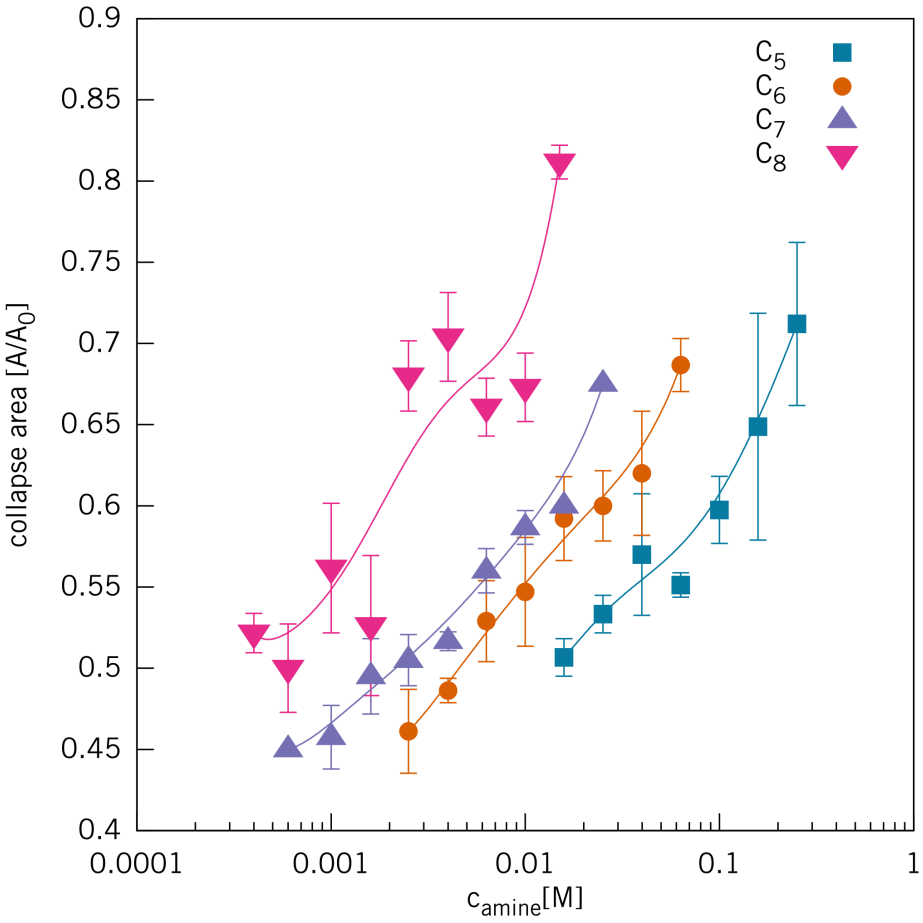

Figure 6.4.: Collapse area fraction at which either the surface pressure remains constant or the drop shape become non-Laplacian. An increasing collapse area A/A_0 indicates a higher particle coverage at the interface. The adsorption time for all samples was 90 s. Solid lines are guides to the eye.

lapse area fraction increases, irrespective of the carbon chain length. Put another way, the amount of adsorbed silica particles increases with increasing alkyl amine modification and chain-length, so a compression leads to a close packed layer earlier during the compression.

Microscopy performed on a single foam lamella (Figure 6.5) reveals that the particles structure at the interface to form areas of varying particle coverage. The brightness at a certain point in the image is proportional to the film thickness at that spot. From the

image, it is unlikely that the observed aggregates are spherical, since such large aggregates would most likely lead to rupture of the foam lamella. Additionally, the aggregates appear to have a homogeneous brightness which suggests a two-dimensional structure.

Figure 6.6a displays the scaling exponents E that were determined from the power law fits

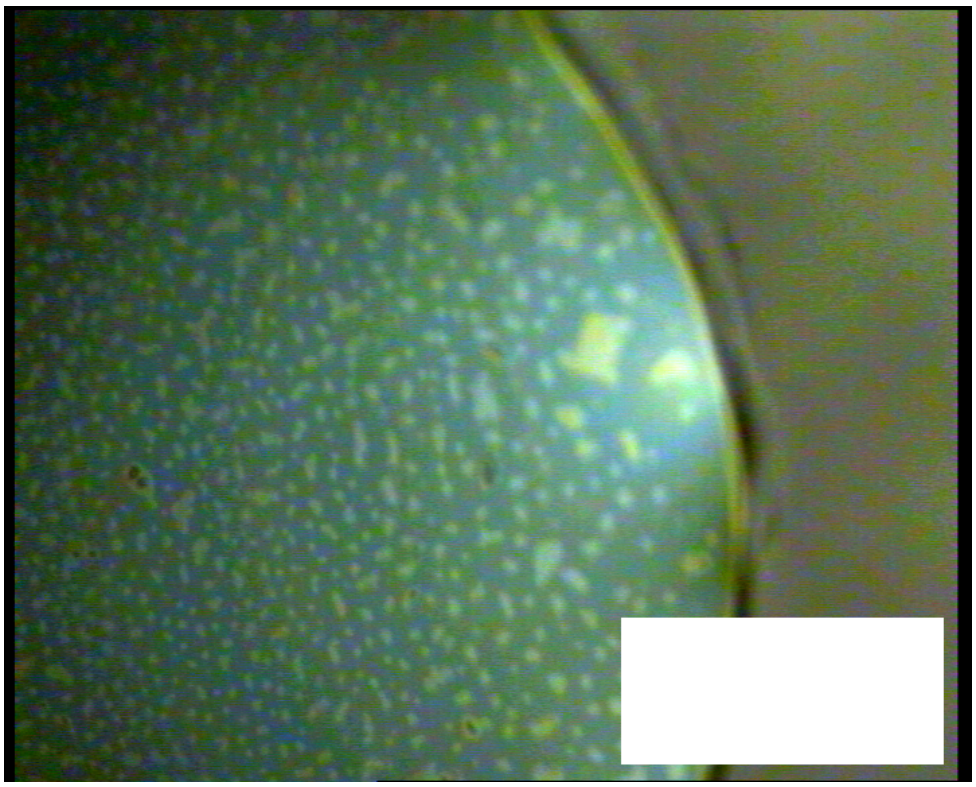

Figure 6.5.: Interfacial aggregation in a thin film pressure balance experiment. The particle aggregates are seen as bright spots. Scale bar corresponds to 100 μm. The image was recorded by Martin Uhlig.

of the experimental data from surface compression. The concentrations were chosen below the flocculation concentration. With increasing amine concentration, a steeper build up of the surface pressure during the surface compression is found, which is reflected by a more negative scaling exponent.

6.2.3. Foaming Behavior

Macroscopic foamability experiments were performed. The samples were prepared by vigorous hand-shaking of 2 mL sample dispersions in a 12 mL vial. The resulting foamability is shown in Figure 6.6b. Photos of the foam samples are shown in Figure 6.7. With increasing alkyl amine concentration, the foamability of the mixed dispersions increases up to the point at which rapid bulk flocculation occurs, as discussed earlier. Interestingly,

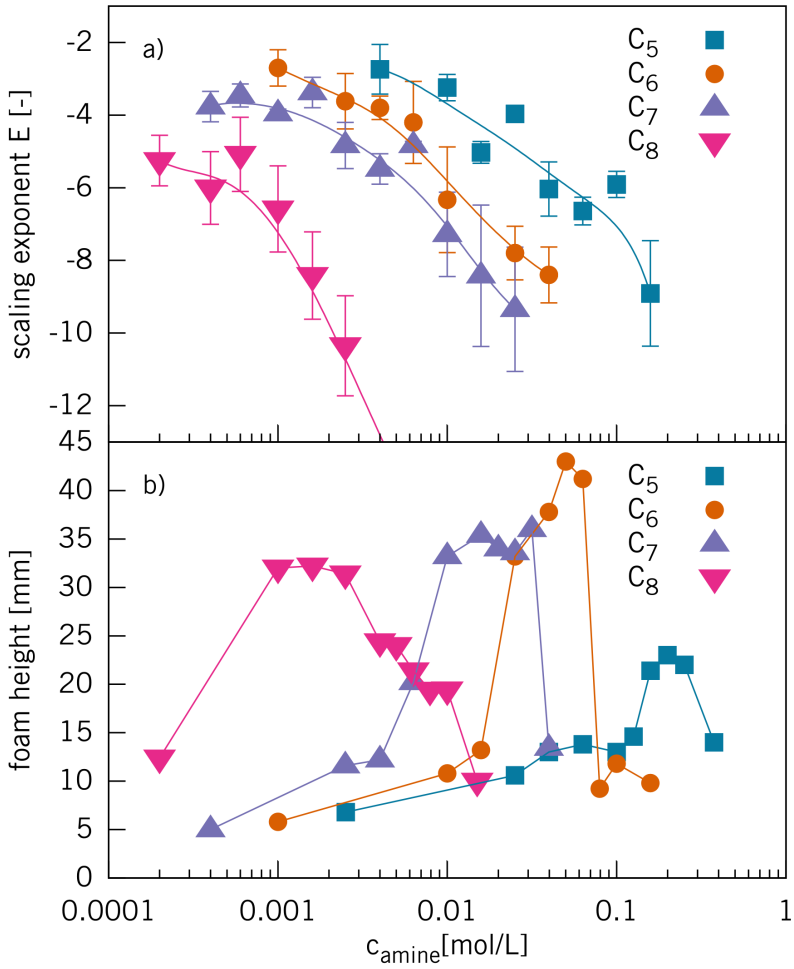

Figure 6.6.: Comparison of a) surface pressure scaling exponent as described in Eq. (6.3) and b) foamability. The foam height increases when the scaling exponent is below -6. Solid lines are guides to the eye.

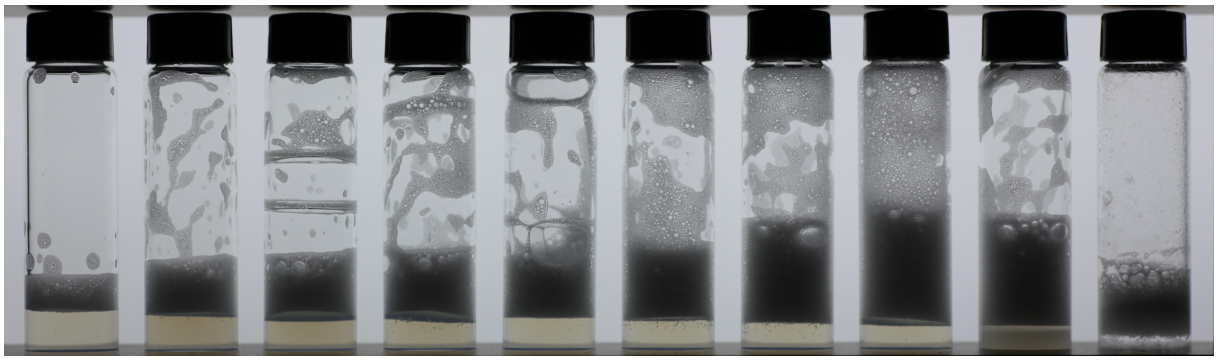

(a) pentylamine (C_5)

(b) hexylamine (C_6)

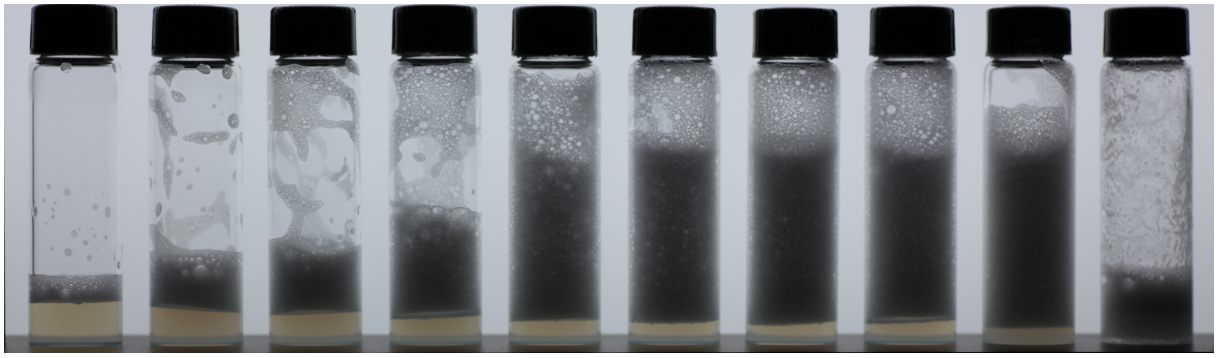

(c) heptylamine (C_7)

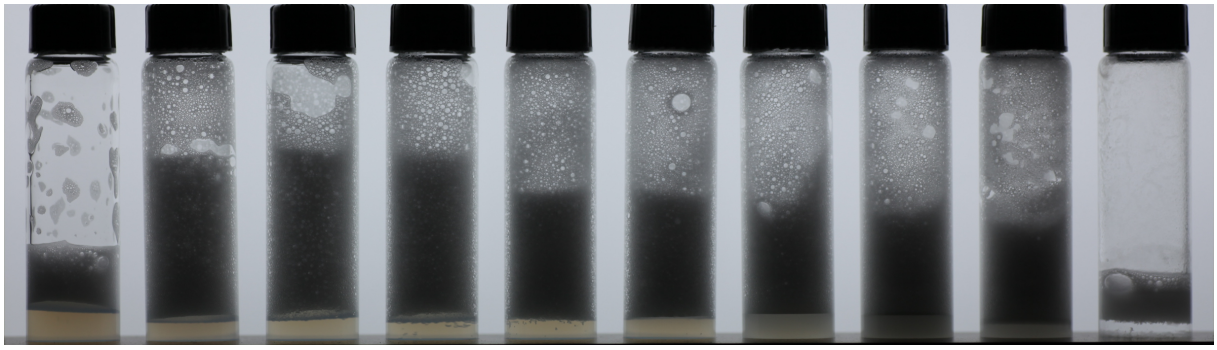

(d) octylamine (C_8)

Figure 6.7.: Foamability of different silica/alkylamine mixtures. The concentrations correspond to the ones used to create Figure 6.6b

as soon as large flocculates are created, the subphase appears clear, as most particles are extracted into the foam phase. At all concentrations below the flocculation concentration, a significant amount of particles remains present in the subphase. Close to the individual amine flocculation concentration, mild aggregation can be visually detected in the subphase, which appears darkened as viewed in transmission. Additionally, the foam stability

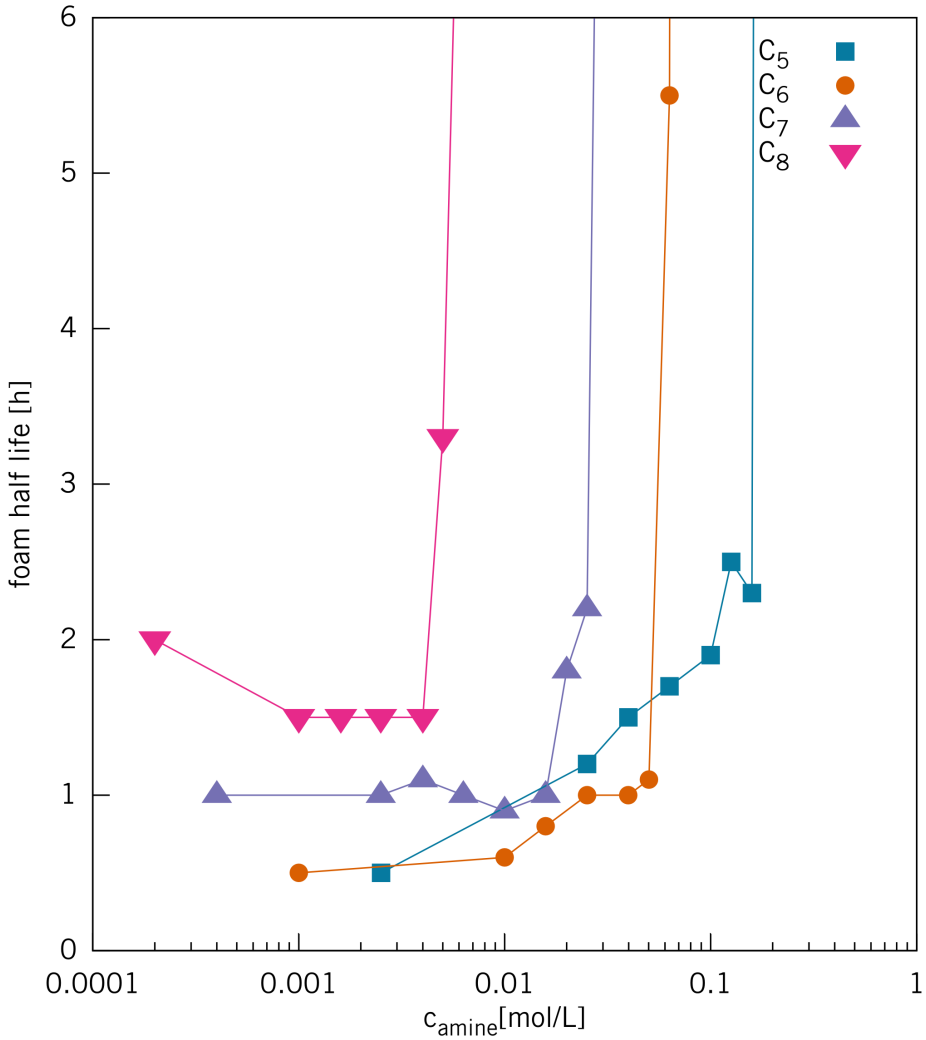

Figure 6.8.: Foam half-life as a function of amine concentration. The sudden increase in foam half-life corresponds to the onset of bulk flocculation.

was monitored over time by taking photographs at regular intervals. As a characteristic value, the foam half-life was chosen, at which the foam height was half the starting value. In Figure 6.8, the foam half-life is depicted as a function of amine concentration. With increasing alkyl amine concentration, the foam half-life stays essentially constant up to the concentration at which also an increased foamability is found. Flocculated samples are stable for several days or even weeks. The most appealing combination of foamability and

foam stability was found for octylamine samples close to the concentration of rapid flocculation, these had a comparatively high foamability and exceptional stability over weeks.

6.3. Discussion

Interesting effects have been seen on all length scales, the aim of this study was to understand how these effects are related to each other. Each length scale will be discussed seperately and to that an overall consistent picture turns up.

The bare silica particles in buffer solution have a zeta potential of -35 mV. Around a zeta potential of -25 mV, rapid bulk flocculation of particles is observed for all carbon chain lengths as depicted in Figure 6.1. This flocculation is reversible when the dispersion is diluted until the amine concentration is reduced below the bulk aggregation concentration. In the frame of the DLVO-theory, -25 mV is the threshold value for which the double layer potential becomes comparable to kT. In order to check whether the aggregation is induced by simple electrostatic screening effects, $MgCl_2$ was added to the bare silica dispersion to increase the ionic strength and compress the electric double layer. The zeta potential was reduced to a value of -22 mV without the onset of bulk flocculation. That means the reduction in zeta potential is not the only reason for the flocculation.

It is clear from Figure 6.2 that the formation of hydrophobic domains in the dispersion is an effect of the presence of silica particles. This effect can be explained by the formation of surface micelles of aggregation number N » 10, large enough to incorporate the pyrene molecule[92,93]. The concentrations at which the I_1/I_3 steps are observed coincide with the onset of flocculation, readily detectable by visual inspection and indicated by vertical lines in Figure 6.1. In the case of surface micellization (sm), it can be expected that the free energy of the process ΔG_{sm} is composed of a sum of a lateral chain-chain interaction free energy ΔG_{lat} and a surface binding free energy ΔG_{surf}. It is assumed that both contributions are mutually independent. The lateral interaction energy is expected to linearly depend on the alkyl chain length n. A first approximation is given by

$$\Delta G_{sm} = n\Delta G_{CH_2} + \Delta G_{surf} \approx kTln(x_{csmc}) \tag{6.2}$$

with ΔG_{CH_2}, the free energy of lateral interaction per CH_2 unit in the carbon chain and x_{csmc} the molar fraction at which hydrophobic moieties were detected as can be seen in

Figure 6.2. Figure 6.9 shows a fit of (6.2) to the experimental data. From the slope, a

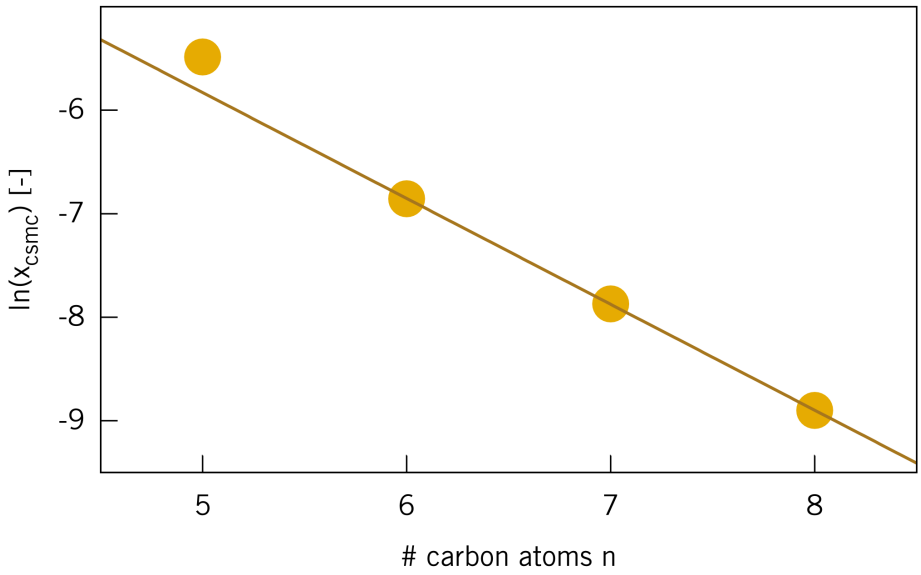

Figure 6.9.: Surface micellization free energy from fluorescence spectroscopy. The surface micellization concentration was measured by using pyrene as a hydrophobic probe. The data were fitted to Eq. (6.2).

lateral interaction free energy ΔG_{CH_2} of 1.0 kT is calculated. This agrees very well to the value found by Studart et al.[54] for an oppositely charged system of short chain carboxylic acids adsorbed onto alumina and is comparable to the value found for ionic long-chain surfactants. The intercept gives a surface binding free energy ΔG_{surf} of 0.7 kT which is comparable to the electrostatic free energy $\Delta E = z\Phi \approx z\zeta$. Herein, $z = +1$ and Φ is taken as the zeta potential of an unmodified silica particle, which will result in a value of $\Delta E = 1.3$ kT. The first point in Figure 6.9, corresponding to pentylamine, was omitted in the fit because including it resulted in $\Delta G_{surf} = 0.0$ kT. This is unphysical since it would imply cooperative binding taking place in the bulk and at the interface at the same concentrations, which is clearly not the case.

Combining the findings of the zeta potential measurements and the fluorescence experiments, the following picture emerges. At concentrations that are low compared to the flocculation concentration of the respective alkyl amine, amine-amine interaction is negligible so isolated adsorption events take place in a Langmuir-type fashion. The apparent surface charge is reduced monotonically with increasing amine concentration. Above a critical threshold concentration the amine adsorption becomes cooperative and hydrophobic patches are created at the particle/water interface. These patches will lead to strong hydrophobic interaction leading to rapid flocculation. The concentrations around 0.01

mol/L are well suited to compare the behavior for different chain lengths in Figure 6.2. Even though the ionic strength is identical at each concentration, the zeta potential is reduced with increasing alkyl chain length representing increasing amounts of amine adsorbed to the particle surface. These findings show that the bulk interaction of the modified silica particles is mainly dominated by the structuring of the amine layer and that electrostatic shielding effects play a minor role regarding particle-particle interaction.

These results prove the assumptions about the cooperative behavior of the amine made by Arriaga et al.[78] who used a silica/pentylamine system, similar to the present study. The fact that the interface is not fully covered before the interface is compressed might be explained by a thermodynamic argument following Reincke et al.[57] by which the adsorbed particles interact mainly via an interaction potential composed of short ranged van der Waals attraction, long ranged dipole-dipole interaction and unscreened Coulomb repulsion which ultimatively prevent a particle surface fraction close to unity. A decreased surface charge, compare Figure 6.1, might lead to reduced electrostatic repulsion which in turn permits a higher particle surface fraction.

Another possibility is that the reduced adsorption is a kinetic effect. There might exist an indefinite adsorption barrier for the interfacial particle adsorption that is reduced by either the adsorption of alkyl amine onto the silica particles or at the air/dispersion interface. A lower barrier would lead to a faster adsorption of particles. Time resolved measurements of the particle adsorption were not within the scope of the study, so no definite decision can be made at this point. In an X-ray study, Stocco et al.[34] as well found an incomplete interfacial coverage in foams stabilized by covalently hydrophobized silica.

From the present results, it seems likely that a prominent change in the particle surface structure at the air/dispersion interface takes place as the alkyl amine concentration approaches the flocculation point. Groot and Stoyanov[87] performed simulations on interfacially adsorbed nanoparticles and also found a power law behavior for the interfacial compression with an exponent varying between -6.5 and -10.5, depending on the structure of the formed particle layer. Using a scaling argument, they arrived a the following expression for the surface pressure

$$\Pi \propto \left(\frac{A}{A_0}\right)^{-\frac{d_s+d_f}{d_s-d_f}} = \left(\frac{A}{A_0}\right)^{E} \tag{6.3}$$

Herein, d_s is the space dimension and d_f is the fractal dimension (Hausdorff dimension) of the 2D aggregated particle cluster. Assuming isolated 2D aggregates which were formed by interfacial particle-particle aggregation, an exponent of ≈ -6 is estimated. Close to the two-dimensional sol-gel transition, the system should behave like a percolated network and the corresponding exponent calculates to -9.5. An excellent agreement is found for these predicted values and the values obtained from the experiments.

Figure 6.6 compares the macroscopic foamability and the surface pressure scaling exponents obtained from the single droplet compression experiments. There is a strong correlation for all systems studied. For scaling exponents between -2 and -4, week foamability is observed. With increasing alkyl amine concentration, the foamability increases, in line with a decrease in the exponent from -4 to -6. An increase in foamability is seen, when the concentration is increased further and the exponent drops below ≈ -6. For carbon chain length C_5 to C_7, an exponent of ≈ -12 is extrapolated for the point of flocculation. Such high values were measured for the octylamine system below the rapid bulk flocculation concentration but indeed, a gentle aggregation of silica particles was observed for these concentrations while the samples were ageing.

In a recent related study, Maestro et al.[15] investigated bubbles with adsorbed C_{16}TAB-coated silica nanoparticles. When the surfactant concentration was increased, the dilatational elastic modulus of the air/dispersion interface increased accordingly. It was shown that the increased elastic modulus can prevent coarsening and slow down the foam evolution. Similar effects as in the present study are assumed to be operative. With increasing amine concentration, the amount of interfacially adsorbed particles increases. The higher concentration of particles at the interface favors the formation of a strong particle network, that will show a high dilatational elastic modulus.

The effects on the different length scales are strongly correlated, so they can be interpreted as a consistent framework. At low amounts of adsorbed amines, as seen from the zeta potential measurements, single isolated particles adsorb to the interface and the surface coverage is low, so that particle-particle interaction is negligible. With increasing adsorption of amines at higher concentrations, the surface coverage increases and the particles start to form isolated networks, floating at the air/solution interface. Upon further increase in amine concentration and hence, a higher particle surface fraction, the particles clusters percolate. As soon as cooperative amine binding takes place, hydrophobic patches on the particles lead to strong hydrophobic interaction and rapid flocculation. The large aggregates in the bulk phase form a gel network in the foam that leads to increased foam lifetime.

With increasing connectivity of the particle network at the bubble interfaces in the foam, the interfaces become more rigid. It has been shown that increased surface rigidity is linked to a deceleration of foam drainage and therefore leads to higher stability of the foam.

6.4. Conclusion

The synergistic effects of short-chain amines combined with silica particles with respect to their foaming behavior were investigated. The data show that the microscopic bulk properties of the dispersions are strongly correlated with the macroscopic foam properties.

For each alkyl chain length, the adsorption of the amines becomes cooperative at a specific concentration. This general behavior is well explained by thermodynamic considerations. The lateral chain-chain interaction energy per CH_2 unit is comparable that found for classical long chain surfactants. For equally long adsorption times, it is found that the interfacially adsorbed amount of silica particles depends on the concentration of the amine. In the frame of the applied theory, this indicates that the interfacial structure of the particles changes from small isolated 2D-aggregates towards a bubble-spanning particle network, which increases foamability.

The experiments on pendant droplets suggest that a higher particle surface coverage and inter-particle connectivity on the foam bubbles leads to a high foamability. It has to be investigated further whether the particle arrangements on a single static foam lamella or bubble are the same as in a foam. There is a subtle balance between foamability and foam stability. When the foam stability is increased due to bulk aggregation of the particles, the foamability is strongly reduced. The increase in stability is explained by a blocking of the Plateau borders which slows down the drainage. On the other hand, bulk aggregation reduces the effective concentration of free particles which are able to adsorb at the air/water interface.

The present study helps to understand the foaming behavior of in-situ hydrophobized silica particles for a comparably low-shear foaming process (shaking by hand).

Chapter 7.

Particle Structure and Dynamics of the Foam*

Abstract

Foams are complex in the sense that they combine multiple ingredients with a wide range of structual length scales and dynamics on various time scales. They belong to the well studied but less well understood systems. Particle stabilized foams are very common in food systems. It is shown that the depletion of the bulk silica concentration during the foam formation can be quantified by precise density measurements. In case of nanoparticle aggregation, more particles are trapped in the foam and will form a network in the foam channels. Diffusing Wave Spectroscopy was used to study the different time and length scales of the composite system. It is found that it is possible to obtain the diffusion coefficient of the particles within the foam by two different approaches. Additionally, the dynamics of the foam network is analyzed and it is confirmed that the formation of an aggregated particle network within the foam is responsible for a decceleration of the foam structure evolution.

Design of experiments, data analysis and evaluation were done by the author. Measurements of the hydrodynamic radii and 60 % of the presented diffusing wave experiments were performed by Judith Witte.

7.1. Introduction

Foams are not transparent because of their large number of refractive index discontinuities. Therefore, they are not conveniently accessible for most optical techniques.

For systems with a high degree of multiple scattering, Diffusing Wave Spectroscopy (DWS) is a useful tool to investigate dynamics and structures at different time and length scales. The theory can be regarded as well-elaborated[94–99] and has found application in various fields of research, especially in the soft matter community[100,101] and food science[102–104]. Examples for systems whose parameters became optically accessible by the use of DWS are highly scattering dispersions[105,106], emulsions[107–109] and foams[110].

*Similar content was presented in A. Carl, J. Witte, and R. von Klitzing, *J. Phys. D: Appl. Phys.*, **2015**, *48*, 434003.

The technique enables to probe the diffusion processes of the constituents in the sample by optical means. Therefore, contactless microrheological measurements can be performed[111–113]. Changes in particle size and network formations be detected[114,115]. Both approaches are used in the research of food colloid systems. In the industry, mouth-feel and flow properties are very important in food product design[116]. Hence, it is desired to obtain information about the correlation of microstructure and the sensory aspect of a food product. Milk is one of the most investigated systems[117,118], especially its response to changes in the environment (pH, temperature, ionic strengh) e.g. in the process of cheese making[119,120]. The temporal evolution of emulsified systems is another topic of interest that can be covered by DWS[121]. Reviews of food systems studied by DWS can be found in the literature[122,123].

As an example of highly light scattering soft matter, foams are suitable candidates to be studies by DWS[124–128]. Durian et al. extensively used Diffusing Wave Spectroscopy to study the temporal and structual features of classical surfactant foams[110,129,130]. From the culinary point of view, foams can be found as e.g. a molecular-kitchen-style gelled foam[131], coffee crema, whipped cream, beer heads or milk-foams[132]. Many of the food foams are stabilized by proteins or aggregates of proteins. These can be regarded as particle stabilized foams with proteins playing the role of the surface active ingredient.

In this kind of systems, a fraction of the present particles is used to stabilize the liquid/air interface. A large fraction of particles remains in the bulk phase that is held up in the foam structure (Plateau borders, vertices)[18,78]. Similar model systems have recently been investigated using hydrophobic aggregates of silica particles[34,133]. These systems possess features at different time and length scales. The nanoparticles are very small compared to the large bubbles of the foam. Likewise, the particle motion is orders of magnitude faster than the dynamics of the foam structure[126,128].

The foams in this study are serving as a general model for particle stabilized foams. Solutions of the aliphatic amines themselves do not show any noticable foamability, in contrast to long-chain surfactants. Crassous and Saint-Jalmes proposed a theoretical framework[128] to analyse DWS data obtained from systems of mixed scatterers like nanoparticles and foam bubbles. It will be shown that this model can be used to explain the experimental results of the presented nanoparticle stabilized foams. It is shown that the particle and foam dynamics are well separated. The particle sizes can be determined in the foam with two different approaches with satisfactory agreement.

7.2. Results

The bulk behavior of the particle dispersions is assessed by DLS measurements. The particle radius is determined as a function of the amine concentration. As can be seen from Figure 7.1, the particle radii remain nearly constant up to a concentration at which aggregation starts. This concentration will be referred to as the critical amine concentration (CAC). The volume fraction of silica used in these measurements was chosen to be 0.005. Above the CAC, at higher silica volume fractions of 0.05, strong aggregation occurs and the samples form a gel within hours. The particle extraction experiments clearly show

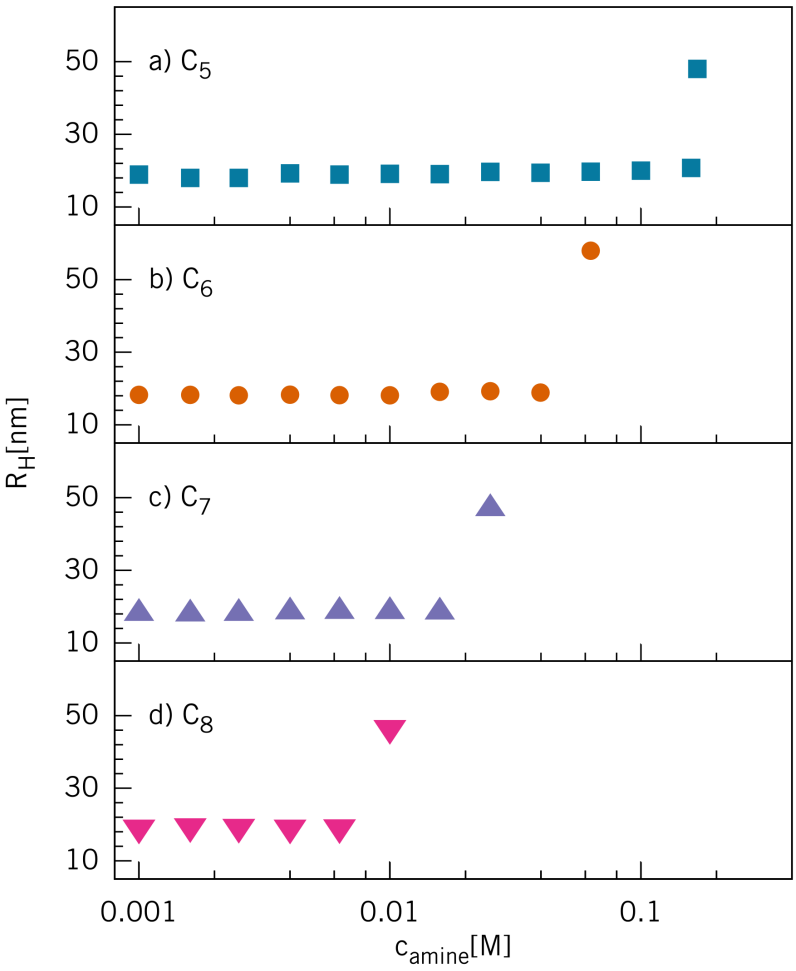

Figure 7.1.: Hydrodynamic radius of the nanoparticles as a function of amine concentration measured by DLS. For all amine carbon chain lengths, aggregation is visible above the critical amine concentration (CAC). Silica concentration 5 g/L.

that the foaming process depletes the bulk phase of silica particles as measured in the

drained liquid. The extracted particle fraction α is calculated from Eq. (4.3). In Figure 7.2, this fraction is plotted as a function of the amine concentration. Approximately linear dependencies are found for the amount of particle depletion and the logarithm of amine concentration. Particle dispersions without additional amines show no foamability. As expected, no foam formation goes along with no change in the particle concentration before and after shaking. Above the CAC, the amount of particles in the drained liquid is strongly decreased compared to the amounts below the CAC. This means that more particles are trapped in the foam above the CAC.

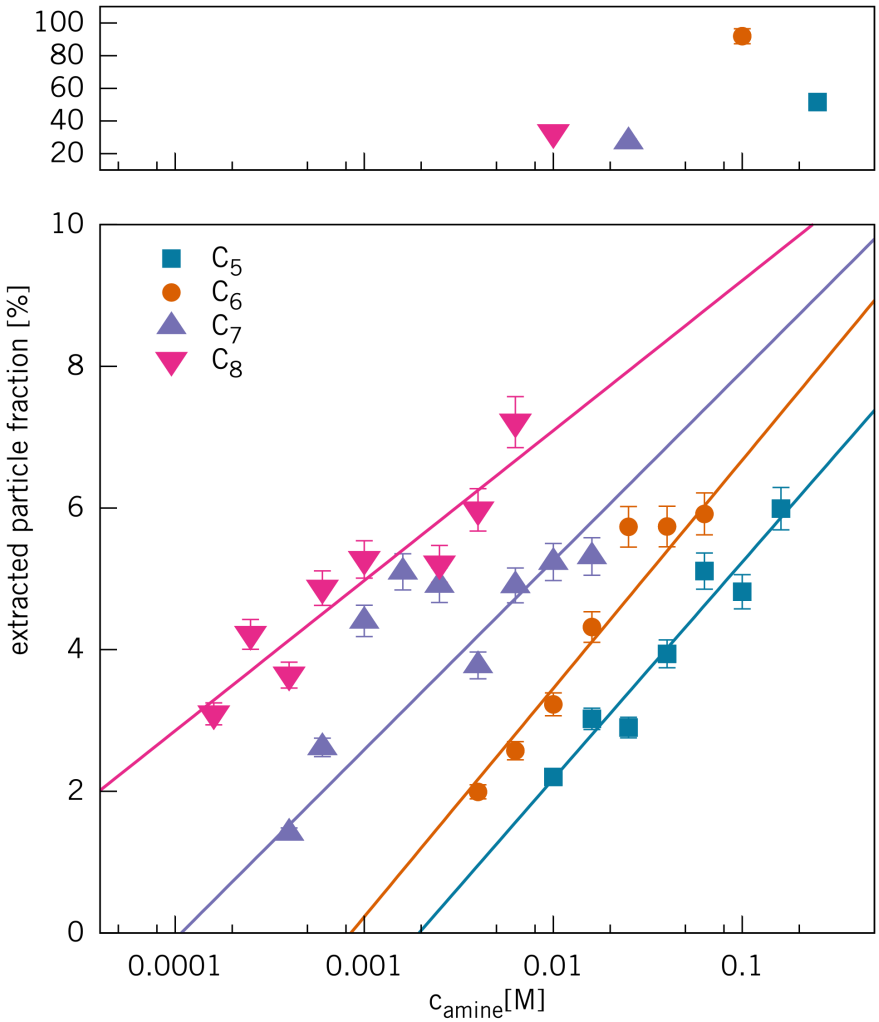

Figure 7.2.: Fraction of particles that are immobilized in the produced foam, as a function of amine concentration and chain length. Above the CAC, a lot of particles are trapped in the foam due to aggregation and gel formation in the foam matrix. Lines are guides to the eye. Silica concentration 25 g/L.

Figure 7.3 shows the dependence of the produced foam volume on the extracted parti-

cle fraction α. A roughly linear dependence is found for low values of α. When large amounts of particles are extracted, the foam volume decreases, this is again coincident with the aggregation of silica particles. Above the CAC, the produced foam volume is strongly reduced compared to the foam volume close to the CAC. The DWS autocor-

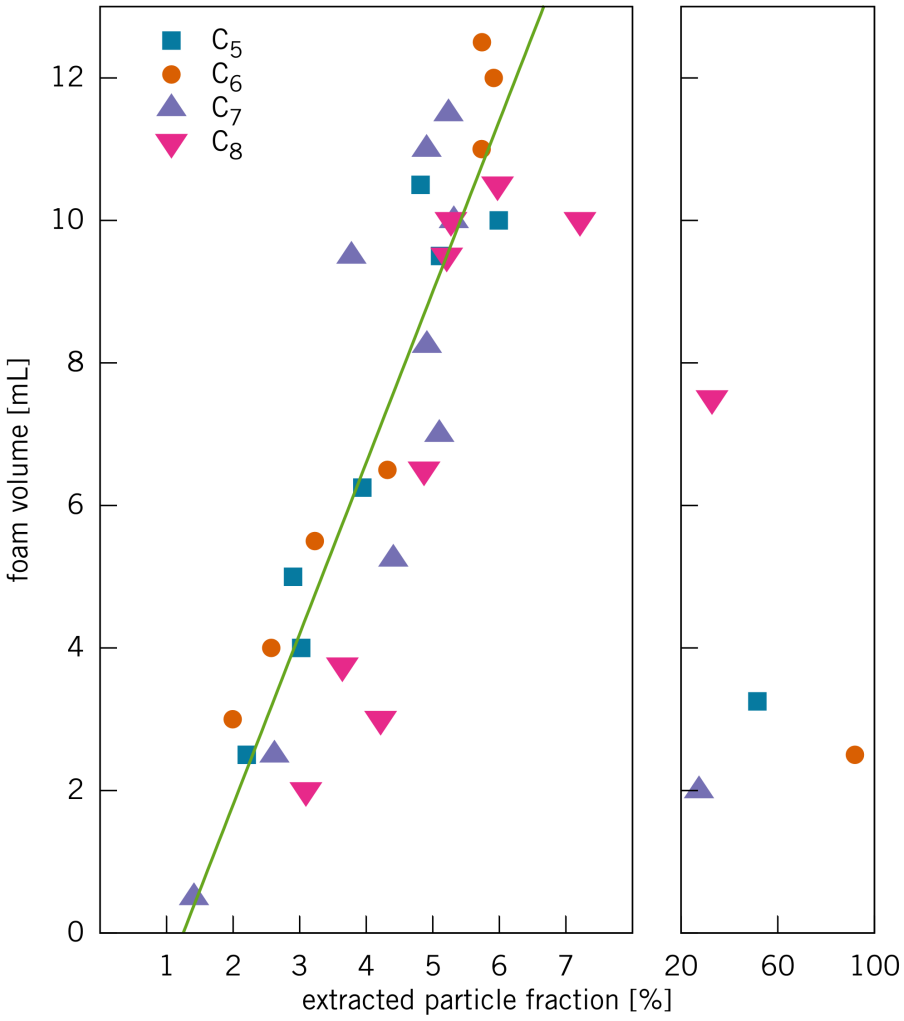

Figure 7.3.: Produced foam volume as a function of extracted particle fraction. The linear dependence indicates an approximately constant number of particles per air bubble. The line serves as guide to the eye. Silica concentration 25 g/L.

relation functions show two temporally separated decays/decorrelations as depicted in a lin-log representation in Figure 7.4a. The decorrelation is caused by dynamics of the scatterers and the matrix. Experiments on foams with and without additional dispersed particles have shown that the first (fast) decorrelation at small lag times τ is caused by particles diffusing within the foam matrix[126]. The second (slow) decorrelation at larger lag times is caused by pronounced dynamics of the foam matrix itself. In Figure 7.4b, the

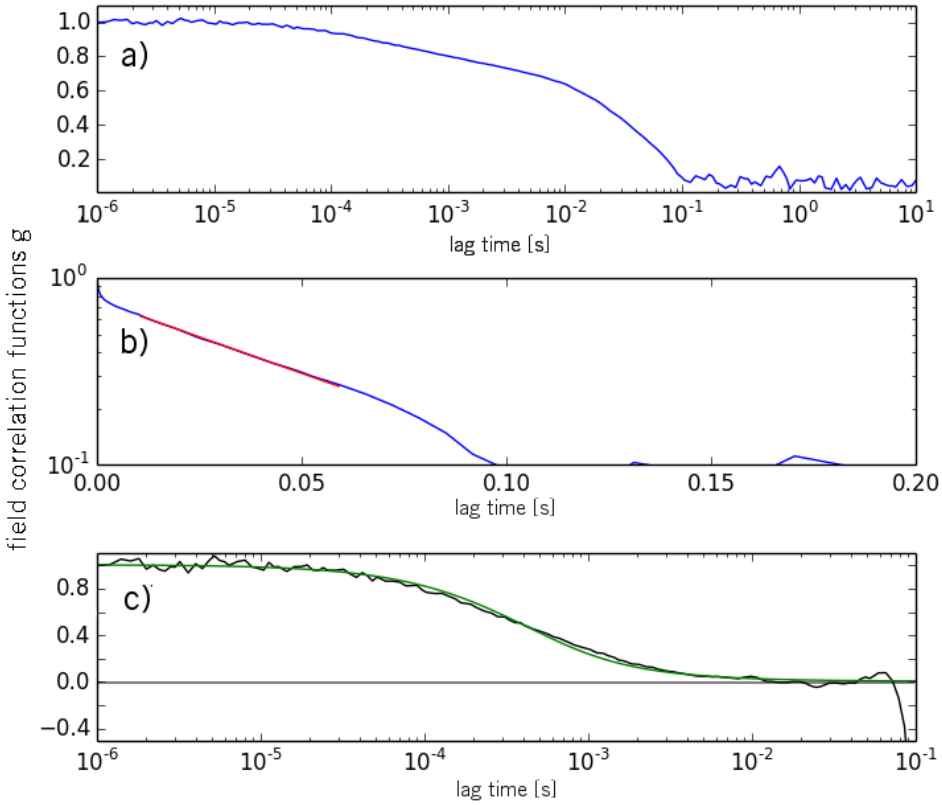

Figure 7.4.: a) lin-log plot of the field autocorrelation function $g_1(\tau)$ of the transmitted light intensity. b) log-lin plot of $g_1(\tau)$ with an exponential fit to extract the characteristic rearrangement time of the foam. c) Field autocorrelation function $g_E^B(\tau)$ as calculated by (7.1) with the corresponding fit to obtain the particle diffusion time. Silica concentration 50 g/L.

data are plotted on a log-lin scale. It can be seen that the second decorrelation is approximately exponential. The corresponding data region can be fitted by a single exponential function $g_E(\tau) = g_E^* \exp(-\tau/\tau_0)$ leading to a respective decay time τ_0 that is a measure for the dynamics of the foam matrix. Additionally, the amplitude g_E^* is a measure for the magnitude of the first decorrelation. Surprisingly, the first decorrelation was almost absent for samples above the CAC.

The following data treatment is heavily based on the approach demonstrated by Crassous and Saint-Jalmes[128]. For a detailed derivation of the theory and the corresponding formulas, the reader may be referred to the original paper. The authors have shown that the first decorrelation signal can be separated from the second decorrelation signal, leading to a field autocorrelation function $g_E^{(B)}$ that solely depends on the signal caused by the particle movements. That particle signal $g_E^{(B)}$ is calculated from the measured autocorrelation

function $g_E(\tau)$ and the fit values of τ_0 and g_E^* through

$$g_E^{(B)}(\tau) = -\frac{\ln \frac{g_E(\tau)}{g_E^* \exp(-\tau/\tau_0)}}{\ln(g_E^*)} \tag{7.1}$$

An example is shown in Figure 7.4c. This extracted signal can be fitted to extract a decay time τ_B that is representative for the motion of the particles in the foam. The theoretical fit function used is

$$g_E^{(B)}(\tau) = \left[1 - \exp\left(-\frac{\tau}{\tau_B}\right)\right] \frac{\tau_B}{\tau} \tag{7.2}$$

Figure 7.5 summarizes the Brownian decay times τ_B as a function of the amine concentration and chain length. The dominant decay time is ≈ 0.23 ms for all the samples studied. This decay time is almost independent of the amine concentration until the CAC where a slight increase is visible. One should keep in mind that the $g_E^{(B)}(\tau)$ signal became comparatively noisy above the CAC. The missing increase for C_5 and C_6 can be explained by assuming fast aggregation at the studied amine concentration above the CAC. In that case, no free aggregates would be detectable. For further analysis, it is necessary to perform further calculations regarding the slow decay times τ_0 which are caused by the foam dynamics. In order to gain comparable information about the foam, the rearrangement time τ_R has to be calculated, which is a measure for how fast the foam structure changes per unit time. Larger values reflect a slower evolution of the foam structures. It can be calculated from τ_0 as follows

$$\tau_R = \frac{\tau_0 L^2}{2(l^*)^2} \tag{7.3}$$

with the sample width L and the transport mean free path length l^*. The transport mean free path length l^* can be calculated from the transmitted intensity I of the sample. With a reference sample of known l^*_{ref}, the sample l^* is calculated by $l^* = (I/I_{ref}) \cdot l^*_{ref}$. Latex particle dispersions of known particle size and concentration were used as the reference. The l^* value of these dispersions is calculated by Mie theory and their transmitted intensity l^*_{ref} is measured. In Figure 7.6, the rearrangement times τ_R are shown as a function of the amine concentration and chain length. The values are averages over the total measurement time for every sample. With increasing amine concentration, the rearrangement time increases and reaches its maximum value at the CAC. This behavior is seen for all amine chain lengths.

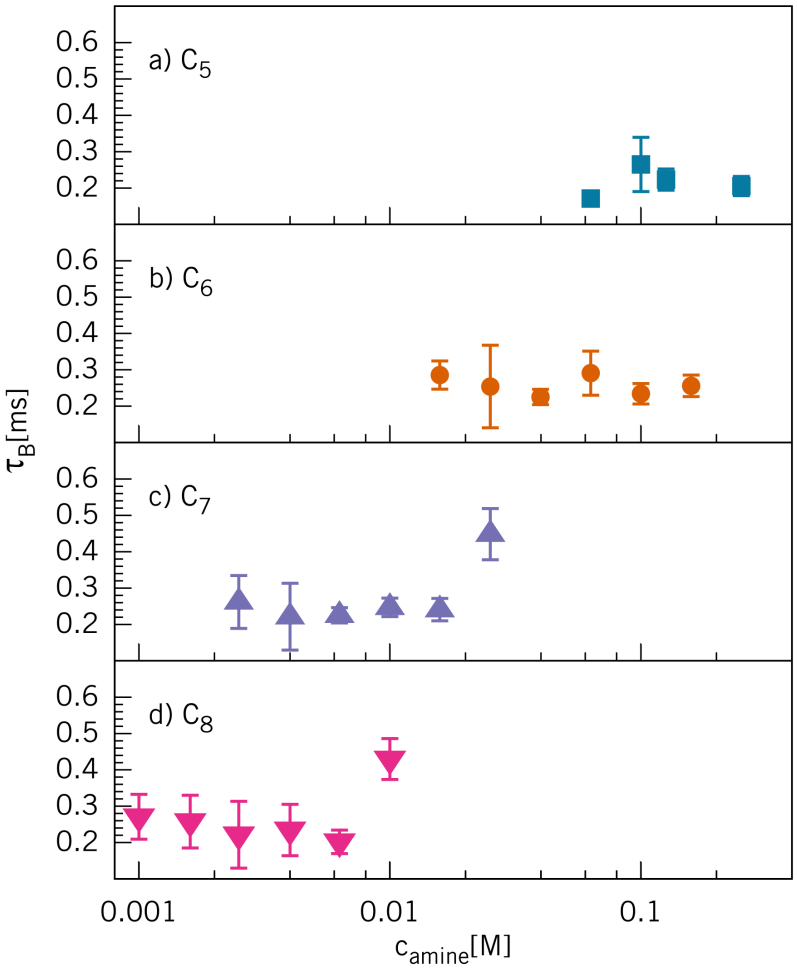

Figure 7.5.: Brownian diffusion time of the particles as a function of amine concentration and chain length. An increase can be seen above the CAC which indicates aggregates. Silica concentration 50 g/L.

Theory predicts a linear dependence of the logarithm of the plateau values g_E^* on the particle volume fraction (*in the foam*). That is, considering the apparent dilution of the bulk particle concentration due to the presence of air bubbles. Since the DWS samples were weighted, the mean liquid fraction Φ_l is known at least at the start of each experiment. The silica particle mass concentration in bulk (no foam) is also known. Depletion effects which were discussed previously are ignored due to their low impact on the bulk particle concentration. With known particle density, the particle fraction Φ_p in the foam can therefore be calculated. The theoretical linear dependence is confirmed in Figure 7.7. Samples above the CAC, where particle aggregation is likely to occur, were not included in the analysis. When aggregation was visible in the sample, the first decorrelation was

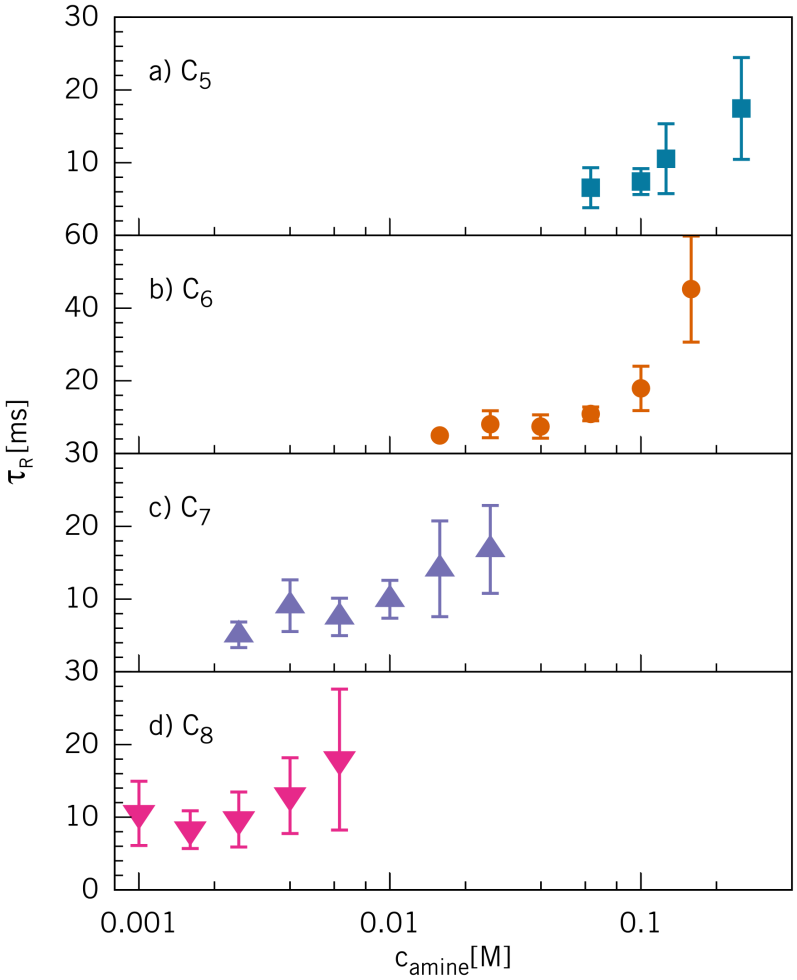

Figure 7.6.: Foam rearrangement times as a function of amine concentration and chain length. Larger times reflect slower dynamics of the foam matrix, namely bubble rearrangements and film ruptures. Silica concentration 50 g/L.

absent in most cases, as stated above.

Linear fits of the slopes for each amine chain length are summarized in the following table. The mean value of l_0^* for the corresponding samples is included for further analysis. Here, l_0^* represents the mean of the transport mean free path length of the foam within the first 5 minutes of the experiment. During this time, no substantial coarsening was observed.

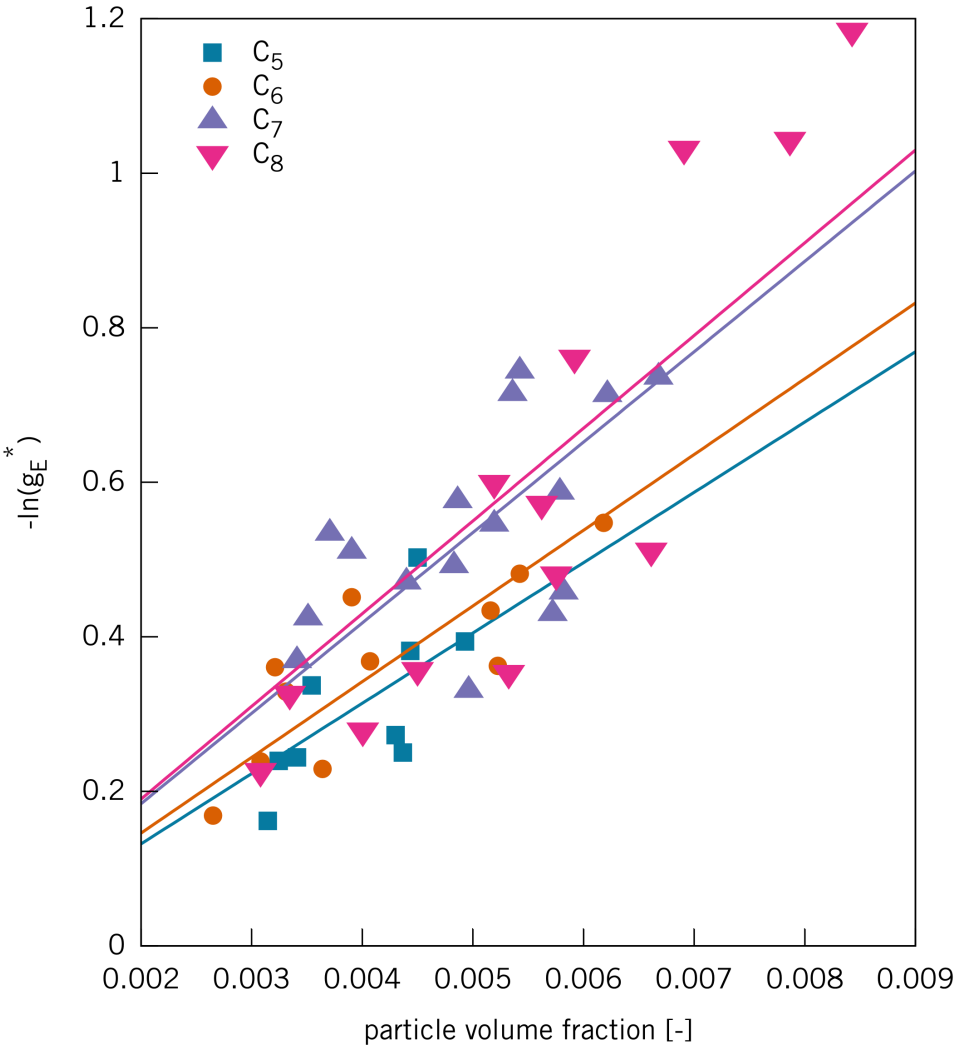

Figure 7.7.: Logarithm of plateau value g^* between the two decays of the autocorrelation function $g_1(\tau)$ as a function particle volume fraction. The linear relation can be fitted to yield a measure of the particle size. Silica concentration 50 g/L.

7.3. Discussion

It is clear from the results that the aggregation of the particles at the CAC has a pronounced influence on the structure and dynamics of the foam matrix. The bulk behavior of the particle dispersions, how this influences their foaming behavior and illustrate the efficiency of DWS in characterizing the system will be discussed.

It has been shown earlier that the adsorption of short-chain amines onto silica particles obeys the same rules as classical surfactants[54,133]. In the beginning, there are isolated adsorption events. The adsorption of the hydrophobic amines will render the particles

$\mathbf{C}_n$	**slope**	l_0^* [μm]
C_5	78±6	191±57
C_6	86±5	209±68
C_7	107±6	174±22
C_8	111±8	154±34

surface active. Above a critical surfactant concentration, the amine adsorption becomes cooperative. This leads to hydrophobic interaction between the particles and therefore, the particles aggregate.

When a dispersion of hydrophobic particles is foamed, some of the particles will go to the interface. These particles will therefore be removed from the liquid that drains out of the foam. This depletion can be quantified with density measurements, as demonstrated in this study. Boos et al. showed that the surfactant depletion for classical surfactant foams is measureable[134]. The amount of particles that is removed from the bulk phase depends on the concentration of the amines and their chain length. With increasing hydrophobicity, the particles seem to be more capable to stabilize a foam during the foaming procedure. Below the CAC, the foam volume increases when more particles are extracted from the bulk. This means that the number of extracted particles per unit volume of foam is constant. In turn, this supports a hypothesis that the in-plane interaction of the adsorbed particles is more important for their foaming behavior than simply the number of adsorbed particles.

Above the CAC, a drastic decrease of foam volume is found while simultaneously the number of particles that are trapped in the foam strongly increases. The reduced foamability can be explained with the reduction of free small particles, since aggregation is taking place. In a previous study, it was found that aggregation significantly increases the foam life-time[133]. Large particle aggregates are easily trapped in the Plateau borders and vertices[17]. These aggregates will not drain out of the foam, so the draining liquid is strongly depleted of particles. Additionally, these particles can form a gel, which slows down the dynamics of the foam.

As stated before, the DWS data analysis is based on the model published by Crassous and Saint-Jalmes[128]. The model applies very well to the presented composite particle-foam system. In order to discuss the DWS data, it is convenient to briefly sketch the parameters of the studied system. Diffusing wave spectroscopy relies on multiple scattering of the photons travelling through the sample. The idea is that photons travel through the sample in random walk steps, like in a diffusion process. An important parameter is the transport mean free path length l^* which is the distance after which a photon has randomized its

direction with respect to the incident direction. It corresponds to the random walk step length.

For unfoamed particle dispersions, the transport mean free path length can be calculated in the framework of Mie scattering theory. First, the mean free path of the colloidal dispersion l_c is calculated via $l_c = 1/\rho\sigma$ with the particle number density ρ and the particle scattering cross-section σ. The transport mean free path length is calculated as $l_c^* = l_c/(1-\chi)$ with the asymmetry parameter χ. The size of the asymmetry parameter χ it between 0 and 1. The larger the value of χ, the more directed is the scattering towards certain scattering angles. Figure 7.8 displays l_c and l_c^* as a function of the particle radius at constant mass concentration. With increasing radius, the particle number density ρ decreases but the scattering cross-section σ_{scat} increases leading to a decrease in the mean free path l_c. For Rayleigh scatterers, the direction of a photon is randomized after a single scattering event. In this case the relation simply is $l_c^* = l_c$. In the Mie scattering regime, l_c^* is always larger than l_c. Multiple scattering events are necessary in this regime to randomize the photon direction because a single scattering event is strongly directed.

For the dispersion, the hydrodynamic radius determined by DLS and the mass concentration used in DWS were used to calculate the transport mean free path $l_c \approx l_c^* = 13$ mm. This is the mean distance between two scattering events in the unfoamed dispersion. The foams in this study have a void fraction of 80 % which will increase the effective colloidal transport mean free path length to $l_c^* = 65$ mm due to apparent dilution of the dispersion. The length of 65 mm is large compared to the cell width L= 5 mm. It is instructive to compare the transport mean free path length of 65 mm to the length of the photon path through the foam sample. The photon path length can be calculated from the scattering properties of the foam and the thickness of the sample cell. The l_f^* of the fresh foam is in the order of 200 μm and small compared to the cell width. There are two different transport mean free path lengths l_c^* and l_f^* in the system. The effective transport mean free path lengths l^* is calculated via

$$\frac{1}{l^*} = \frac{1}{l_f^*} + \frac{1}{l_c^*} \tag{7.4}$$

In this study, the $1/l_c^*$ can be neglected and it follows $l^* \approx l_f^*$. The effective transport mean free path will be referred to as l^* in the further discussion.

In general, the l^* depends on the bubble size and increases as coarsening of the foam matrix proceeds. Knowing the liquid fraction of $\approx$ 20 %, the mean bubble size can be estimated to be in the order of 100 μm[135], which is reasonable for the used foaming

method. A photon travelling through the sample will be randomized mainly by refraction on the foam bubbles. It is possible to estimate the dominant path length of a photon through the sample by $L^2/l^* = 125$ mm. Comparing this path length to $l_c^* = 65$ mm, it is clear that a noticable fraction of the transmitted photons will have been scattered by a particle. At the same time, is is unlikely to see multiple scattering caused by particles. In other words, the foam bubbles produce an isotropic field of incident photons which are likely to be scattered once from a particles before eventually exiting the sample cell.

Paths that include a particle scattering event also lead to fluctuations in the transmitted intensity on the timescale of the particle diffusion. This is the reason for the first decorrelation in Figure 7.4a. The second decorrelation is caused by bubble rearrangement and coalescence events. The larger the second decorrelation time, the slower is the evolution of the foam matrix.

From the first decay time τ_B of ≈ 0.23 ms an apparent particle radius can be calculated via

$$R_h = \frac{8\tau_B \pi k T}{3\lambda^2 \eta} \tag{7.5}$$

with the laser wavelength λ and the liquid dynamic viscosity η. This yields an apparent radius of 28 nm. Within the experimental accuracy, this is in acceptable agreement with the DLS radius of 20 nm. For amine concentrations above the CAC, the particles start to aggregate while the mass concentration is constant. This should lead to a larger decay time. Slightly larger decay times that indicate larger particles are observed which confirm the presence of aggregates in the foam channels.

The second decay time τ_R increases with increasing amine concentration which indicates that the foams evolve slower. This can be interpreted as a stiffening of the system which is also qualitatively observed when handling the prepared foams. Foams with strongly aggregated particle networks show a time dependent increase in the τ_R value, as the systems ages and gels.

In the following,the plateau values g_E^* will be discussed. Theory predicts the following dependence

$$-\ln(g_E^*) = \frac{L^2}{2l^* l_c} = \frac{L^2 \sigma}{3\pi l^* d^3}\Phi_c \tag{7.6}$$

with the measured transport mean free path length l^*. The right-hand side of (7.6) can be used to evaluate the fits in Figure 7.7. If both the cross-section σ_{scat} and the diameter d of the particles are unknown, it is straightforward to calculate the ratio σ/d^3 from the slope of the curves and find e.g. the diameter by comparison with data calculated by means of Mie theory. When this is applied to the measured data, the particle radii r_{app} are found as summarized in the following table.

$\mathbf{C}_n$	σ/d^3 **[1/m]**	r_{app} **[nm]**
C_5	5617	28.8
C_6	6776	30.8
C_7	7019	30.9
C_8	6444	30.3

These values are larger than the hydrodynamic radii probed by DLS. Nonetheless, it should be noted that they compare very well to the apparent radii of 28 nm extracted from the τ_B values. Both methods which were presented to obtain a measure for the particle size in the foam are different in their approach. One uses information from the decorrelation time, the other one is based on the total amount of decorrelation. Modelwise there is no correlation between those information. Another aspect of the information in the g^* values shall be addressed. Assuming the silica particles in the foam channels start to aggregate, their l_c value would decrease as depicted in Figure 7.8 and explained earlier. Equation (7.6) shows the dependence of the plateau value g_E^* on l_c. It turns out that aggregation should lead to a decrease of the plateau value g_E^*. This decrease is not observed. The opposite is found, in samples with strong aggregation the plateau is nearly absent. An easy explanation is the gelation or settling of the aggregates in the foam structure as depicted in Figure 7.9 and 7.10. As these large aggregates do not move any longer, they cannot cause any decorrelation in the transmitted beam intensity. Only freely diffusing particle (aggregates) contribute to the fast decorrelation signal in Figure 7.4c.

7.4. Conclusion

The structure and dynamics of an aqueous particle stabilized foam were investigated. The data suggest that the foam structure and dynamics depend on the interfacial particle interaction as well as the particle aggregation state in the bulk foam liquid.

For all studied alkyl chain lengths, there exists a characteristic amine concentration that leads to immediate particle aggregation. Below this threshold concentration, particles

become more efficient foam stabilizers as the amine concentration is increases. The amine adsorption leads to increased hydrophobicity of the particles. A decrease in the foam rearrangement time is found, as the hydrophobicity of the particles is increased. The nanoparticle diffusion can be probed by DWS and their size can be determined in the foam. When two of the three parameters particle mass concentration, particle size and foam liquid fraction are known, the third one can be conveniently determined by means of DWS. Two independent approaches to determine the particle size in the foam were validated successfully.

When the particle hydrophobicity is increased to a degree at which bulk aggregation starts, the foam structure gels as reflected by the long foam rearrangement times. The arrest of single particle dynamics is seen by the absence of a strong particle induced fast decorrelation in the autocorrelation function.

The present study illustrates the power of the Diffusing Wave Spectroscopy technique to characterize complex composite materials that include several largely separated length scales. It illustrates how a component of the matrix can be probed optically without the need for the sample to be transparent or optically homogeneous.

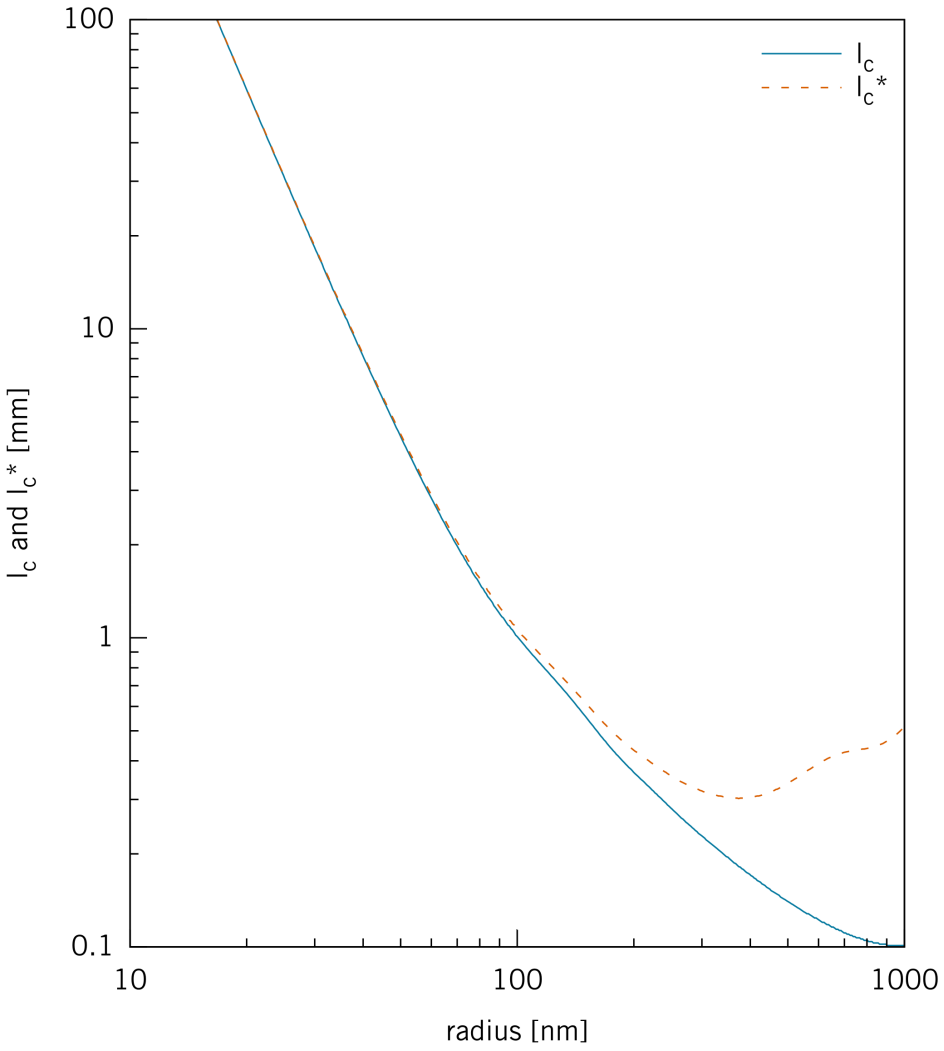

Figure 7.8.: Theoretical values of the (transport) mean free path lengths l_c and l_c^* as a function of particle radius at constant silica mass concentration of 10 g/L. The l_c values are the mean distance between two scattering events in an unfoamed dispersion. The l_c^* values represent the step length after which the photon direction has been randomized in the same system.

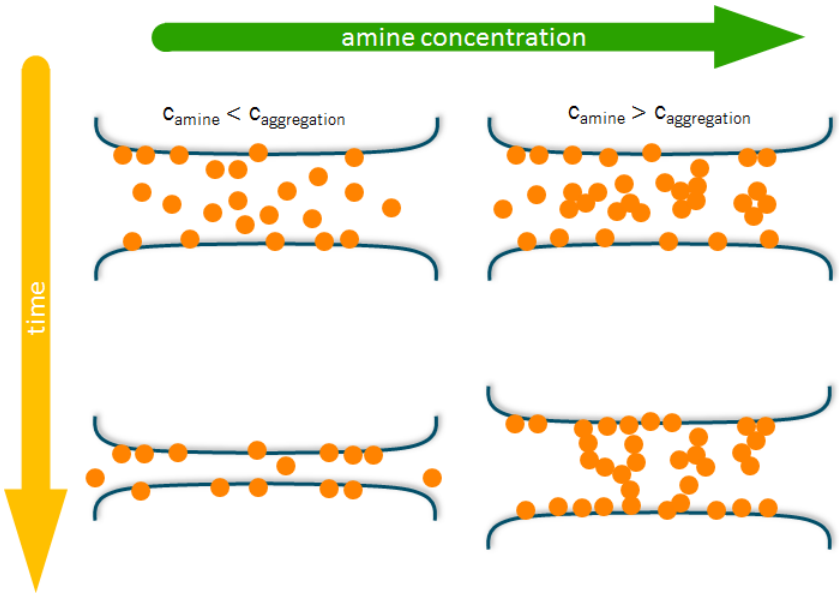

Figure 7.9.: Ageing of the foam films below and above the CAC. Below the CAC, particles remain isolated and the liquid drains out of the foam. Above the CAC, particle aggregates will prevent the film from thinning which slows down coarsening and coalescence.

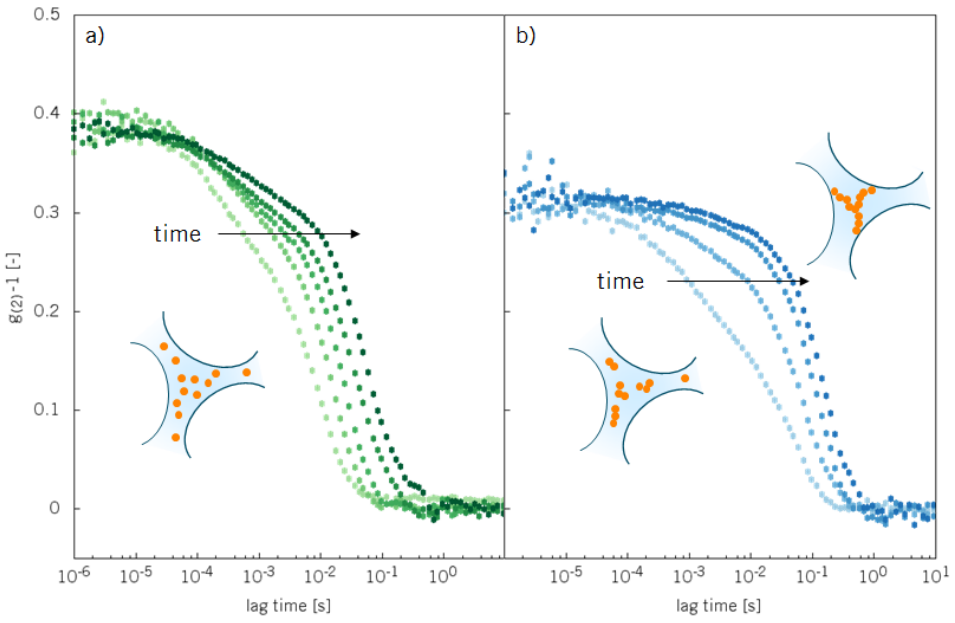

Figure 7.10.: Ageing of the Plateau borders a) below and b) above the CAC. Below the CAC, particles remain isolated and the liquid drains out of the foam. Above the CAC, particle aggregates will prevent the liquid from draining which slows down the ageing processes.

Chapter 8.

Summary and Outlook

In the present thesis, the complex structure and dynamics of particle stabilized foams are investigated. It is found that interaction between the short-chain alkyl amines and the silica nanoparticles is strongly synergistic with respect to the system's foaming behavior.

The observed properties are general for all used alkyl chain lengths. With increasing chain length, the observed effects are shifted to lower concentrations. With increasing amine concentration, increased amounts of amine adsorb at the particle interface. Above a critical amine concentration (CAC), there are considerable alkyl-alkyl chain interactions of the adsorbed amines. Hydrophobic domains or patches form due to these interactions. The hydrophobic patches lead to strong hydrophobic interaction of the particles and eventually particle aggregation. Bulk characterizations are shown in Section 6.2.1.

Even below the CAC, changes in the interfacial behavior of the nanoparticles are observed. Mechanical studies of the interfacial layer are compatible with the formation of a fractal network. The network becomes increasingly dense with increasing hydrophobicity, as explained in Section 6.2.2. For very low amine concentrations, the particles are isolated at the interface. When the hydrophobicity is increased, small 2D aggregates are expected to form. Close to the CAC, a bubble spanning particle network is assumed. A high degree of particle/network cross-links leads to increased foamability, as described in Section 6.2.3.

A model was developed in Section 5.2.2 to non-invasively probe the contact angle. The increasing hydrophobicity is evidenced by an increase in the particle contact angle, measured by X-ray Reflectivity. The particles will become moderately hydrophobic with contact angles below 45°. A simple geometrical model estimates the energy of detachment to be at least two orders of magnitude above the thermal energy. This means, the particles adsorb irreversibly at the interface as explained in Section 5.3.

For long adsorption times, the interface becomes packed with particles, close to the maximum packing fraction. This was shown by theoretical calculations in Section 5.2.3 and the results from the XRR study.

Foams from particle dispersions at amine concentrations close to the CAC show a slow down in the foam ageing. This is evidenced by an increase in the slower DWS decay rate in Section 7.2. It can also be explained by the formation of a stiff network around the bubbles, which decellerates foam evolution, as explained above. Two independent methods in Section 7.3 show that the non-adsorbed particles in the foam liquid phase are unaggregated below the CAC. Close to the CAC, slight particle aggregation can be

observed in the foam. Above the CAC, particle aggregates are entrapped in the foam liquid channels. The fast decay signal in the DWS correlation curve disappears which is a clear indication of hindered diffusion of the aggregates. This is caused by slight gelation of the liquid components of the foam. Additionally, the foams are drastically stabilized above the CAC as discussed in Sections 6.2.3 and 7.3.

A detailed picture of the mechanism of foam stabilization is established for the studied system. Generality is found for different chain lengths of surfactant. Hence, it is expected that the results are applicable to a wide range of surfactant-particle systems beyond the present study.

A graphical overview of the results is given in Figure 8.1.

Since the mechanisms are understood on different lengths and time scales, they can be used to design particle stabilized foams with tailor-made properties. Additionally, the knowledge about the mechanisms can be exploited in future studies to create responsive foam systems.

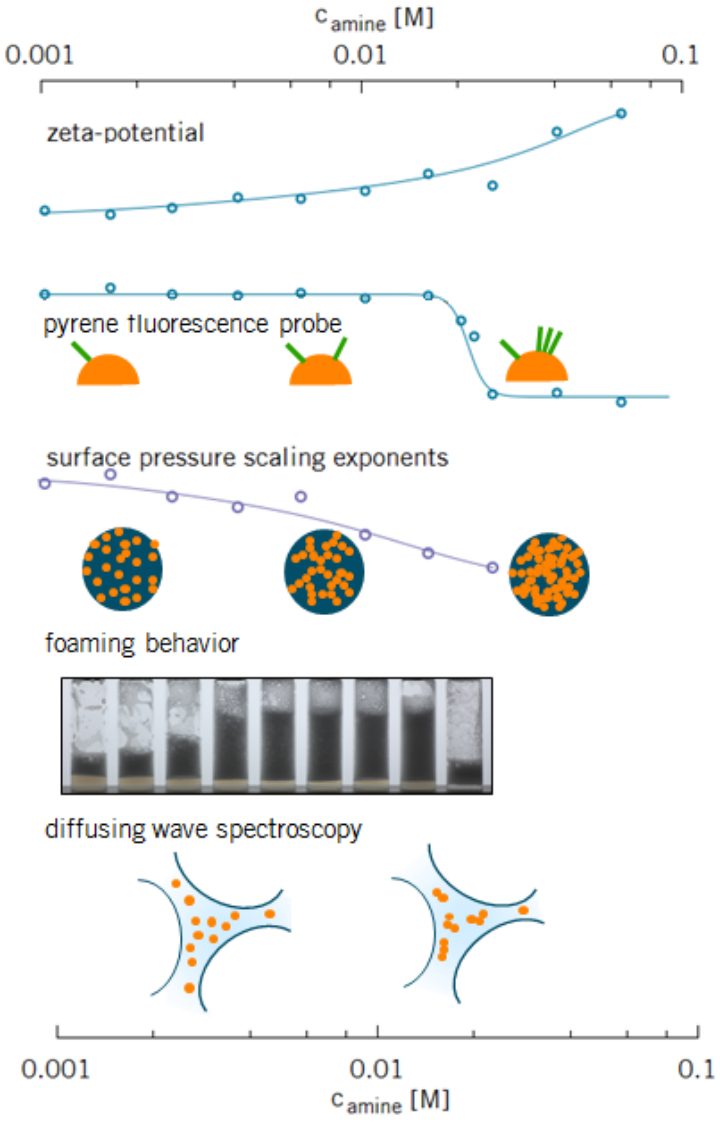

Figure 8.1.: Conceptual and qualitative summary of the results. The results are general for all amine chain lengths, the exact concentration range varies.

Bibliography

[1] B. Binks, *Current Opinion in Colloid & Interface Science* **2002**, *7*, 21–41.

[2] B. P. Binks, T. S. Horozov, *Angew. Chem.* **2005**, *117*, 3788–3791.

[3] B. P. Binks, A. Rocher, M. Kirkland, *Soft Matter* **2011**, *7*, 1800–1808.

[4] P. Pieranski, *Phys. Rev. Lett.* **1980**, *45*, 569–572.

[5] D. A. Weitz, M. Oliveria, *Phys. Rev. Lett.* **1984**, *52*, 1433–1436.

[6] M. Lin, H. Lindsay, D. Weitz, R. Klein, R. Ball, P. Meakin, *Journal of Physics: Condensed Matter* **1990**, *2*, 3093.

[7] A. Marchand, J. H. Weijs, J. H. Snoeijer, B. Andreotti, *American Journal of Physics* **2011**, *79*.

[8] V. B. Fainerman, V. I. Kovalchuk, E. H. Lucassen-Reynders, D. O. Grigoriev, J. K. Ferri, M. E. Leser, M. Michel, R. Miller, H. Möhwald, *Langmuir* **2006**, *22*, 1701–1705.

[9] S. Huang, K. Gawlitza, R. von Klitzing, L. Gilson, J. Nowak, S. Odenbach, W. Steffen, G. K. Auernhammer, *Langmuir* **2016**, *32*, 712–722.

[10] E. Santini, J. Krägel, F. Ravera, L. Liggieri, R. Miller, *Colloids Surf., A* **2011**, *382*, 186–191.

[11] C. P. Whitby, D. Fornasiero, J. Ralston, L. Liggieri, F. Ravera, *The Journal of Physical Chemistry C* **2012**, 3050–3058.

[12] A. Maestro, E. Guzmán, E. Santini, F. Ravera, L. Liggieri, F. Ortega, R. G. Rubio, *Soft Matter* **2011**, *8*, 837–843.

[13] D. Georgieva, A. Cagna, D. Langevin, *Soft Matter* **2009**, *5*, 2063–2071.

[14] A. Cervantes Martinez, E. Rio, G. Delon, A. Saint-Jalmes, D. Langevin, B. P. Binks, *Soft Matter* **2008**, *4*, 1531–1535.

[15] A. Maestro, E. Rio, W. Drenckhan, D. Langevin, A. Salonen, *Soft Matter* **2014**, *10*, 6975–6983.

[16] D. Weaire, S. Hutzler, *The Physics of Foams*, Clarendon Press, **2001**.

[17] F. Carn, A. Colin, O. Pitois, R. Backov, *Soft Matter* **2011**, *8*, 61–65.

[18] F. Carn, A. Colin, O. Pitois, M. Vignes-Adler, R. Backov, *Langmuir* **2009**, *25*, 7847–7856.

[19] P. Stevenson, *Current Opinion in Colloid & Interface Science* **2010**, *15*, 374 – 381.

[20] E. Solorzano, S. Pardo-Alonso, J. de Saja, M. Rodriguez-Perez, *Colloids and Surfaces A: Physicochemical and Engineering Aspects* **2013**, *438*, 159 – 166.

[21] M. B. J. Meinders, W. Kloek, , T. van Vliet, *Langmuir* **2001**, *17*, 3923–3929.

[22] V. Carrier, , A. Colin, *Langmuir* **2003**, *19*, 4535–4538.

[23] V. Bergeron, A. Waltermo, , P. M. Claesson, *Langmuir* **1996**, *12*, 1336–1342.

[24] D. Kashchiev, D. Exerowa, *Journal of Colloid and Interface Science* **1980**, *77*, 501 – 511.

[25] C. Stubenrauch, R. von Klitzing, *Journal of Physics: Condensed Matter* **2003**, *15*, R1197.

[26] R. Klitzing, A. Espert, A. Asnacios, T. Hellweg, A. Colin, D. Langevin, *Colloids and Surfaces A: Physicochemical and Engineering Aspects* **1999**, *149*, 131 – 140.

[27] Y. Zeng, S. Schön, A. Carl, R. von Klitzing in *Colloid Process Engineering*, Springer, **2015**, pp. 3–19.

[28] I. E. Dzyaloshinskii, E. M. Lifshitz, L. P. Pitaevskii, *Soviet Physics Uspekhi* **1961**, *4*, 153.

[29] H. Dörfler, *Grenzflächen und kolloid-disperse Systeme: Physik und Chemie*, Springer, **2002**.

[30] P. M. Dove, C. M. Craven, *Geochimica et Cosmochimica Acta* **2005**, *69*, 4963 – 4970.

[31] B. H. B. Tatiana P. Goloub, Luuk K. Koopal, M. P. Sidorova, *Langmuir* **1996**, *12*, 3188–3194.

[32] P. Somasundaran, T. W. Healy, D. W. Fuerstenau, *The Journal of Physical Chemistry* **1964**, *68*, 3562–3566.

[33] B.-Y. Zhu, T. Gu, *Advances in Colloid and Interface Science* **1991**, *37*, 1 – 32.

[34] A. Stocco, F. Garcia-Moreno, I. Manke, J. Banhart, D. Langevin, *Soft Matter* **2011**, *7*, 631–637.

[35] J. B. German, M. J. McCarthy, *Journal of Agricultural and Food Chemistry* **1989**, *37*, 1321–1324.

[36] A. J. Meagher, M. Mukherjee, D. Weaire, S. Hutzler, J. Banhart, F. Garcia-Moreno, *Soft Matter* **2011**, *7*, 9881–9885.

[37] A. J. Meagher, D. Whyte, J. Banhart, S. Hutzler, D. Weaire, F. Garcia-Moreno, *Soft Matter* **2015**, *11*, 4710–4716.

[38] V. Garbin, J. C. Crocker, K. J. Stebe, *Journal of Colloid and Interface Science* **2012**, *387*, 1–11.

[39] S. Kinge, M. Crego-Calama, D. N. Reinhoudt, *ChemPhysChem* **2008**, *9*, 20–42.

[40] Y. Lin, *Science* **2003**, *299*, 226–229.

[41] F. C. Meldrum, N. A. Kotov, J. H. Fendler, *The Journal of Physical Chemistry* **1994**, *98*, 4506–4510.

[42] F. Reincke, S. G. Hickey, W. K. Kegel, D. Vanmaekelbergh, *Angewandte Chemie International Edition* **2004**, *43*, 458–462.

[43] B. P. Binks, M. Kirkland, J. A. Rodrigues, *Soft Matter* **2008**, *4*, 2373–2382.

[44] L.-H. Chen, A. Dudek, Y.-L. Lee, C.-H. Chang, *Langmuir* **2007**, *23*, 3123–3127.

[45] S. I. Karakashev, O. Ozdemir, M. A. Hampton, A. V. Nguyen, *Colloids and Surfaces A: Physicochemical and Engineering Aspects* **2011**, *382*, 132–138.

[46] M. D'Souza Mathew, M. S. Manga, T. N. Hunter, O. J. Cayre, S. Biggs, *Langmuir* **2012**, *28*, 5085–5092.

[47] S. Fujii, A. J. Ryan, S. P. Armes, *Journal of the American Chemical Society* **2006**, *128*, 7882–7886.

[48] E. Santini, E. Guzmán, F. Ravera, A. Ciajolo, M. Alfè, L. Liggieri, M. Ferrari, *Colloids and Surfaces A: Physicochemical and Engineering Aspects* **2012**, *413*, 216–223.

[49] B. P. Binks, A. Rocher, *Physical Chemistry Chemical Physics* **2010**, *12*, 9169.

[50] E. Dickinson, R. Ettelaie, T. Kostakis, B. S. Murray, *Langmuir* **2004**, *20*, 8517–8525.

[51] G. Kaptay, *Colloids and Surfaces A: Physicochemical and Engineering Aspects* **2003**, *230*, 67–80.

[52] Q. Liu, S. Zhang, D. Sun, J. Xu, *Colloids and Surfaces A: Physicochemical and Engineering Aspects* **2009**, *338*, 40–46.

[53] D. Chandler, *Nature* **2005**, *437*, 640–647.

[54] A. R. Studart, R. Libanori, A. Moreno, U. T. Gonzenbach, E. Tervoort, L. J. Gauckler, *Langmuir* **2011**, *27*, 11835–11844.

[55] A. R. Studart, U. T. Gonzenbach, I. Akartuna, E. Tervoort, L. J. Gauckler, *J. Mater. Chem.* **2007**, *17*, 3283–3289.

[56] R. Zhang, P. Somasundaran, *Adv. Colloid Interface Sci.* **2006**, *123*, 213–229.

[57] F. Reincke, W. K. Kegel, H. Zhang, M. Nolte, D. Wang, D. Vanmaekelbergh, H. Möhwald, *Phys. Chem. Chem. Phys.* **2006**, *8*, 3828–3835.

[58] D. Frydel, S. Dietrich, M. Oettel, *Physical Review Letters* **2007**, *99*.

[59] F. Bresme, M. Oettel, *Journal of Physics: Condensed Matter* **2007**, *19*, 413101.

[60] A. Böker, J. He, T. Emrick, T. P. Russell, *Soft Matter* **2007**, *3*, 1231–1248.

[61] B. P. Binks, P. D. I. Fletcher, *Langmuir* **2001**, *17*, 4708–4710.

[62] D. L. Cheung, S. A. F. Bon, *Soft Matter* **2009**, *5*, 3969–3976.

[63] T. N. Hunter, G. J. Jameson, E. J. Wanless, D. Dupin, S. P. Armes, *Langmuir* **2009**, *25*, 3440–3449.

[64] N. Nagy, A. Deák, Z. Hórvölgyi, M. Fried, A. Agod, I. Bársony, *Langmuir* **2006**, *22*, 8416–8423.

[65] D. Zang, A. Stocco, D. Langevin, B. Wei, B. P. Binks, *Physical Chemistry Chemical Physics* **2009**, *11*, 9522.

[66] Y. Zhang, *Review of Scientific Instruments* **2010**, *81*, 085101.

[67] L. Isa, F. Lucas, R. Wepf, E. Reimhult, *Nature Communications* **2011**, *2*, 438.

[68] B. P. Binks, L. Isa, A. T. Tyowua, *Langmuir* **2013**, *29*, 4923–4927.

[69] K. Geisel, L. Isa, W. Richtering, *Langmuir* **2012**, *28*, 15770–15776.

[70] V. N. Paunov, *Langmuir* **2003**, *19*, 7970–7976.

[71] D. C. E. Calzolari, D. Pontoni, M. Deutsch, H. Reichert, J. Daillant, *Soft Matter* **2012**, *8*, 11478.

[72] X. Fang, B. Li, I. V. Chernyshova, P. Somasundaran, *J. Phys. Chem. C* **2010**, *114*, 15473–15477.

[73] O. Zech, M. F. Haase, D. G. Shchukin, T. Zemb, H. Moehwald, *Colloids Surf., A* **2012**, *413*, 2–6.

[74] U. T. Gonzenbach, A. R. Studart, E. Tervoort, L. J. Gauckler, *Angew. Chem., Int. Ed.* **2006**, *45*, 3526–3530.

[75] B. P. Binks, S. O. Lumsdon, *Langmuir* **2000**, *16*, 8622–8631.

[76] A. Stocco, W. Drenckhan, E. Rio, D. Langevin, B. P. Binks, *Soft Matter* **2009**, *5*, 2215–2222.

[77] A. Stocco, E. Rio, B. P. Binks, D. Langevin, *Soft Matter* **2011**, *7*, 1260–1267.

[78] L. R. Arriaga, W. Drenckhan, A. Salonen, J. A. Rodrigues, R. Íñiguez-Palomares, E. Rio, D. Langevin, *Soft Matter* **2012**, *8*, 11085–11097.

[79] Timothy N. Hunter, Robert J. Pugh, George V. Franks, Graeme J. Jameson, *Adv. Colloid Interface Sci.* **2008**, *137*, 57–81.

[80] T. Horozov, *Curr. Opin. Colloid Interface Sci.* **2008**, *13*, 134–140.

[81] G. Mohamedi, M. Azmin, I. Pastoriza-Santos, V. Huang, J. Pérez-Juste, L. M. Liz-Marzán, M. Edirisinghe, E. Stride, *Langmuir* **2012**, *28*, 13808–13815.

[82] Z. Nie, J. I. Park, W. Li, S. A. F. Bon, E. Kumacheva, *J. Am. Chem. Soc.* **2008**, *130*, 16508–16509.

[83] H. Duan, D. Wang, N. S. Sobal, M. Giersig, D. G. Kurth, H. Möhwald, *Nano Lett.* **2005**, *5*, 949–952.

[84] E. Rio, W. Drenckhan, A. Salonen, D. Langevin, *Adv. Colloid Interface Sci.* **2014**, *205*, 74–86.

[85] M. Abkarian, *Phys. Rev. Lett.* **2007**, *99*, 188301.

[86] F. Bresme, M. Oettel, *J. Phys.: Condens. Matter* **2007**, *19*, 413101.

[87] R. D. Groot, S. D. Stoyanov, *Soft Matter* **2010**, *6*, 1682–1692.

[88] I. Lesov, S. Tcholakova, N. Denkov, *J. Colloid Interface Sci.* **2014**, *426*, 9–21.

[89] J. Israelachvili, *Langmuir* **1994**, *10*, 3774–3781.

[90] E. Tyrode, M. W. Rutland, C. D. Bain, *J. Am. Chem. Soc.* **2008**, *130*, 17434–17445.

[91] D. Y. Kwok, B. Tadros, H. Deol, D. Vollhardt, R. Miller, M. A. Cabrerizo-Vílchez, A. W. Neumann, *Langmuir* **1996**, *12*, 1851–1859.

[92] B.-Y. Zhu, T. Gu, *J. Chem. Soc., Faraday Trans. 1* **1989**, *85*, 3813–3817.

[93] B.-Y. Zhu, T. Gu, X. Zhao, *J. Chem. Soc., Faraday Trans. 1* **1989**, *85*, 3819–3824.

[94] G. Maret, P. Wolf, *Zeitschrift für Physik B Condensed Matter* **1987**, *65*, 409–413.

[95] G. Maret, *Current Opinion in Colloid & Interface Science* **1997**, *2*, 251 – 257.

[96] D. Pine, D. Weitz, J. Zhu, E. Herbolzheimer, *Journal de Physique* **1990**, *51*, 2101–2127.

[97] W. Brown, *Dynamic light scattering: the method and some applications*, *Vol. 49*, Oxford University Press, USA, **1993**.

[98] L. Cipelletti, D. Weitz, *Review of Scientific Instruments* **1999**, *70*, 3214–3221.

[99] D. Pine, D. Weitz, P. Chaikin, E. Herbolzheimer, *Physical Review Letters* **1988**, *60*, 1134.

[100] C. Oelschlaeger, M. Schopferer, F. Scheffold, N. Willenbacher, *Langmuir* **2009**, *25*, 716–723.

[101] S. Cohen-Addad, R. Höhler, *Phys. Rev. Lett.* **2001**, *86*, 4700–4703.

[102] C. Schmitt, C. Bovay, M. Rouvet, *Food Hydrocolloids* **2014**, *42, Part 1*, 139 – 148, Special Issue: A Festschrift in honour of Professor Eric Dickinson.

[103] Y. Hemar, D. Pinder, R. Hunter, H. Singh, P. Hébraud, D. Horne, *Journal of Colloid and Interface Science* **2003**, *264*, 502 – 508.

[104] Y. Hemar, D. S. Horne, *Colloids and Surfaces B: Biointerfaces* **1999**, *12*, 239 – 246.

[105] A. Knaebel, M. Bellour, J.-P. Munch, V. Viasnoff, F. Lequeux, J. L. Harden, *EPL (Europhysics Letters)* **2000**, *52*, 73.

[106] P. D. Kaplan, A. D. Dinsmore, A. G. Yodh, D. J. Pine, *Phys. Rev. E* **1994**, *50*, 4827–4835.

[107] S. Marze, M. Choimet, L. Foucat, *Soft Matter* **2012**, *8*, 10994–11004.

[108] A. Schwenzfeier, A. Helbig, P. A. Wierenga, H. Gruppen, *Food Hydrocolloids* **2013**, *30*, 258 – 263.

[109] F. Cardinaux, T. G. Mason, F. Scheffold, *AIP Conference Proceedings* **2013**, *1518*, 222–226.

[110] A. D. Gopal, D. J. Durian, *Phys. Rev. Lett.* **2003**, *91*, 188303.

[111] T. G. Mason, D. A. Weitz, *Phys. Rev. Lett.* **1995**, *74*, 1250–1253.

[112] C. Eliot, D. S. Horne, E. Dickinson, *Food Hydrocolloids* **2005**, *19*, 279 – 287.

[113] X.-L. Wu, D. J. Pine, P. M. Chaikin, J. S. Huang, D. A. Weitz, *J. Opt. Soc. Am. B* **1990**, *7*, 15–20.

[114] F. Scheffold, *Journal of dispersion science and technology* **2002**, *23*, 591–599.

[115] H. G. M. Ruis, K. van Gruijthuijsen, P. Venema, E. van der Linden, *Langmuir* **2007**, *23*, 1007–1013.

[116] E. ten Grotenhuis, M. Paques, G. A. van Aken, *Journal of Colloid and Interface Science* **2000**, *227*, 495 – 504.

[117] A. Chappellaz, M. Alexander, M. Corredig, *Food Biophysics* **2010**, *5*, 138–147.

[118] S. Sandra, M. Ho, M. Alexander, M. Corredig, *Journal of Dairy Science* **2012**, *95*, 75 – 82.

[119] S. Sandra, M. Alexander, D. G. Dalgleish, *Journal of Colloid and Interface Science* **2007**, *308*, 364–373.

[120] S. Sandra, C. Cooper, M. Alexander, M. Corredig, *Food Research International* **2011**, *44*, 951–956.

[121] R. R. R. Vincent, G. Gillies, A. Stradner, *Soft Matter* **2011**, *7*, 2697–2704.

[122] M. Corredig, M. Alexander, *Trends in Food Science & Technology* **2008**, *19*, 67 – 75.

[123] M. Alexander, D. G. Dalgleish, *Current Opinion in Colloid & Interface Science* **2007**, *12*, 179 – 186.

[124] D. Durian, D. Weitz, D. Pine, *Science* **1991**, *252*, 686–688.

[125] M. U. Vera, A. Saint-Jalmes, D. J. Durian, *Appl. Opt.* **2001**, *40*, 4210–4214.

[126] A. Stocco, J. Crassous, A. Salonen, A. Saint-Jalmes, D. Langevin, *Physical Chemistry Chemical Physics* **2011**, *13*, 3064–3072.

[127] S. Marze, D. Langevin, A. Saint-Jalmes, *Journal of Rheology (1978-present)* **2008**, *52*, 1091–1111.

[128] J. Crassous, A. Saint-Jalmes, *Soft Matter* **2012**, *8*, 7683–7689.

[129] D. J. Durian, D. A. Weitz, D. J. Pine, *Phys. Rev. A* **1991**, *44*, R7902–R7905.

[130] A. D. Gopal, D. J. Durian, *J. Opt. Soc. Am. A* **1997**, *14*, 150–155.

[131] T. Vilgis, *Die Molekularküche*, R. Frenzel (Ed.), Tre Torri Verlag, **2007**.

[132] S. Qian, J. J. Chen, *Chemical Engineering Science* **2015**, *122*, 250 – 269.

[133] A. Carl, A. Bannuscher, R. von Klitzing, *Langmuir* **2015**, *31*, 1615–1622.

[134] J. Boos, W. Drenckhan, C. Stubenrauch, *Langmuir* **2012**, *28*, 9303–9310, PMID: 22694021.

[135] R. Höhler, S. Cohen-Addad, D. J. Durian, *Current Opinion in Colloid & Interface Science* **2014**, *19*, 242–252.

List of Figures

2.1. The bulk liquid phase of the foam is a dispersion of silica particles onto which amines are adsorbed. Structural elements of the foam are the Plateau borders, four of which connect to form a vertex. Additionally, the lamellae separate two bubbles. The foam is composed of a collection of bubbles. Amines and particles may be adsorbed at all gas/liquid interfaces. An estimate of the size ranges of the structures is shown. 11

2.2. Possible structures of interfacially adsorbed particles. a) Isolated particles b) Aggregated particles forming a (fractal) network 12

2.3. Coupled mechanisms of foam ageing as explained in the text. 15

2.4. a) Beginning of surfactant adsorption, b) Isolated Langmuir type adsorption, c) cooperative adsorption due to lateral interaction, d) double layer above CMC. 17

3.1. Linear dependence of the bulk density of the particle suspensions on the mass concentration. 19

3.2. Setup of a x-ray reflectivity experiment. Monochromation optics are used in front of the sample but are omitted in the sketch. 21

3.3. Typical setup of an ADSA experiment. 22

3.4. Schematic setup of a DLS or DWS experiment. The correlation procedure of the data is identical in both cases. In DWS, the sample is probed in transmission (not shown). 25

3.5. Angular distribution of scattered light for a) a Rayleigh scatterer of diameter 70 nm. b) a Mie scatterer of diameter 770 nm. The intensity is in arbitrary units and scaled logarithmically. 27

5.1. Interfacial tension isotherms of alkyl amine solutions without particles (open symbols) and with a particle concentration of 50 g/L (closed symbols). Adsorption time is about 10 seconds. Error bars are smaller than the sysmbols. 38

5.2. Left: side view of an interfacially adsorbed nanoparticle with contact angle θ. Right: top view of virtual slices through the system in a plane parallel to the interface. 39

5.3. Calculation of the electron density profile. Each data point represents one of the 200 layers. Particle diameter 28±3 nm, contact angle 60±5° 40

5.4. XRR curves of pentyl amine (C_5) modified silica nanoparticles with increasing alkyl amine concentration. Silica concentration 25 g/L. 41

5.5. XRR curves of hexyl amine (C_6) modified silica nanoparticles with increasing alkyl amine concentration. Silica concentration 25 g/L. 42

5.6. XRR curves of heptyl amine (C_7) modified silica nanoparticles with increasing alkyl amine concentration. Silica concentration 25 g/L. 42
5.7. XRR curves of octyl amine (C_8) modified silica nanoparticles with increasing alkyl amine concentration. Silica concentration 25 g/L. 43
5.8. Contact angles as a function of amine concentration determined by XRR according to the model in this chapter. Particle diameter 28 nm, particle concentration 25 g/L. The distribution width is omitted for clarity, it can be found in Table 5.1. Lines are guides to the eye. 44
5.9. Calculated equilibrium surface fraction of the particle layer as a function of the surface charge density and the residual surface charge fraction in the low-ϵ_r phase (in percent). The volume fraction of the particles in the bulk phase is 0.0125. 47
5.10. Side-view of the assumed distribution of amine on the particle surface and the air/water interface as the amine concentration is increased. 49
5.11. Different possible states of a foam lamella. Left: Particle layer on both gas/liquid interfaces. Right: Bridging particles 51

6.1. Electrophoretic mobilitiy and ζ-potential (in mV) dependence on alkyl amine chain length and concentration for a dispersion of 2.5wt-% silica particles. Adsorption of the amines to the particles leads to charge neutralisation at the particle/water interface. Bulk flocculation at a certain amine concentration is indicated by "floc". Redispersion of the particles is marked by "redisp". Separation into a water-rich and amine-rich phase is indicated by "sep". 56
6.2. Probing of hydrophobic domains by fluorescence spectroscopy. Ratio of the fluorescence intensities I_1 and I_3 of the pyrene molecule as marked in the inset in the lower right. Ratio for the pure amine solutions at increasing concentrations (squares) and the mixed dispersions with an amount of 2.5wt-% silica particles (circles) for the studied chain lengths. A change of the ratio I_1/I_3 from 1.8 to 1.2 indicates the formation of hydrophobic domains. For heptylamine c) and octylamine d), phase separation occurs above the concentrations shown. Solid lines are guides to the eye. 58
6.3. Surface pressure isotherm analysis from pendant drop measurements. Hexylamine modified silica particles were compressed at the amine concentration stated at the corresponding plots. Closed and open symbols correspond to repeated measurements of the surface pressure isotherm at the same hexylamine concentration. Power laws were fit to the data. 60

6.4. Collapse area fraction at which either the surface pressure remains constant or the drop shape become non-Laplacian. An increasing collapse area A/A_0 indicates a higher particle coverage at the interface. The adsorption time for all samples was 90 s. Solid lines are guides to the eye. 61
6.5. Interfacial aggregation in a thin film pressure balance experiment. The particle aggregates are seen as bright spots. Scale bar corresponds to 100 μm. The image was recorded by Martin Uhlig. 62
6.6. Comparison of a) surface pressure scaling exponent as described in Eq. (6.3) and b) foamability. The foam height increases when the scaling exponent is below -6. Solid lines are guides to the eye. 63
6.7. Foamability of different silica/alkylamine mixtures. The concentrations correspond to the ones used to create Figure 6.6b 64
6.8. Foam half-life as a function of amine concentration. The sudden increase in foam half-life corresponds to the onset of bulk flocculation. 65
6.9. Surface micellization free energy from fluorescence spectroscopy. The surface micellization concentration was measured by using pyrene as a hydrophobic probe. The data were fitted to Eq. (6.2). 67

7.1. Hydrodynamic radius of the nanoparticles as a function of amine concentration measured by DLS. For all amine carbon chain lengths, aggregation is visible above the critical amine concentration (CAC). Silica concentration 5 g/L. 73
7.2. Fraction of particles that are immobilized in the produced foam, as a function of amine concentration and chain length. Above the CAC, a lot of particles are trapped in the foam due to aggregation and gel formation in the foam matrix. Lines are guides to the eye. Silica concentration 25 g/L. . 74
7.3. Produced foam volume as a function of extracted particle fraction. The linear dependence indicates an approximately constant number of particles per air bubble. The line serves as guide to the eye. Silica concentration 25 g/L. 75
7.4. a) lin-log plot of the field autocorrelation function $g_1(\tau)$ of the transmitted light intensity. b) log-lin plot of $g_1(\tau)$ with an exponential fit to extract the characteristic rearrangement time of the foam. c) Field autocorrelation function $g_E^B(\tau)$ as calculated by (7.1) with the corresponding fit to obtain the particle diffusion time. Silica concentration 50 g/L. 76

7.5. Brownian diffusion time of the particles as a function of amine concentration and chain length. An increase can be seen above the CAC which indicates aggregates. Silica concentration 50 g/L. 78
7.6. Foam rearrangement times as a function of amine concentration and chain length. Larger times reflect slower dynamics of the foam matrix, namely bubble rearrangements and film ruptures. Silica concentration 50 g/L. . . . 79
7.7. Logarithm of plateau value g^* between the two decays of the autocorrelation function $g_1(\tau)$ as a function particle volume fraction. The linear relation can be fitted to yield a measure of the particle size. Silica concentration 50 g/L. 80
7.8. Theoretical values of the (transport) mean free path lengths l_c and l_c^* as a function of particle radius at constant silica mass concentration of 10 g/L. The l_c values are the mean distance between two scattering events in an unfoamed dispersion. The l_c^* values represent the step length after which the photon direction has been randomized in the same system. 86
7.9. Ageing of the foam films below and above the CAC. Below the CAC, particles remain isolated and the liquid drains out of the foam. Above the CAC, particle aggregates will prevent the film from thinning which slows down coarsening and coalescence. 87
7.10. Ageing of the Plateau borders a) below and b) above the CAC. Below the CAC, particles remain isolated and the liquid drains out of the foam. Above the CAC, particle aggregates will prevent the liquid from draining which slows down the ageing processes. 87

8.1. Conceptual and qualitative summary of the results. The results are general for all amine chain lengths, the exact concentration range varies. 91

Appendix A.

Listings

A.1. XRR fitting

In order to use the script below, IGOR Pro and the Motofit package have to be installed on the computer on which the analysis is performed. The code has not been optimized for speed or readability, but it works.

Listing of Motofit Fitting Functions used to evaluate the XRR data.

```
#pragma rtGlobals=1              // Use modern global access method.



Function create_wave()

        Variable i=0
        Variable h=1
        Variable r=2
        Variable z
        make/n=100 wave
        SetScale/I x, -10, 10, "nm", wave

        For(z=-10;z<=10;z=z+0.2)
                if((z>=-1*h)&&(z<=2*r-h))
                        wave[(z+10)*5] = r^2-(z-(r-h))^2
                else
                        wave[(z+10)*5] = 0
                endif
                i=i+1
        Endfor
End

Function particleLayer(coefs,rr,qq):fitfunc
        wave coefs,qq,rr
        particleLayerToRef(coefs)
        Wave W_forReflectivity
        motofit(W_forreflectivity,RR,qq) // AbelesAll(coefs,rr,qq <- 2 dim
            )
        //RR=log(RR)
End

Function particleLayerToRef(coefs)

        wave coefs
        Variable rAv=coefs[0],sigR=coefs[1],noR=15 // beware, until now,
            negative radii are possible, so don't use rAv < 3*sigR
        //Variable hAv=coefs[2],sigH=coefs[3],noH=15 // penetration height/
            depth depends on particle radius and is governed by contact
            angle
        Variable caAv=coefs[2],sigCA=coefs[3],noCA=15
        Variable s=coefs[4]
```

```
39          Variable k,i,j
40          Variable zStart = -2*rAv-3*sigR-2, zEnd = 2*rAv+3*sigR+2
41          Variable noProf=200
42          Variable z,h
43          Variable count=0
44          Variable dR,dCA,dz
45          Variable sigI = coefs[10]
46          Variable sldFront = coefs[5] //5
47          Variable sldMiddle = coefs[6]
48          Variable sldBack = coefs[7] //9.45
49          Variable scaling = coefs[8]
50          Variable background = coefs[9]
51
52
53          make/o/d/n=(noProf*4+6) W_forReflectivity
54          W_forReflectivity = 0
55
56          W_forReflectivity[0] = noProf //N
57          W_forReflectivity[1] = scaling //scale factor
58          W_forReflectivity[2] = sldFront // sld fronting
59          W_forReflectivity[3] = sldBack // sld backing
60          W_forReflectivity[4] = background // linear background
61          W_forReflectivity[5] = 0 // roughness backing to layer no N
62
63          make/o/n=(noR) rDist
64          Setscale/I x, (rAv-3*sigR), (rAv+3*sigR), rDist
65          Duplicate/o rDist, rVal
66          rDist = 1/sigR/sqrt(2*Pi)*exp(-(x-rAv)^2/2/sigR^2)
67          rVal = x
68          dR = rVal[1]-rVal[0]
69
70          caAV = caAV//*Pi/180
71          sigCA = sigCA//*Pi/180
72
73          make/o/n=(noCA) caDist
74          Setscale/I x, (caAv-3*sigCA), (caAv+3*sigCA), caDist
75          Duplicate/o caDist, caVal
76          caDist = 1/sigCA/sqrt(2*Pi)*exp(-(x-caAv)^2/2/sigCA^2)
77          caVal = x
78          dCA = caVal[1]-caVal[0]
79
80          make/o/n=(noProf) profileP
81          SetScale/I x, zStart, zEnd, "nm", profileP
82          Duplicate/o profileP, profileVal
83          profileP = 0
84          profileVal = x
85          dz = abs(profileVal[1]-profileVal[0])
86
87          Duplicate/o profileP, tempProfile
88          Duplicate/o profileP, fullProfile
89
90          For(k=0;k<noCA;k=k+1)
91          //count +=  caDist[k]*dCA  // check for distribution "integral" = 1
92          //count +=  rDist[k]*dR // check for distribution "integral" = 1
93                  For(i=0;i<noR;i=i+1)
```

```
94                      count += caDist[k]*dCA*rDist[i]*dR      // check
                            for double distribution "integral" = 1
95                      if(rVal[i] > 0)
96
97                              tempProfile = 0
98                              //tempProfile[((-1*hVal[k]-zStart)*noProf/(
                                    abs(zStart)+abs(zEnd))),((2*rVal[i]-hVal
                                    [k])-zStart)*noProf/(abs(zStart)+abs(
                                    zEnd))] = hDist[k]*dH*rDist[i]*dR*2*Pi*(
                                    rVal[i]^2-(x-(rVal[i]-hVal[k]))^2)/sqrt
                                    (3)/(2*rVal[i]+s)^2
99                              For(z=zStart;z<=zEnd;z=z+((abs(zStart)+abs(
                                    zEnd))/noProf))
100                                     //h = rVal[i]-rVal[i]*cos((180-
                                            caVal[k])*Pi/180) //contact
                                            angle through air
101                                     h = rVal[i]-rVal[i]*cos((caVal[k])*
                                            Pi/180) //contact angle through
                                            water
102
103                                     if((z>=-1*h)&&(z<=2*rVal[i]-h))
104                                             tempProfile[(z-zStart)*
                                                    noProf/(abs(zStart)+abs(
                                                    zEnd))] = caDist[k]*dCA*
                                                    rDist[i]*dR*2*Pi*(rVal[i
                                                    ]^2-(z-(rVal[i]-h))^2)/
                                                    sqrt(3)/(2*rVal[i]+s)^2
105                                     else
106                                             tempProfile[(z-zStart)*
                                                    noProf/(abs(zStart)+abs(
                                                    zEnd))] = 0
107                                     endif
108
109                             Endfor
110                             profileP = profileP+tempProfile
111                     endif
112             Endfor
113     Endfor
114
115     tempProfile = 1/2*(1+erf(x/sigI/sqrt(2)))*(sldBack-sldFront)+
            sldFront
116     //tempProfile = 1/2*(1+erf(x/sigI/sqrt(2)))
117     //KillWaves rDist,rVal,caDist,caVal,profileVal
118     //fullProfile = (1-profileP)*tempProfile+(sldMiddle)*profileP
119     fullProfile = (1-profileP)*tempProfile+sldMiddle*profileP //
            working
120     //fullProfile = tempProfile
121
122     //print(count)
123
124     For(i=0;i<noProf;i=i+1)
125             W_forReflectivity[4*i+6] = dz*10 // thickness layer
126             W_forReflectivity[4*i+7] = fullProfile[i] // sld layer
127             W_forReflectivity[4*i+8] = 0 // solvent penetration in %
128             W_forReflectivity[4*i+9] = 0 // rougness layer n to n-1
```

```
129         Endfor
130
131 End
```

A.2. Surface Fraction Calculations

Each listing has to be converted to a file and named according to its title. Then it can be run in an octave console by starting run equi_surfrac.

equi_surfrac.m

```
1  filename = input("Enter filename: ","s")
2  fid = fopen(filename,'w');
3
4  fprintf(fid,"R[m]\tcont_angle[Â°]\tz[-]\trescharfrac[-]\tsurcharden[C/m^2]\
       teps_org[-]\teps_water[-]\tift[mN/m]\tI[mol/L]\tT[K]\tvolfrac[-]\tH[J]\
       troot\tf(root)\treturn code\n");
5  printf("R[m]\tcont_angle[Â°]\tz[-]\trescharfrac[-]\tsurcharden[C/m^2]\
       teps_org[-]\teps_water[-]\tift[mN/m]\tI[mol/L]\tT[K]\tvolfrac[-]\tH[J]\
       troot\tf(root)\treturn code\n");
6
7  for i = [0.05:0.001:0.3]
8      surcharden = i;
9      minimize = @(x) ( (interface_energy(r,contangle,ift) ...
10                    + vdw(x,z,H) ...
11                    + screened_coulomb(x,r,contangle,z,surcharden,I,eps_water,T
                          ) ...
12                    + unscreened_coulomb(x,r,contangle,z,rescharfrac,surcharden
                          ,eps_org) ...
13                    + dipole_interaction(x,r,contangle,z,surcharden,eps_org,I,
                          eps_water,T) ...
14                    - bulk_energy(r,volfrac,T)) ...
15                    ./4.14e-21 ... #divide by kT
16                     );
17     [a b c] = fsolve(minimize,0.3);
18     fprintf(fid,"%e\t%u\t%u\t%f\t%f\t%f\t%f\t%f\t%f\t%f\t%f\t%e\t%f\t%f\t%f
           \n",r,contangle,z,rescharfrac,surcharden,eps_org,eps_water,ift,I,T,
           volfrac,H,a,b,c);
19     printf("%e\t%u\t%u\t%f\t%f\t%f\t%f\t%f\t%f\t%f\t%f\t%e\t%f\t%f\t%f\n",r
           ,contangle,z,rescharfrac,surcharden,eps_org,eps_water,ift,I,T,
           volfrac,H,a,b,c);
20 endfor
21
22 fclose(fid);
```

params.m

```
1 z=6                          # number of nearest neighbor particles [-]
2 r=14e-9                       # particle radius [m]
3 surcharden = 0.6                  # surface charge density [C/m^2]
4 rescharfrac = 0.0
            # residual charge factor for unpolar phase
```

```
5 eps_org = 1                                                                    #
      relative dielectric constant unpolar phase
6 eps_water = 78                                                 # relative
      dielectric constant polar phase
7 contangle = 40
8 T = 300
9 volfrac = 0.0125
10 k = 1.38e-23
11 H = 1e-20
12 I = 0.05
13 ift = 50
```

bulk_energy.m

```
1 function y = bulk_energy(r,volfrac,T)
2                 k = 1.38e-23;
3                 v_water = 3e-30; # water volume ~ 3e-30 m^3
4                 v_p = 4/3*pi.*r^3;
5           y = -k.*T.*(log(v_water./v_p)+log(volfrac));
6 end
```

debye_length.m

```
1 function L = debye_length(I,eps,T)
2                 I = I*1000;
3                 eps_0   = 8.854e-12;
4                 N_A = 6.022e23;
5                 e = 1.602e-19;
6                 k = 1.381e-23;
7     L = sqrt(eps_0*eps*k*T./(2*N_A*e^2.*I));
8 end
```

dipole_interaction.m

```
1 function y = dipole_interaction(x,r,angle,z,surcharden,eps_org,I,eps,T)
2     phi_full = 1/6*sqrt(3)*pi;  # maximum 2D packing fraction ~ 0.906
3     eps_0       = 8.854e-12;                                          #
          dielectric constant of vacuum
4     a_frac = x./phi_full;       # reduced area fraction
5                 A_cap = sphere_cap_area(r,angle);
6                 ld = debye_length(I,eps,T);
7                 #eps_eff = (eps_org.+eps)./2;
8                 f1 = sphere_cap_area(r,angle)./(4.*pi.*r.^2);
9                 f2 = sphere_cap_area(r,180.-angle)./(4.*pi.*r.^2);
10                eps_eff = f1.*eps_org+f2.*eps;
11          y = 5.*z.*(A_cap.*surcharden.*ld).^2./(64.*pi.*eps_eff.*eps_0.*r
                .^3).*a_frac.^(3/2);
12 end
```

interface_energy.m

```
1 function y = interface_energy(r,angle,ift)
2                 k = 1.38e-23;
3                 ift = ift./1000;
4           y = -pi.*r.^2.*ift.*(cos(angle/180*pi)-1).^2;
5 end
```

screened_coulomb.m

```
function y = screened_coulomb(x,r,angle,z,surcharden,I,eps,T)
    phi_full = 1/6*sqrt(3)*pi;  # maximum 2D packing fraction ~ 0.906
    eps_0       = 8.854e-12;                                    #
        dielectric constant of vacuum
    a_frac = x./phi_full;       # reduced area fraction
    ld = debye_length(I,eps,T);
                A_cap = sphere_cap_area(r,(180-angle));
          y = z.*(A_cap.*surcharden).^2/(32.*pi.*eps.*eps_0.*r).*(3.*sqrt(
              a_frac)+2.*r./ld).*exp(-2.*r./(ld.*sqrt(a_frac)));
end
```

sphere_cap_area.m

```
function A_cap = sphere_cap_area(R,angle)

   A_cap = 2*pi*R^2*(1-cos(angle/180*pi));

end
```

unscreened_coulomb.m

```
function y = unscreened_coulomb(x,r,angle,z,rescharfrac,surcharden,eps_org)
    phi_full = 1/6*sqrt(3)*pi;  # maximum 2D packing fraction ~ 0.906
    eps_0       = 8.854e-12;                                    #
        dielectric constant of vacuum
    a_frac = x./phi_full;       # reduced area fraction
                A_cap = sphere_cap_area(r,angle);
          y = 3.*z.*(A_cap.*rescharfrac.*surcharden).^2./(32.*eps_org.*
              eps_0.*r.*pi).*sqrt(a_frac);
end
```

vdw.m

```
function y = vdw(x,z,H)
    phi_full = 1/6*sqrt(3)*pi;  # maximum 2D packing fraction ~ 0.906
    a_frac = x./phi_full;       # reduced area fraction
          y = -z*H./12*(a_frac.^2./(2.*(1-a_frac).^2)+a_frac+log(1-a_frac))
              ;
end
```